2011

Mechanistic Modeling of Photocatalytic Water Disinfection

Omatoyo Kofi Dalrymple
University of South Florida, odalrymp@mail.usf.edu

Mechanistic Modeling of Photocatalytic Water Disinfection

by

Omatoyo Kofi Dalrymple

A dissertation submitted in partial fulfillment
of the requirements for the degree of
Doctor of Philosophy
Department of Civil & Environmental Engineering
College of Engineering
University of South Florida

Co-Major Professor: Yogi Goswami, Ph.D.
Co-Major Professor: Maya Trotz, Ph.D.
Elias Stefanakos, Ph.D.
Vicki Luna, Ph.D.
Vinay Gupta, Ph.D.
Jeffrey Cunningham, Ph.D.

Date of Approval:
March 8, 2011

Keywords: Drinking Water, Double Layer, *E. coli*, Solar Applications, Titanium Dioxide

DEDICATION

To my wife, Rhonda, and son, Jaden; my father, Norman Dalrymple, and mother, Agnes Dalrymple; my siblings, Najuma, Olatunde, Kojo, Palesa, Monifa, Ayodele, and Kayode; my nieces, Palesa, Ticisa, Jenncia, and Takiyah; and nephews, Randy, Akintunde, Rashad, Keyondre, Raydon, and Azriel

ACKNOWLEDGEMENTS

Research, particularly of this magnitude, can never be accomplished by one person. The work contained herein was conducted under the auspices of the Clean Energy Research Center (CERC) at the University of South Florida with financial support from the Florida Energy Systems Consortium (FESC). Special thanks to my research committee and my co-major professors, Dr. Yogi Goswami and Dr. Maya Trotz. Special thanks to Dr. Elias Stefanakos, the Director of the CERC. I also want to thank Dr. Vinay Gupta for allowing the use of his dynamic light scattering equipment, and Dr. Norma Alcantar and her graduate student, Eva Williams, for teaching me to make lipid vesicles in their lab. A special “thank you” to Mr. Charles Garretson, our exceptional lab manager and a truly brilliant engineer who can build almost anything that can be conceived. I also want to thank Mr. Ed Haller for his patience in teaching me to use the transmission electron microscope. I am indebted to my colleagues, who offered their assistance when I needed it the most; Dru Latchman, Ray Morris, Matthew Cutter, Russell Ferlita, Mohammad Abutayeh, Ken Thomas, Ricardo Vasquez, Ana Lucia Prieto, Gokman Demirkaya, and Yangyang Zhang.

TABLE OF CONTENTS

LIST OF TABLES

LIST OF FIGURES

LIST OF SYMBOLS

A	Hammaker constant	J
a_1	radius of bacterial cell	m
a_2	radius of catalyst particle	m
a_i	inactivation rate around the inflection point	
$\mathrm{a_r}$	ratio of catalyst particle radius to bacterial cell radius a_2/a_1	
b_1	Weibull probability distribution scale parameter	
b_2	Weibull probability distribution shape parameter	
c	disinfectant concentration	$mg \cdot L^{-1}$
C	concentration and the of specifically adsorbing ions	$mol \cdot L^{-1}$
$\mathrm{C_{An}}$	concentration of anion	$mol \cdot L^{-1}$
$C_{An,i}$	concentration of the specific anion species in solution	$mol \cdot L^{-1}$
$\mathrm{c_{cat}}$	mass concentration of catalyst	
C_{BP}	concentration of byproducts	$mol \cdot L^{-1} \cdot g^{-1} \cdot s^{-1}$
C_i^{bulk}	concentration of electrolytes in the bulk solution	$mol \cdot L^{-1}$

C_i^{mem}	concentration of electrolytes in the ion penetrable layer	$mol \cdot L^{-1}$
d	coefficient of dilution	
D	particle diffusivity tensor	
D_b	diffusion coefficient in the bulk	$m^2 \cdot s$
D_{bac}	diffusion coefficient of the bacteria	$m^2 \cdot s$
D_{cat}	catalyst particle diffusion coefficient	$m^2 \cdot s$
D_{rel}	relative diffusion coefficient	$m^2 \cdot s$
e	electron charge	C
e_{cb}^-	conduction band electron	
E	exposure to disinfectant	
$E_{c,i}$	characteristic lethal exposure dose for the particular organism	
F	Faraday constant	$C \cdot mol^{-1}$
F_s	integrated absorption fraction	
$G_{\cdot OH}$	rate of OH radical generation	$mol \cdot L^{-1} \cdot s^{-1}$
$G'_{\cdot OH}$	normalized rate of OH radical generation	
h_{vb}^+	valence band hole	
H^*	dimensionless parameter that defines the effective interaction range	
I_a	absorbed photon flux	$E \cdot L^{-1} \cdot s^{-1}$

I_0	incident photon flux	$E \cdot L^{-1} \cdot s^{-1}$
I_t	transmitted light flux	$E \cdot L^{-1} \cdot s^{-1}$
j	vector function describing the flows (flux) of n_p	$m^{-2} \cdot s^{-1}$
$\bar{j}$	normalized flux	$m^{-2} \cdot s^{-1}$
$\bar{j}_0$	normalized stationary adsorption flux	$m^{-2} \cdot s^{-1}$
k	generic disinfection rate constant	
k'	product of disinfection rate constant and disinfection concentration (kc)	
k_B	Boltzmann constant	$J \cdot K^{-1}$
k_{BP}	reaction rate constant for byproduct oxidation	$mol \cdot L^{-1} \cdot s^{-1}$
k_d	diffusion-controlled rate constant	
$k_{d'}$	rate constant for dissociation or organism-radical complex and radical quenching and repair	
k_{dis}	observed rate constant for disinfection	$mol \cdot L^{-1} \cdot s^{-1}$
k_{inv}	rate constant of inactivation	
$k_{\cdot OH}$	OH radical consumption rate constant	$L^n \cdot M^{n-1} \cdot CFU^{-1} \cdot s^{-1}$
K_a	generic acid dissociation constant	
K_a^S	surface acidity constant	
K_a^{bulk}	acidity constant in bulk solution	
K_{An}^s	Langmuir adsorption rate constant for anion on surface of metal oxide	

K_{BP}^{ads}	Langmuir adsorption rate constant for disinfection byproducts on surface of metal oxide	
$K_{[\mathrm{cell}\cdot(\mathrm{OH})_m]}$	equilibrium constant for the formation of the cell-radical complex	
K_D	empirical constant of the Haas model	
K_{pseudo}	Langmuir parameter for Marugán model	
L_e	dimensionless double layer thickness given by $\kappa a_2{}^{-1}$	
L_{TA}	total concentration of acidic sites on bacterial surface	$mol \cdot m^{-2}$
L_{TB}	total concentration of basic sites on bacterial surface	$mol \cdot m^{-2}$
n	reaction order with respect to concentration of OH radicals	
n_b	number concentration of catalyst particles in bulk solution	L^{-1}
n_p	number concentration of catalyst particles on surface of bacteria	L^{-1}
n_s	number of particles collected on an element of area	
N	bacteria concentration	$CFU \cdot L^{-1}$
N_0	initial concentration of bacteria	$CFU \cdot L^{-1}$
N_A	Avogadro's number	
N_{ads}	number of adsorption sites per unit area	m^{-2}

N_{dam}	concentration of damaged cells in the Marugán model	CFU·L $^{-1}$
N_{undam}	concentration of undamaged cells in the Marugán model	CFU·L^{-1}
Q_e	total surface charge	
R_{BP}	rate of byproduct oxidation	mol·L^{-1}·g^{-1}·s^{-1}
R_d	overall disinfection reaction rate for bimolecular reaction	CFU·L^{-1}·s^{-1}
r_{dis}	observed rate of disinfection	CFU·L^{-1} ·s^{-1}
$R_{q,i}$	rate of inhibition due to quenching of radicals by anions	mol·L^{-1}·s^{-1}
s	sink terms in continuity equation	
S	microbial survival $\frac{N}{N_0}$	
t	time	s
T	absolute temperature	K
t_{lag}	time lag parameter for initial lag phase in the disinfection process	s
t_r	relaxation time	s
U	particle translation velocity vector	
$V_e(x)$	potential energy of double layer interaction between the two spheres at distance x	J
$V_{pl}(x)$	potential energy of the electrostatic interactions per unit area between two plates at separation x	J

$V_T(x)$	total potential energy of interaction between two spherical particles separated by a distance x	J
$V_v(x)$	potential energy for van der Waal interaction between the two particles at distance x	J
$v_x(x)$	fluid velocity component directly perpendicular to the interface	$m \cdot s^{-2}$
x_d	thickness of the organism's diffusive boundary layer	m
y	reaction order with respect to cell concentration	
z	valence of electrolyte ion	

Greek symbols

α	coefficient of attenuation per mass concentration of catalyst	$L \cdot g^{-1} \cdot cm^{-1}$
β	empirical constant of the Haas model	
ΔG_{ads}	Gibbs energy of adsorption per molecule	J
ΔG_{spec}	Gibbs energy of specific interaction	J
$\Delta\phi_i$	fraction of the population with a critical exposure of $E_{c,i}$	
ε_m	dielectric constant within the cell membrane layer	$F \cdot m^{-1}$
ε_o	electric constant	$F \cdot m^{-1}$
ε_r	relative permittivity	
ε_s	relative dielectric constants of the solution	
ξ	dimensionless interaction energy	

ζ	zeta potential	V
η	dynamic viscosity	Pa·s
θ	dimensionless surface coverage	
θ_{An}	surface coverage of anion species on metal oxide	
θ_{BP}	surface coverage of byproducts	
θ_T	total surface coverage	
θ_t	surface concentration of particles adsorbed during the transient conditions	
θ_∞	maximum theoretical surface coverage for an RSA model	
κ	Debye-Huckel parameter	m^{-1}
λ	concentration-time product constant	$mg \cdot s \cdot L^{-1}$
μ_e	electrophoretic mobility	$m^2 \cdot s^{-1} \cdot V^{-1}$
ρ_e	surface charge density	$C \cdot m^{-3}$
ρ_{el}	charge density contribution of the ions in the ion-penetrable layer	$C \cdot m^{-3}$
ρ_{fix}	fixed surface charge	$C \cdot m^{-2}$
σ_{ads}	specifically adsorbed charge per unit area	$C \cdot m^{-2}$
σ_d	charge density in the double layer	$C \cdot m^{-3}$
τ_d	ratio of time to relaxation time t/t_r	
$\varphi_{\cdot OH}$	quantum yield of radical generation	

ψ	electrostatic potential of the double layer	V
ψ_0	electrostatic surface potential	V
ψ_1	electrostatic potential at bacterial cell surface	V
ψ_2	electrostatic potential at catalyst surface	V
ψ_d	potential difference across the diffuse part of the double layer	V
ψ_{DON}	Donnan potential	V

ABSTRACT

The main goal of this research was to develop a mechanism-based model for photocatalytic disinfection of bacteria in water using suspended catalyst particles in batch reactors. The photocatalytic disinfection process occurs as a semiconductor photocatalyst, most commonly titanium dioxide (TiO_2), is irradiated with light of wavelength less than 380 nm to produce hydroxyl radicals and other highly reactive oxidants which can inactivate microorganisms. Photocatalytic disinfection involves a complex interaction of many fundamental mechanisms such as light absorption and scattering by semiconductor particles, electrochemical surface reactions, and heterogeneous colloidal stability. Current models, based largely on chemical reacting systems, do not adequately account for these fundamental mechanisms. Even the Langmuir model developed for heterogeneous systems cannot describe the interactions of such large colloidal particles. As a result, it is difficult to assess the combined effects of many important factors which go into the design of a photocatalytic disinfection system.

A mechanistic modeling approach is desirable because it provides a framework to understand the influence of many important parameters on the disinfection process. It requires a description of the physical properties of the catalyst, the nature of the suspending electrolyte solution, the physical and chemical properties of the cell surface, and the energetic aspects that influence the interaction of the particles. All these aspects

are interrelated. While it is customary to envision the adsorption of reactants unto a catalyst surface, for photocatalytic disinfection involving suspended catalyst particles, multiple catalyst particles adhere to the bacterial surface.

In this work a mechanistic model has been developed that simulates the effect of light intensity and catalyst concentration on the disinfection process. The simulations show good agreement with the experimental data for stable colloidal suspensions, that is, suspensions in which rapid aggregation of cells and TiO_2 do not occur. Increased disinfection rates and high levels of inactivation can be achieved by maintaining a relatively low catalyst-to-microbe ratio while maximizing the light intensity. The influence of pH and ionic strength on the disinfection process have been included in the model, but these are only expected to be accurately predicted when the solution remains stable.

CHAPTER 1: INTRODUCTION

1.1 The global water crisis

Waterborne pathogens, including viruses, bacteria, and protozoa, are responsible for 3.5 billion cases of diarrhea each year and 1.8 million deaths as a result of contaminated drinking water. The majority of those affected are children under the age of 5 years [1]. Even though there have been outbreaks in developed nations, waterborne diseases are much more prevalent in developing countries, particularly among the poor. In general, access to clean water and basic sanitation is a major problem in many poor communities. According to the United Nations, as much as 50% of the developing world is affected by the main diseases or infections associated with inadequate water supply and sanitation. These include diarrhea, intestinal helminth infections, dracunculiasis, schistosomiasis, and trachoma [2].

1.2 Traditional and low-cost disinfection options

In addition to being chemically nontoxic, water must also be biologically safe to consume; that means the potential to cause infection must be removed. In many poor communities, boiling water before consumption is the only effective option available for disinfection. However, boiling can be energy intensive, especially to meet the needs of large families. Solar disinfection is a low-cost alternative in which water in transparent plastic or glass bottles is exposed to direct sunlight. The dual action of solar infrared heating and ultraviolet irradiation inactivates a range of microorganisms [3-5].

Nevertheless, solar disinfection is limited to small volumes of clear water which must be consumed soon after treatment because of the potential for re-growth of pathogens.

By far the most common method to disinfect drinking water for the last 100 years is chlorination. In the United States, about 98% of municipal water treatment facilities use chlorine, and about 200 million residents receive chlorinated drinking water at home [6]. Chlorine is a powerful oxidant and does not only kill pathogens, it also reacts with dissolved natural organic compounds to form many chlorinated byproducts (DBPs). Studies show that some classes of DBPs such as trihalomethanes (THMs) and haloacetic acids (HAAs) are potentially mutagenic and carcinogenic [7, 8]. The control of DBPs has become important in water treatment adding another level of difficulty to the process. Recent Environmental Protection Agency (EPA) regulations have further limited THMs, HAAs and other DBPs (including chlorite and bromate) in drinking water [9]. As a result, many water systems now limit the use of chlorine to high-quality groundwater or reduce total organic carbon prior to disinfection. Another concern of chlorine disinfection is that some organisms tend to develop resistance to chlorine or require higher than normal doses for complete inactivation [10, 11]. Relatively high residual chlorine concentration can make drinking water taste and smell unpleasant. Nonetheless, chlorination remains an important disinfection method.

1.3 Advanced treatment processes

Many advanced alternative disinfection processes are now available. These include the use of ozone gas, chlorine dioxide, advanced membrane processes, and

germicidal ultraviolet (UV) irradiation. Most of these advanced methods are very effective against a wide range of harmful pathogens. However, the cost may be prohibitive since expensive chemicals and costly equipment are required to generate the disinfectant onsite. They are often associated with increased process complexity and safety requirements as well.

Moreover, ozonation produces harmful byproducts including bromate and other brominated DBPs formed in waters with elevated bromide [12, 13]. Chlorine dioxide produces less harmful disinfection byproducts than chlorine, but the formation of chlorite and chlorate may be a problem for dialysis patients. Also, chlorine dioxide is less effective against rotaviruses and *E. coli* bacteria. UV disinfection makes use of DNA-damaging shortwave radiation (less than 280 nm), which requires the set up of expensive lighting equipment and is associated with increased energy utilization.

1.4 The case for photocatalytic disinfection

In general, these advanced techniques are out of reach and often not suited for the local circumstances of developing countries where contaminated water is a real issue. However, heterogeneous photocatalysis may be a suitable alternative because it is capable of utilizing sunlight directly so it can be used in remote areas, and titanium dioxide (TiO_2) is widely available. The reactor setup can also be simple either as a suspended-catalyst application or the catalyst may be affixed to the reactor walls. The actual disinfection of the pathogens occurs as a result of the highly reactive hydroxyl radical generated during the process, placing the technique among advanced oxidation

processes (AOP). Hydroxyl radicals are among the strongest oxidants and are capable of degrading a wide variety of organic and inorganic pollutants [14-18].

The first reported killing of microorganisms, including *L. acidophilus, S. cerevisiae* and *E. coli*, was by Matsunaga et al [19]. Many other researchers have since reported on the use of photocatalysis for water disinfection with much attention given to *E. coli*, largely because it is an indicator of fecal contamination in water systems; see for example [14, 20-29]. Even the more chemically-resistant organisms, such as *Cryptosporidium* and *Giardia*, have been effectively inactivated by photocatalysis [3, 5, 30-32].

Heterogeneous photocatalysis is particularly adaptable for applications in developing countries, especially in remote and rural areas where energy supply may be prohibitive [33]. In addition, TiO_2 is abundant in most countries and relatively cheap, and photocatalysis is not known to produce the potentially harmful byproducts associated with other disinfection processes. The potential for solar application was previously explored for oxidation of chemicals, but Block et al [34] were among the first researchers to explore the use of solar illumination to drive the disinfection process. In addition, the engineering and economic feasibility of these systems were explored in detail by Goswami [35] and Goswami et al. [36]. Although they are not currently in widespread use, solar photocatalytic systems have been used with much success in pilot facilities [17, 37, 38]. Figure 1 and Figure 2 show a solar photocatalytic system operated in Spain [18] and a simplified system layout for flat plate solar reactors.

Nonetheless, as with most treatment options, photocatalytic treatment has its challenges. Firstly, TiO_2 has shown the most promise and has become the most widely used photocatalyst, but it is only sensitized by near UV radiation or photons with greater energy. This means that only a very small fraction of sunlight (<5%) can be used for solar applications. However, the modification of TiO_2 through doping with metals and non-metals to enhance its visible light capability has shown tremendous promise [39-45]. Secondly, slurry reactors are usually more effective than thin films, but they require an additional post-treatment step to separate the catalyst (Figure 1b), adding a level of complexity and increased cost. Thirdly, the rate of disinfection is relatively slow compared to other processes, and like UV and ozone, there is no residual protection in a drinking water distribution system.

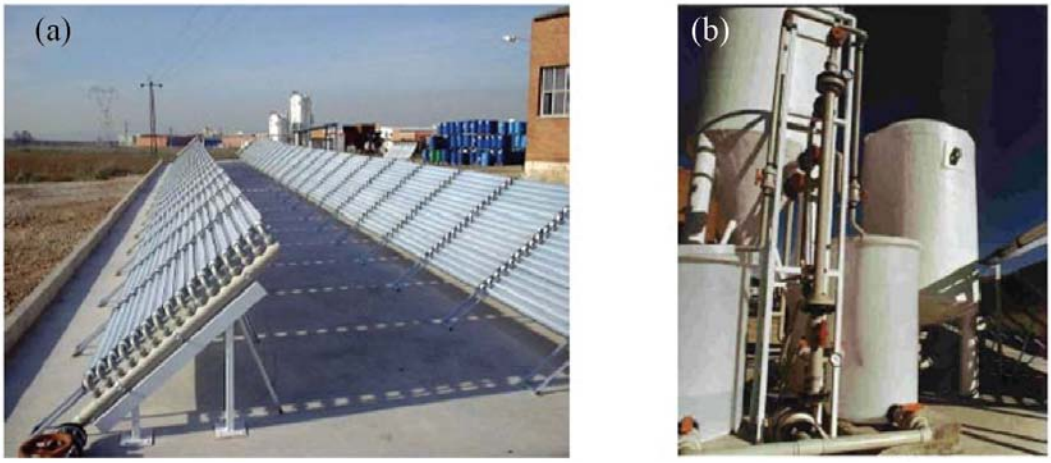

Figure 1: (a) View of a solar collector field and (b) catalyst recovery system (Courtesy of Plataforma Solar de Almería, Spain)

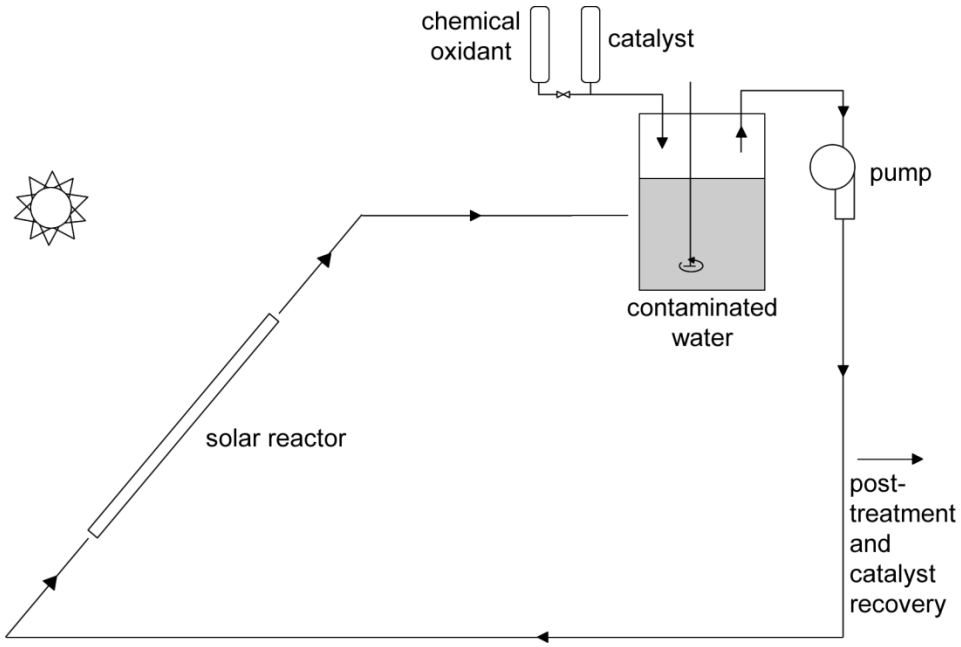

Figure 2: Typical layout of photocatalytic plant for the treatment of water

1.5 Problem statement

The design of a disinfection system relies substantially on the knowledge of the inactivation rate of a target or indicator organism(s) by the disinfectant. For photocatalysis, the synergistic effect of catalyst concentration and light intensity on the rate of the process determines the most efficient combination of contact time and dose to employ. Currently, most of this information is obtained from bench-scale studies and extrapolated with a series of empirical models which do not adequately describe photocatalytic disinfection. The most common application is the Chick-Watson model used primarily to fit inactivation data with first order decay or modified for data with an initial lag.

However, frequent deviations from such models have been reported in the literature [21, 46]. These models do not allow designers to explicitly determine the overall influence of

important parameters such as catalyst concentration, light intensity, ionic strength, and pH on the disinfection process. It is difficult to account for many of the complex interactions which occur during photocatalytic inactivation without over-fitting data with numerous empirical parameters. No study to date has proposed a comprehensive mechanistic model to describe the photocatalytic disinfection which can be used to optimize the design of such systems. A major benefit of a mechanistic model is the significant cost reduction associated with performing fewer preliminary experiments to determine the effectiveness of various combinations of catalyst concentration and light intensity for a given organism.

1.6 Research objective

The objective of this research was to develop and apply a mechanistic modeling approach to describe the kinetics of photocatalytic inactivation for batch reactor systems utilizing suspended TiO_2 particles. The overall goal was to build a model which could account for the influence of catalyst concentration, light intensity, ionic strength, and cell membrane fatty acid distribution on the disinfection process. The aim is that the model will serve as a predictive tool to design disinfection systems, so that water can be disinfected quickly, efficiently and inexpensively.

CHAPTER 2: PHOTOCATALYSIS

2.1 Definition

Heterogeneous photocatalysis is the chemical transformation of a substrate at the interfacial boundary of a solid light-absorbing catalyst (photocatalyst) and a water or gas phase. In this form of photocatalysis, the role of light is to produce active sites on the surface of the photocatalyst so that subsequent chemical reactions may occur [47]. As in catalysis, the catalyst remains unchanged at the end of the cycle [47, 48].

$$catalyst + h\nu \rightleftharpoons catalyst^* \quad (1)$$

$$catalyst^* + A \longrightarrow catalyst + B \quad (2)$$

2.2 Semiconductor band structure

The energy band structure of semiconductors allows the absorption of light and generation of charge carriers (electron and hole) which participate in photocatalysis. Semiconductor photocatalysts include TiO_2, tungsten oxide (WO_3), tungsten sulfide (WS_2), cadmium sulfide (CdS), zinc oxide (ZnO), and zinc sulfide (ZnS) among others. The electrons in the atoms of a semiconductor crystal occupy different energy levels which tend to overlap with those of electrons confined to neighboring atoms. According to the Pauli Exclusion Principle, electron energy levels cannot be the same, the electronic structure becomes characterized by a set of closely spaced energy levels, forming an energy band. When the band structure is analyzed, a series of allowed and forbidden

energies are obtained resulting in energy bands separated by energy band gaps [49]. Although the energy band diagrams of semiconductors are rather complex, they can be simplified since only the electrons in the highest almost-filled band and the lowest almost-empty band dominate the behavior of the semiconductor (Figure 3).

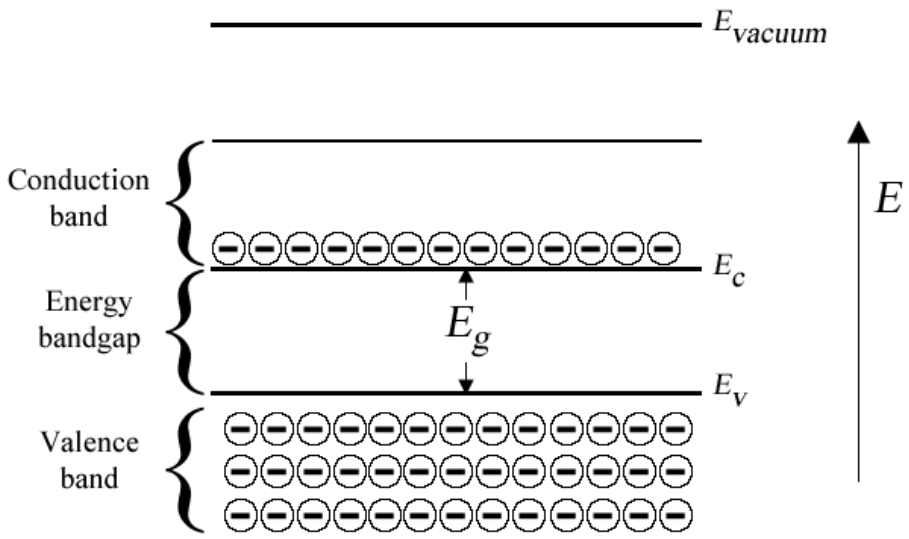

Figure 3: Simplified energy band diagram of semiconductors [49]

The almost-empty conduction band is identified by a set of horizontal lines, the bottom edge of which is labeled E_c. Similarly, the top of the valence band is indicated by a horizontal line labeled E_v. The energy bandgap, E_g, is located between the two bands. The energy of a free electron outside the crystal is called the vacuum level labeled E_{vacuum} [49].

2.3 Electronic excitation and formation of charge carriers

At absolute zero temperature, the valence band is completely filled with electrons while the conduction band is empty. At room temperature, increased thermal energy reduces the band gap slightly as the atomic vibrations increase. This thermal excitation causes some adjustment to the energy distribution of the electrons, such that a few have enough energy to cross the energy band gap into the conduction band [50]. Another process through which electrons can gain energy to cross the band gap is through photoexcitation. In this case, electrons in the valence band absorb the energy from a photon. This is the initiating step in photocatalysis [48, 50]. The photon must provide energy greater than or equal to the band gap for the electron to cross the barrier (Figure 4).

The electrons which break free from bonds between neighboring atoms in the solid and enter the conduction band are free to move around, and hence can conduct charge or participate in chemical reactions. The bonds from which these excited electrons originated are left with electron vacancies, or holes. The holes are considered positive charge carriers which appear to move around freely as neighboring electrons move in and out of the vacancy [49]. The free electron may migrate to a surface site on the semiconductor and participate in a reduction reaction. Similarly, a suitable electron donor at the surface of the material can be oxidized by the valance band hole (Figure 4). If the conduction band electron returns to the valence band and fills the vacancy, the process is called recombination and is accompanied by a release of heat and or fluorescence.

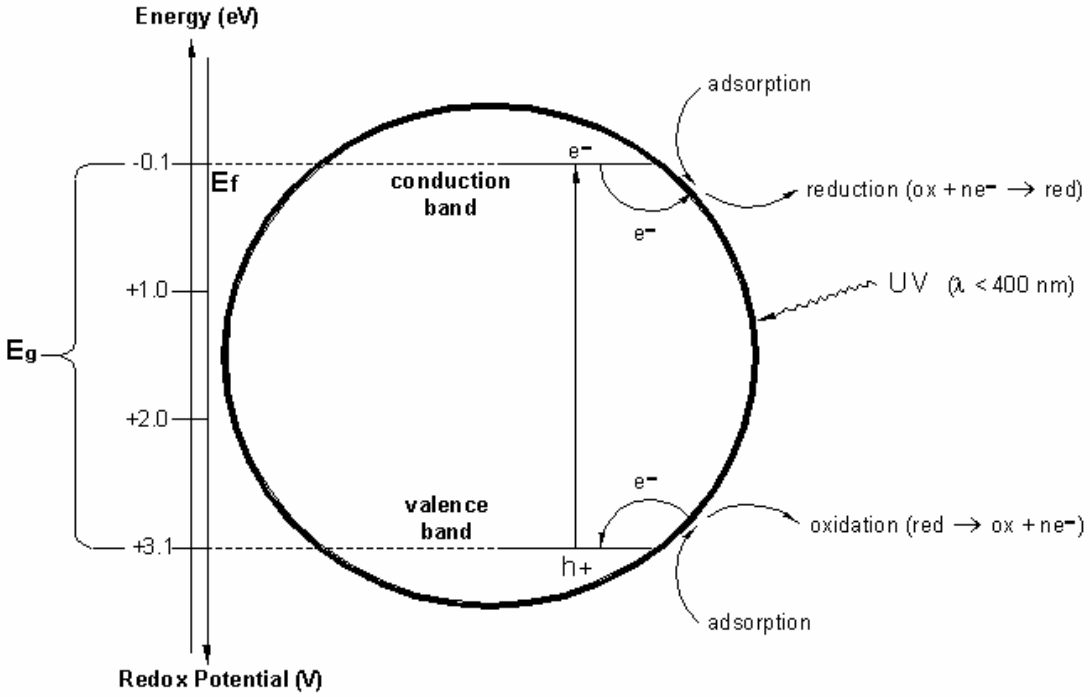

Figure 4: Schematic of photocatalytic processes on the surface of TiO_2. A semiconductor with a band gap of 3.1 eV, TiO_2 requires photons with wavelength less than 400 nm [50].

2.4 Titanium dioxide photocatalyst

TiO_2 is a model photocatalyst because it is non-toxic, stable (does not self-oxidize), and highly active [51]. The conduction and valence bands lie in energetically favorable positions to both reduce and oxidize adsorbed species (Figure 5). A compound is oxidized on the catalyst surface when its oxidation potential is above the valence band position of the catalyst (dark gray rectangle). Similarly, reduction takes place when the redox potential of the acceptor is below the conduction band position (light gray rectangle). According to Figure 5, TiO_2 not only has the oxidation potential to degrade pollutants, but also the reduction potential necessary for splitting water molecules to create hydrogen gas [52].

There are three crystalline phases of TiO_2; anatase, rutile, and brookite. The anatase and brookite phases are known to be thermodynamically less stable than the rutile phase and are generally converted to rutile at high temperature [53-56]. Band structure calculations revealed that rutile and anatase TiO_2 have direct and indirect band gaps, respectively [53]. In a direct band gap semiconductor the conduction band minimum is directly above the valence band maximum, that is, they occur at the same wavenumber [49]. This makes rutile much more efficient at absorbing light than anatase, but charge carriers generated in the anatase phase have longer lifetimes making it more photocatalytically active than rutile. However, anatase is commonly mixed with rutile to help reduce the rate of recombination [48, 51]. The band gap energy of anatase is 3.2 eV and hence absorbs photons of 380 nm or less. Rutile has a slightly lower band gap at 3.1 eV and absorbs into the visible range 418 nm [53, 57].

There is a wide range of photoreactivity within mixtures containing variable contents of anatase and rutile. However, Degussa P25 TiO_2 has set the standard for photoreactivity in environmental applications [50, 58]. It is a non-porous 70% to 30% anatase to rutile mixture [51, 58]. P25 is available as high surface area (50 ± 15 m^2g^{-1}) nanoparticles with an average individual particle size of 20-30 nm, even though particle agglomeration in solution can reach 300-500 nm [51, 59]. The small size of the nanoparticles provides high efficiency of surface trapping of the photogenerated electron and hole, thus increasing the probability of a photocatalytic process on the surface of the catalyst.

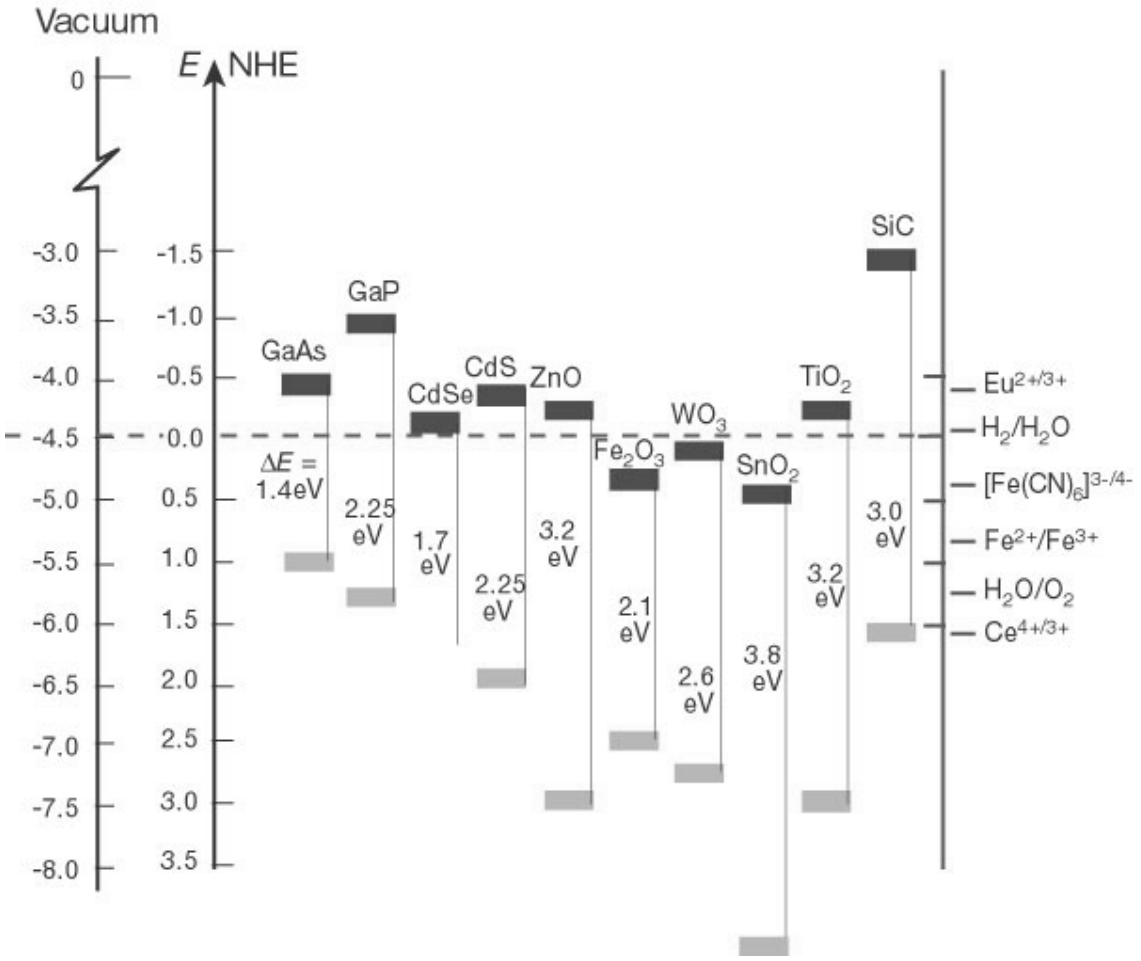

Figure 5: Band positions of several semiconductors in contact with aqueous electrolyte at pH 1. Adapted by permission from Macmillan Publishers Ltd [60].

2.5 Aqueous phase photocatalysis

When a semiconductor is in contact with an aqueous solution, bond formations with water molecules and other ions occur instantaneously. There is a movement of charge between the semiconductor and the solution to create the conditions of equilibrium at the interface of the two phases. This is achieved when the electrochemical potentials of the two phases are equal [49]. The electrochemical potential of the solution is determined by its redox potential, while in semiconductors the electrochemical potential of the electrons is determined by the Fermi level. The Fermi level is the energy

level occupied by electrons at absolute zero temperature or the level at which the probability of occupation of an electron is 50% [49]. On an energy band diagram, the Fermi level would be located at the mid-point of the band gap for intrinsic semiconductors, and just below the conduction band for *n*-type semiconductors such as TiO_2.

The redistribution of charges at the interface produces the space charge region which extends at a considerable distance (100-10,000 Angstroms) below the surface of the semiconductor [49]. Likewise, solute and solvent ions with counter charges are distributed from the surface towards the bulk solution. The exchange of charges also induces changes to the bulk energy levels in the localized area resulting in a curvature to the energy band near the junction. For an *n*-type semiconductor, the Fermi level is typically higher than the redox potential of the aqueous solution, and hence electrons are transferred from the semiconductor into the solution. Therefore, there is a positive charge associated with the space charge region, and this is reflected in an upward bending of the band edges (Figure 6).

Since most of the charge carriers have been removed from the space charge region, electron transfer reactions occur slowly, if at all. However, if the semiconductor is exposed to radiation of sufficient energy, electrons can now be promoted to the conduction band. Electron-hole pairs generated in the region of the electric field, i.e., the space-charge region, are separated efficiently rather than undergoing immediate recombination. This forces the photogenerated electron towards the bulk of the

semiconductor, where it can be transferred through a surface site to a point where an electron acceptor can be reduced. The photogenerated hole, under the influence of the electric field, migrates towards the interface to a site where it can oxidize a suitable electron donor in the solution [50].

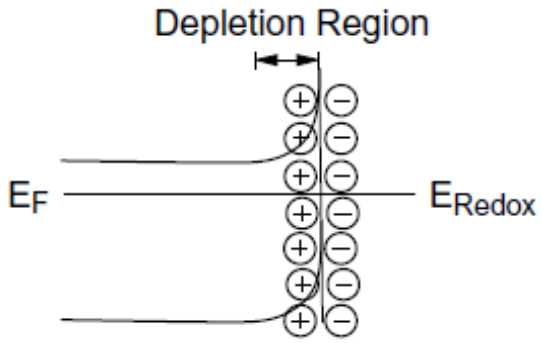

Figure 6: Interface of semiconductor and aqueous solution showing band bending for an n-type semiconductor [49]

The absorption of energy and the subsequent generation of the electron-hole pair are the initiating steps in the photocatalytic process which may be represented as follows [61, 62]:

$$TiO_2 + h\nu \leftrightarrows e^-_{cb}(TiO_2) + h^+_{vb}(TiO_2) \quad (3)$$

where e^-_{cb} is the conduction band electron and h^+_{vb} is the valence band hole.

The interaction of the hole with a water molecule or hydroxide ion produces the very reactive hydroxyl radical (·OH). These radicals are bound or diffuse from the surface of the semiconductor and act as the primary oxidants in the photocatalytic system [61, 63]. The formation of the radicals is illustrated below:

$$H_2O + h_{vb}^{+} \rightarrow \cdot OH + H^{+} \quad (4)$$

$$OH^{-} + h_{vb}^{+} \rightarrow \cdot OH \quad (5)$$

A typical reaction of the bound radical with an organic compound such as glucose may be illustrated as in Equation (6). Bacterial cells are predominantly water and the major cellular constituents, such as polysaccharides, lipids, proteins and nucleic acids are mostly organic. They react with the hydroxyl radical in a similar way and this subsequently leads to cell death.

$$\frac{1}{24}C_6H_{12}O_6 + \frac{1}{4}H_2O + \cdot OH \rightarrow \frac{1}{4}CO_2 + H_2O \quad (6)$$

Oxidation of compounds may also occur directly via the valence band hole before it is trapped either within the particle or at the particle's surface. Nevertheless, the presence of hydroxyl radicals in aqueous solutions of illuminated TiO_2 has been confirmed by researchers and many intermediates are consistent with those found when organic compounds react with a known source of hydroxyl radicals [64-67]. The chemical properties pollutant and the reaction conditions largely determine which mechanism will dominate. However, the presence of hydroxyl radicals is very important for the complete photocatalytic destruction of many organic compounds and the inactivation of pathogens. Cho *et al.* [68] found a linear correlation between hydroxyl radicals and the inactivation of *E. coli* in water disinfection studies.

The photogenerated conduction band electrons are trapped at the surface by Ti^{IV} sites and result in Ti^{III} sites. Oxygen adsorbed at Ti^{III} sites may result in the superoxide radical from a charge transfer reaction as shown below:

$$e_{cb}^{-}(Ti^{III}) + O_2 \rightarrow (Ti^{IV}) + O_2^{\cdot -} \quad (7)$$

The superoxide radical is also relatively reactive and capable of oxidizing cellular constituents. Since all these processes occur simultaneously, photocatalysis may proceed via different pathways depending on the reaction conditions and oxidizable substrates. However, for oxidation of a compound to occur, the presence of oxygen or another suitable electron acceptor (such as hydrogen peroxide) is necessary.

CHAPTER 3: MICROBIOLOGICAL CONTAMINATION OF WATER

3.1 Pathogenic agents of waterborne diseases

Pathogens are a class of microorganisms, including bacteria, viruses, and protozoa, able to cause disease in humans (also plants and animals). The majority of waterborne diseases and infections are caused by bacteria, viruses, and protozoa. Pathogens have genetic, biochemical or structural features which allow them to overcome the defense mechanism of the host, and invade and colonize tissues, or produce toxins. They are transmitted through the direct consumption of contaminated water. In some cases, the consumption of food prepared with contaminated water results in the same infections and diseases [69]. In general, microorganisms are ubiquitous, but pathogens tend to enter water sources particularly through contact with human and animal fecal matter.

3.1.1 Bacteria

Bacterial pathogens include members of the genus *Salmonella* and *Shigella*, cholera-causing *Vibrio cholera*, and some strains of *E. coli*. They are mostly rod-shaped organisms which infect the gastrointestinal tract and are excreted in the feces of infected humans and other animals [70]. However, there are also some waterborne bacterial pathogens, such as *Legionella*, *Burkholderia pseudomallei* and atypical mycobacteria, which can grow in water and soil [69]. *Escherichia*, *Salmonella*, and *Shigella* are genetically closely related [70]. However, while many strains of *Escherichia* are

harmless, members of the *Salmonella* and *Shigella* genus are usually pathogenic. *Escherichia* are almost universal inhabitants of the intestinal tract of humans and warm blooded animals and many species play a nutritional role by synthesizing vitamins, particularly vitamin K [70].

3.1.2 Viruses

Viruses are microorganisms that lack many of the attributes of cells, the most important of which is, they can only reproduce within a living host cell [70]. They are much smaller than bacteria (can range from 10-100 nm), but unlike bacteria, they do not have metabolic abilities of their own. They are also known to infect microbial cells. Waterborne viral pathogens include the hepatitis A virus, poliovirus, adenovirus, and rotavirus among others [1, 69, 71]. Many are excreted in the feces of infected individuals and may contaminate water intended for drinking. Waterborne viral infections often affect the gastrointestinal tract, and among other symptoms, result in severe diarrhea, nausea, and abdominal pain.

3.1.3 Protozoa

Protozoa are eukaryotic cells which are generally larger and structurally more complex than bacteria and viruses. *Cryptosporidium parvum* and *Giardia duodenalis* (previously known as *Giardia lamblia*) belong to this group of pathogens. They live in the intestines of humans and large mammals and pose significant threat to public health [72]. These two organisms are difficult to disinfect because they are transmitted through

water in dormant, resistant forms, known as cysts and oocysts [11, 73]. However, they may be removed through filtration and other advanced treatment techniques [11, 74, 75].

3.2 The model organism: *E. coli*

E. coli is the name given to a group of rod-shaped Gram-negative bacteria which usually inhabit the intestines of humans and warm-blooded animals. Gram-negative bacteria are cells whose membrane thickness and composition do not allow them to retain the gram stain. On the other hand, Gram-positive bacteria easily retain the gram stain. On average, an *E. coli* bacterium measures about 0.5 microns in diameter and 1 micron in length. It is a facultative anaerobe, which can switch from aerobic respiration to fermentation to meet its energy needs.

E. coli is the most studied microorganism in the world. It has found extensive use as a model organism in molecular genetics and molecular biology. However, it is also an excellent model for bacterial pathogens for three important reasons. Firstly, there is a wealth of biological data available for *E. coli*. Secondly, other important pathogens such as Salmonella and Shigella are genetically very similar to *E. coli*. *Salmonella* shares about 50% of its genome with *E. coli*, while *Shigella* shares about 70% [70]. Thirdly, it is easy to culture in the lab and there are many non-pathogenic strains to work with.

3.3 *E. coli* as an indicator of biological contamination

E. coli, along with a number of other similar enteric bacterial species, constitutes the total coliform group. A specific subgroup of this collection is the fecal coliform bacteria, the most common member being *E. coli*. These organisms may be distinguished

from the others by their ability to ferment lactose at 44±0.5°C in the fecal coliform test. In addition, when cultured on a specific plate (e.g. mF Endo) a positive result for *E. coli* is metallic green colonies on a dark purple media (Figure 7).

The presence of fecal coliform bacteria in water is usually an indication that fecal matter from humans or other animals is present. It also suggests that other microorganisms associated with fecal matter, and of more significant virulence, possibly exist. In this way, *E. coli* is used as an indicator organism for the biological contamination of water.

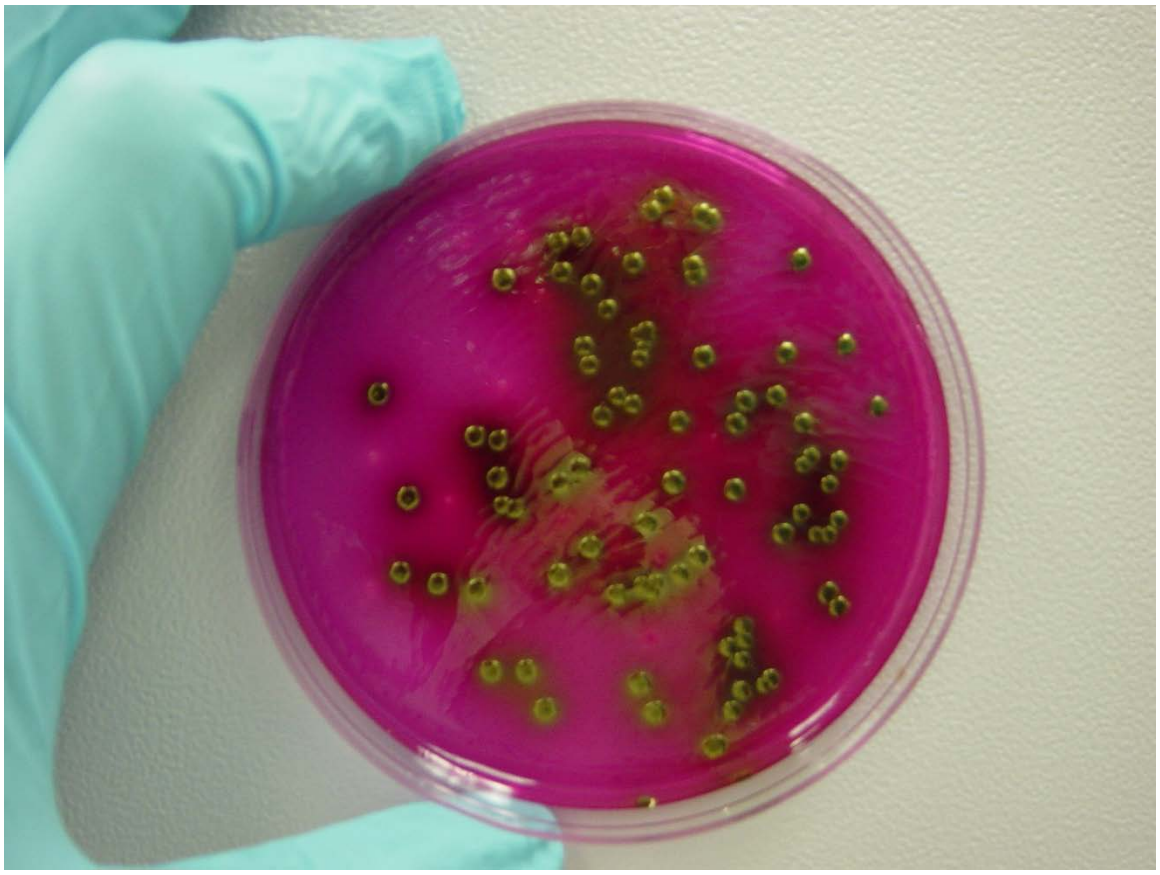

Figure 7: *E. coli* grown on mF-Endo plates in the lab

3.4 Standards for microbial contamination

In the United States (US), the EPA sets the rules and establishes the guidelines for drinking water quality. The Safe Drinking Water Act is the primary federal law that governs the provision of potable water to the public [9]. Under the Act, the EPA has the power to set water quality standards. The Agency uses the Total Coliform Rule, published in 1989, to establish microbiological standards for public water systems [76]. The rule sets both non-enforceable maximum contaminant level goals (MCLG) and legal maximum contaminant limits (MCL) for the presence of total coliform in drinking water. The MCLG for total coliform, which includes *E. coli*, is set at zero. The MCL is based on the presence/absence of total coliforms in samples rather than actual counts of bacteria. For water systems which take less than 40 routine samples per month, 39 must be negative for total coliform. For water systems taking more than 40 samples per month, 95% must be negative for total coliform. The number of routine samples per month is determined by the number of consumers that the water system serves. Currently, the EPA is proposing the elimination of the MCLG and MCL provisions for total coliforms and fecal coliforms, and the inclusion of an MCLG and MCL for *E. coli* and a treatment technique for total coliforms [77].

The World Health Organization (WHO) provides guidelines to assist countries in verifying drinking water quality. The guidelines are very similar to the US EPA requirements in that *E. coli* is the indicator organism of choice and the overall goal is to have no indicator organisms present in drinking water. However, WHO suggests that thermo-tolerant coliforms may be used as an alternative to the test for *E. coli* in many

circumstances. The WHO guideline value for microbial quality is the absence of an indicator organism in 100-ml samples [71].

CHAPTER 4: MICROBE-CATALYST INTERACTIONS

4.1 Introduction

For photocatalytic disinfection to occur, microbes must be in close proximity or make contact with the surface of the semiconductor to allow for the exchange of electrons and subsequent chemical reactions. Although TiO_2 has been studied extensively to disinfect microorganisms, most of what is known about microbe-catalyst interactions in aqueous suspensions is qualitative. No study has quantitatively assessed the significance of these interactions on the disinfection process. The important concepts which are related to microbe-catalyst interactions are discussed in this section. Since *E. coli* is the subject of the investigation, the scope of the discussion has been limited to bacteria.

4.2 Catalyst surface electrochemistry

The surface of a metal oxide particle in an electrolyte solution is almost always electrically charged. Upon exposure to water, there is a spontaneous formation of an adsorbed water layer of oriented water dipoles [78, 79]. The terminal oxygen atoms at the surface react with water to produce hydroxylated sites (Figure 8), which are involved in proton exchange reactions imparting a pH-dependent surface charge [80-82]. In the case of TiO_2, the hydroxyl groups on the surface are known to undergo the following acid-base reactions [50]:

$$\equiv \mathrm{TiOH_2^+} \overset{K_{a1}^S}{\longleftrightarrow} \equiv \mathrm{TiOH} + \mathrm{H^+} \tag{8}$$

$$\equiv \mathrm{TiOH} \overset{K_{a2}^S}{\longleftrightarrow} \equiv \mathrm{TiO^-} + \mathrm{H^+} \tag{9}$$

where K_{a1}^S and K_{a2}^S are the surface acidity constants, which are related to the acidity constant in the bulk solution as [50, 83]:

$$K_{a1}^S = K_{a1}^{bulk}\left(\frac{e\psi_0}{k_B T}\right) \tag{10}$$

$$K_{a2}^S = K_{a2}^{bulk}\left(\frac{e\psi_0}{k_B T}\right) \tag{11}$$

where ψ_0 is the surface potential, e is electron charge, k_B is the Boltzmann constant and T is absolute temperature. The pH-dependence of the dominant surface species for TiO_2 is shown in Figure 9. The surface is known to have a net surface charge of zero close to pH 6 when the neutral TiOH species covers most of the surface sites [84-86].

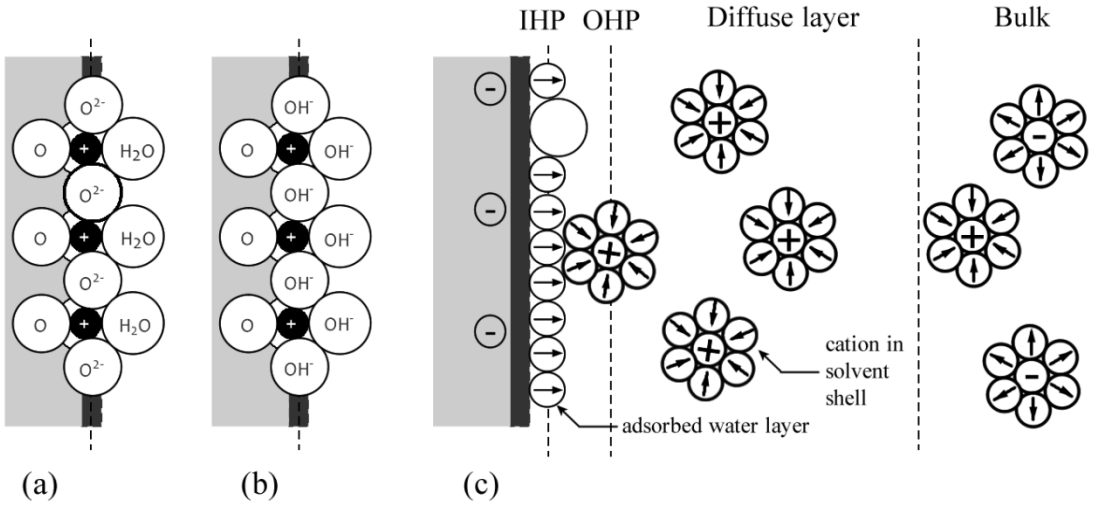

Figure 8: TiO_2 surface in water: (a) water layer [80]; (b) hydroxylated surface [80]; and (c) schematic of double layer according to Stern-Grahame model [87]

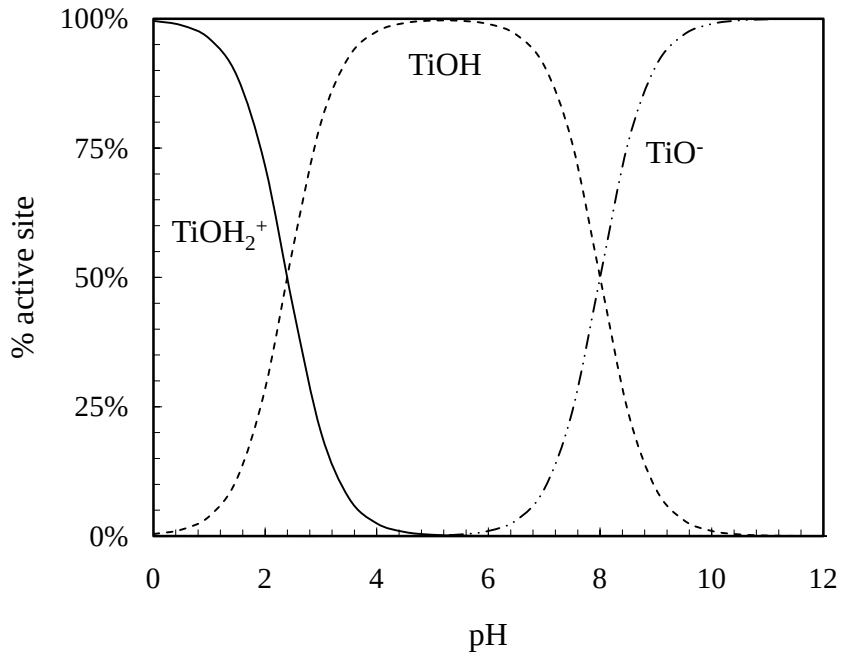

Figure 9: Surface hydroxylated species of TiO_2 a function of pH calculated according to equations (8) and (9) using pK_{a1}^{S}= 2.4 and pK_{a2}^{S}= 8 as determined by Korman et al [86] for Degussa P25 at 25ºC

The adsorption of organic molecules or surface-active ions may also occur at the surface. The distribution of the electrolyte ions at the interface and the electric potential play a key role in the stability of catalyst suspensions during photocatalysis [88-91], as well as their post-treatment recovery [92, 93]. Figure 8 schematically shows the electric double layer at the TiO_2 surface in contact with a solution according to the Stern-Grahame model [94, 95]. Species are attracted to localized surface sites via electrostatic or hydrophobic effects and displace the primary adsorbed water layer, becoming specifically adsorbed on the oxide surface [96-98]. This type of short-range interaction is generally called specific adsorption and the ions lose a portion of their hydration shell to become part of the monolayer at the surface. This is particularly the case for anions, since the hydration energies are generally higher for cations [99]. The specific adsorption of

chloride, sulfate, and phosphate ions has been observed on the surface of TiO_2 [100, 101]. The plane of mean charge of the specifically adsorbed ions defines the inner Helmholtz layer (IHL). The amount of specifically adsorbed charge per unit area σ_{ads} can be expressed using a modified Langmuir isotherm [50]:

$$\sigma_{ads} = \frac{zeCN_{ads}\exp\left(-\frac{\Delta G_{ads}}{k_B T}\right)}{1 + \exp\left(-\frac{\Delta G_{ads}}{k_B T}\right)} \tag{12}$$

in which ΔG_{ads} is the Gibbs energy of adsorption per molecule according to,

$$\Delta G_{ads} = ze\psi_0 + \Delta G_{spec} \tag{13}$$

where $ze\psi_0$ represents the electrostatic interaction energy and ΔG_{spec} is the Gibbs energy of specific interaction. N_{ads} is the number of adsorption sites per unit area. *C* and *z* are the bulk concentration and the valence of specifically adsorbing ions, respectively.

Some ions are adsorbed to the surface through long-range coulombic interactions. They tend to retain their hydration layer and are therefore restricted in their approach to the surface. The mean geometric location of their charge centers defines the outer Helmholtz layer (OHL). The IHL and OHL together constitute the Stern layer. Beyond this region lies the so-called diffuse layer in which ions are fully mobile, and whose spacing from one another is a function of the total ionic concentration in bulk solution. The concentration of ions in this layer is governed by the need to maintain overall charge neutrality, including those species adsorbed at the surface of the metal oxide. The concentration of ions in the diffuse layer is described by the Boltzmann distribution,

$$C_i(x) = C_i^{bulk} \exp\left(-\frac{z_i e\psi(x)}{kT}\right) \tag{14}$$

where C_i is molar concentration (mol L^{-1}) of the ion in the double and C_i^{bulk} is the concentration in the bulk solution. The electrostatic potential of the double layer is given by the Poisson distribution:

$$\nabla^2\psi = -\frac{\rho_e}{\varepsilon} \tag{15}$$

where ρ_e is the charge density given as,

$$\rho_e = \sum_{i=1}^{N} C_i z_i e \tag{16}$$

and ε is the dielectric permittivity of the solution. Using equations (15) and (16), the Poisson-Boltzmann equation for the electric potential profile is derived as,

$$\nabla^2\psi = -\frac{e}{\varepsilon}\sum_{i=1}^{N} C_i^{bulk} z_i \exp\left(-\frac{z_i e\psi}{kT}\right) \tag{17}$$

Equation (17) is restricted to low electrolyte solutions because the ions are treated as point charges. Using the Debye-Huckel approximation for low potential, i.e., $ze\psi \ll kT$, the electric potential profile is given as,

$$\nabla^2\psi = \kappa^2\psi \tag{18}$$

where κ is the Debye-Huckel parameter and is given by,

$$\kappa = \sqrt{\frac{e^2}{\varepsilon kT}\sum_{i=1}^{N} C_i^{bulk} {z_i}^2} \tag{19}$$

The solution for equation (18) for a double layer around a spherical particle of radius *a* is given as [102],

$$\psi = \psi_d \frac{a}{x} \exp\big(-\kappa(x-a)\big) \tag{20}$$

in which the potential ψ_d is the potential difference across the diffuse part of the double layer, which is related to the charge density σ_d in the double layer through,

$$\sigma_d = \varepsilon \frac{1+\kappa a}{a} \psi_d \tag{21}$$

The total surface charge Q_e is given as,

$$Q_e = 4\pi\varepsilon a(1+\kappa a)\psi_d \tag{22}$$

The total surface charge and electrostatic potential of the surface are determining factors for behavior of the colloids in suspension. Particles of similar charge tend to be stabilized as they repel each other. If particles have no charge, there is usually no force to prevent their agglomeration.

4.3 Bacterial cell surface electrochemistry

The surface of a bacterium is much more complex than the surface of impenetrable solid colloids. A bacterial surface is a heterogeneous three-dimensional arrangement of various biomolecules. The surface properties may vary at specific locations as a result of the presence of certain structures. Some cells also have structures that protrude from the surface such as fimbriae, pili, and flagella. Fimbriae and pili are thought to be involved in cell attachment to environmental surfaces, while flagella are special structures used for cell locomotion [70]. To understand cell electrochemistry, a brief description of the cell surface is necessary.

4.3.1 Structural composition of bacterial surface

The outer surface of a bacterial cell is made up of a cell wall and cytoplasmic membrane which encircles the fluid cytoplasm (Figure 10). The cytoplasm is a complex mixture of substances and structures including deoxyribonucleic acid (DNA), ribonucleic acid (RNA), ribosomes, and other dissolved and suspended materials. The cell wall and cell membrane act as barriers to prevent unwanted materials from entering the cell, while also holding the internal contents together. Only water and a few other small, uncharged molecules like oxygen and carbon dioxide diffuse freely across the membrane. All other substances enter through active transport or diffuse through trans-membrane proteins, whose channels open and close according to the needs of the cell.

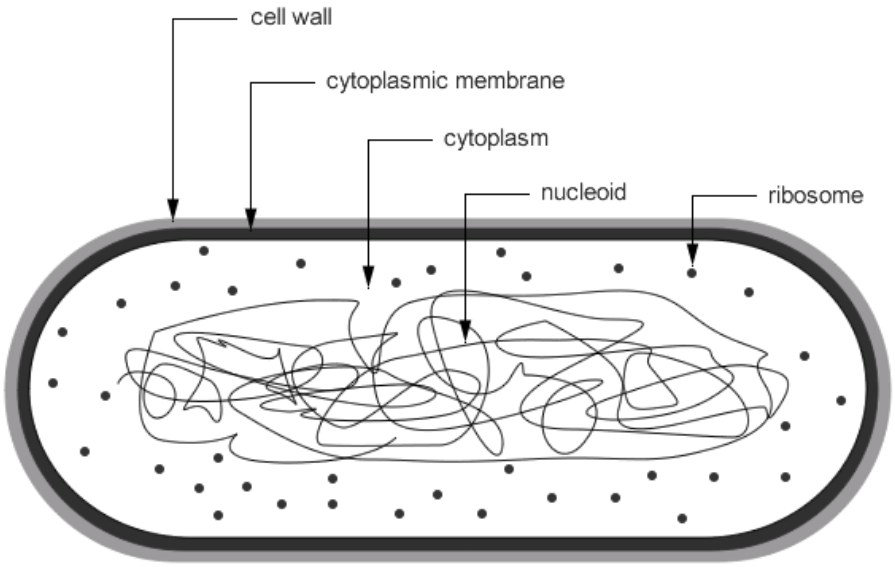

Figure 10: Typical bacterial cell structure (not to scale) [70]

These outer layers are the primary means through which an organism interacts with the environment. Most species of bacteria can be divided into two broad groups based on their cell wall by the Gram-staining method simply as Gram-positive and Gram-negative [70]. Figure 11 shows the structure of bacterial cell surfaces. The cell wall of both groups is composed of peptidoglycan, a peptide-cross-linked polysaccharide matrix layer. The peptidoglycan layer is made up sheets formed from individual strands of peptidoglycan lying adjacent to one another. It accounts for as much as 90% of the Gram-positive cell wall with several (up to 25) sheets stacked upon each other to height of 15-80 nm. In Gram-negative bacteria, it makes up only about 10% of the cell wall (1-2 nm) and is located between the two phospholipid layers; the outer membrane and the cytoplasmic membrane. Peptidoglycan confers rigidity to maintain shape and internal pressure. In both Gram-negative and Gram-positive bacteria, peptidoglycan is very porous and allows particles of approximately 2 nm to pass through [103].

Approximately 45% of the surface of Gram-negative bacteria may be covered with lipopolysaccharide (LPS), which are anchored in the lipids of the outer membrane. It is made up of three distinct regions covalently linked together; a hydrophobic lipid component (lipid A), a core polysaccharide, and *O*-antigen. Some bacterial strains may not possess the *O*-antigen side chain. The LPS core polysaccharide consists of five to ten negatively charged sugar units, which often carry phosphate and carboxylic acid groups. The *O*-antigen consists of 20 to 70 repeating units of three to five sugars, which protrude up to 30 nm or more from the cell surface. It is very likely that the *O*-antigen plays a

major role in polymer interactions with surfaces reported for Gram-negative bacteria [104].

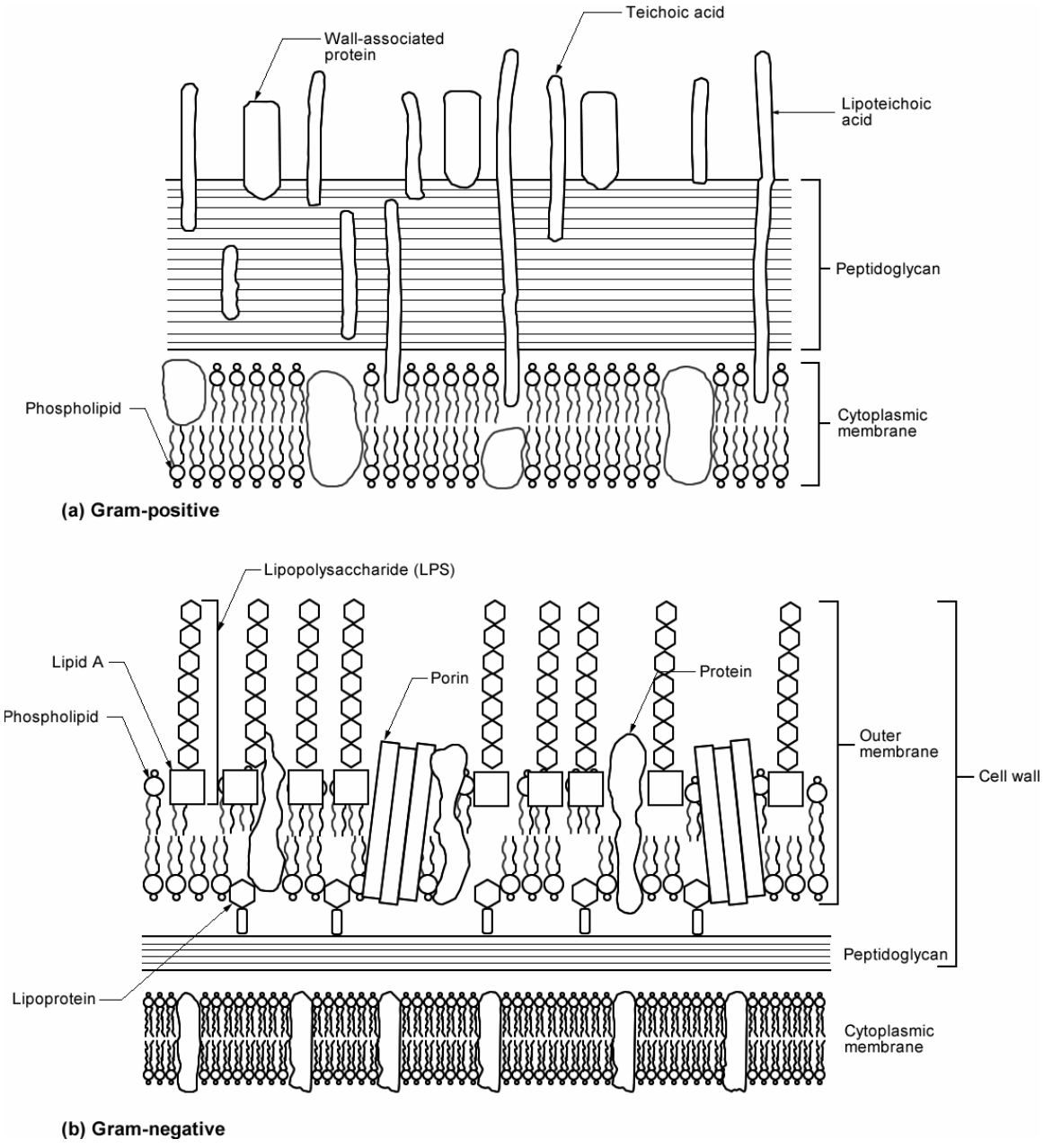

Figure 11: Outer layers of bacteria. Adapted by permission from Pearson Education, Inc. [70]

Similar to the LPS in Gram-negative bacteria, the cell wall of Gram-positive bacteria may contain teichoic acids which are attached, directly or indirectly by way of phosphodiester bonds, to carbon 6 of *N*-acetylmuramic residues of the peptidoglycan, or anchored in the underlying lipid bilayer. In the latter case, these are called lipoteichoic acids and are covalently bound to the lipid bilayer via a glyceride. In general, teichoic acids include all wall, membrane, or capsular polymers of either ribitol phosphate or glycerophosphate residues. They are connected via phosphodiester bonds and usually have other sugars and D-alanine attached.

Both Gram-negative and Gram-positive bacteria have a cytoplasmic membrane composed almost entirely of lipids and proteins. In Gram-negative bacteria, a second phospholipid bilayer is present in the outer cell membrane. Phospholipid bilayers are composed of conventional glycerol-phospholipids, mainly phosphatidylethanolamine (PE), phosphatidylglycerol (PG), and cardiolipin [105-107]. Phospholipids have a hydrophobic head and two hydrophobic tails and are arranged in a two-layer sheet with the tails pointing towards the center of the layer. The head of the lipid is generally made up of a negatively charged phosphate group and glycerol. The tail is usually a long chain of fatty acid hydrocarbons.

Finally, the cell wall and cytoplasmic membrane are populated with proteins which are either firmly embedded (integral proteins) or associate firmly with one of the membrane structures (peripheral proteins). Some proteins bind substrates or process large

molecules for transport into the cell, while lipoproteins are involved in energy metabolism and other important cellular functions.

4.3.2 Surface charges and ionizable functional groups

Much of the charge on a bacterial cell surface is derived from functional groups associated with the surface structures. Bioassay studies suggest that the charge on the cell wall results predominantly from proton exchange reactions involving carboxylic, phosphate, and amino moieties [108-111]. The reactions for the dominant functional groups in *E. coli* and the range of their associated acidity constants (pK_a) are shown in Table 1.

Table 1: Ionizable functional groups located on the surface of *E. coli* and the associated acidity constants (pK_a) for zero salt effects at 25ºC. Data compiled from Martinez et al [109] and Jiang et al [111].

Reaction	Location	pK_a
$\text{R-COOH} \leftrightarrow \text{R-COO}^- + \text{H}^+$	Proteins, sugars and LPS	2.0 - 6.0
$\text{R-NH}_3^+ \leftrightarrow \text{R-NH}_2 + \text{H}^+$	Proteins and phospholipids	9.0 - 11.0
$\text{R-HPO}_4 \leftrightarrow \text{R-PO}_4^- + \text{H}^+$	Phospholipids	3.2 - 3.5
$\text{R-H}_2\text{PO}_4 \leftrightarrow \text{R-HPO}_4^- + \text{H}^+$	LPS	3.2 - 3.5
$\text{R-HPO}_4^- \leftrightarrow \text{R-PO}_4^{2-} + \text{H}^+$	LPS	5.6 - 7.2

Considering that the site density of carboxyl and phosphate groups is generally greater than amines, the cell surface of *E. coli*, like most bacterial cells, is negatively charged at neutral pH [109, 112]. In the absence of other ions, the surface charge density resulting from the ionizable functional groups at the bacterial surface may be derived by considering the generic proton exchange reactions,

$$\mathrm{LH} \overset{K_a^{acid}}{\longleftrightarrow} \mathrm{L^-} + \mathrm{H^+} \tag{23}$$

$$\mathrm{LH^+} \overset{K_a^{base}}{\longleftrightarrow} \mathrm{L} + \mathrm{H^+} \tag{24}$$

where L is the proton-binding site on the cell surface for acidic and basic moieties respectively. The apparent equilibrium constants (K_a) for equations (23) and (24) are defined as,

$$K_a^{acid} = \frac{[\mathrm{H^+}][\mathrm{L^-}]}{[\mathrm{LH}]} \tag{25}$$

$$K_a^{base} = \frac{[\mathrm{H^+}][\mathrm{L}]}{[\mathrm{LH^+}]} \tag{26}$$

The fixed surface charge ρ_{fix} associated with the various sites is given by,

$$\rho_{fix} = e\sum_{i=1}^{m}\left(\frac{L_{TB,i}[\mathrm{H^+}]}{K_{a,i}^{base} + [\mathrm{H^+}]}\right) - e\sum_{j=1}^{n}\left(\frac{L_{TA,i}K_{a,j}}{K_{a,j}^{acid} + [\mathrm{H^+}]}\right) \tag{27}$$

where L_{TB} and L_{TA} are the total concentrations of basic and acidic sites, respectively. The acidity constants associated with each site must be adjusted according to Equations (10) and (11) to account for the electrostatic influence of the surface.

4.3.3 Electric double layer at bacterial surface

Since a bacterial surface has a three-dimensional configuration into which ions and solvent molecules are able to penetrate, the bacteria-water interface may best be described as an ion-penetrable layer with volume spread electric charge [113-117]. Figure 12 schematically shows the distribution of ions at the bacterial surface according to the ion-penetrable model. The charges associated with the ionizable functional groups attract counter ions, but there is no definite boundary at the molecular level. Polymers and surface appendages may also change conformation depending on the ionic character of the microscopic local environment [112, 118]. Unlike a hard colloidal particle, the bacterial surface has a finite thickness which restricts the charges within the ion-penetrable layer. Surface charge density may be deduced from proton titration experiments [110]. However, since it is difficult to determine the spatial distribution of the charge through the cell membrane, it is usually assumed to be uniformed.

The electric potential of the ion-penetrable layer is made up of the fixed charges associated with functional groups, as well as the charge density of the ions which have diffused into the layer [117]. To derive the electric potential within the layer, Equation (15) may be adjusted appropriately as follows

$$\nabla^2\psi = -\frac{\rho_{fix}(x) + \rho_{el}(x)}{\varepsilon_m} \tag{28}$$

where ρ_{el} is the charge density contribution of the ions in the ion-penetrable layer and ε_m is the dielectric constant within the membrane layer. The ions in the membrane have an energy which is equal to $ze\psi$ and follow the Boltzman distribution. Therefore, the

concentration of ions in the ion-penetrable membrane is given by Equation (14). The semi-permeable cytoplasmic membrane maintains an unequal distribution of ions on either side of the membrane. At equilibrium, the electrostatic potential across the membrane is called the Donnan potential, ψ_{DON}. Equation (14) may therefore be rewritten as,

$$C_i^{mem} = C_i^{bulk} \exp\left(-\frac{z_i e \psi_{DON}}{kT}\right) \tag{29}$$

To satisfy conditions of charge neutrality in the membrane, the following is true

$$\rho_{fix} + eN_A \sum_{i=1}^{N} C_i^{bulk} z_i \exp\left(-\frac{z_i e \psi_{DON}}{kT}\right) = 0 \tag{30}$$

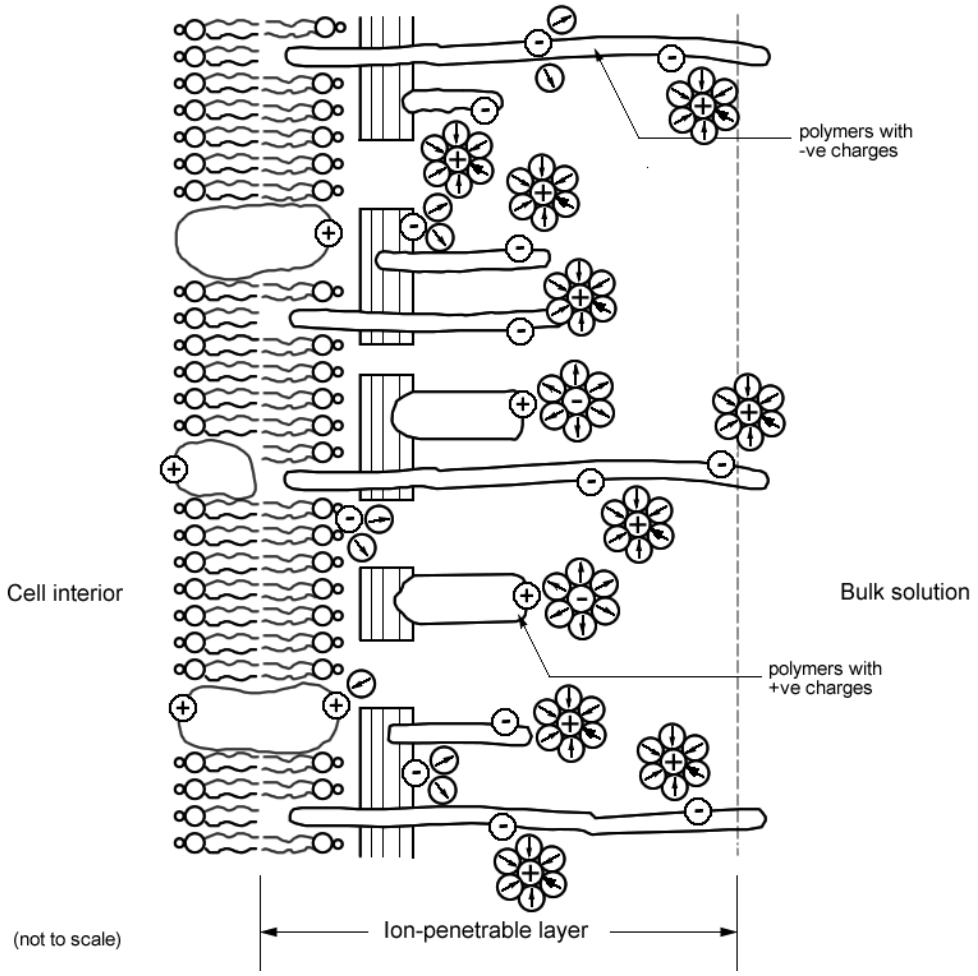

Figure 12: Schematic of bacteria-water interface [113]

A particular solution for Equation (30) gives the Donnan potential for a membrane in contact with a 1-1 electrolytic solution as [116],

$$\psi_{DON} = \frac{kT}{e}\operatorname{arcsinh}\left(\frac{\rho_{fix}}{2n^{bulk}F}\right) \tag{31}$$

where F is the Faraday constant.

Various approaches have been taken to derive the electric potential across the cell membrane. A useful approach is to assume infinite thickness of the membrane, even though the solution indicates that the electric field only exists within a finite thickness of the membrane [119]. However, the origin ($x = 0$) is located at a hypothetical boundary between the membrane and the electrolyte solution such that $x < 0$ represents the membrane, and $x > 0$ is the electrolyte solution. The Poisson-Boltzmann equation for this model is given as,

$$\frac{d^2\psi}{dx^2} = -\frac{1}{\varepsilon_s \varepsilon_o}\left\{\rho_{fix} + eN_A \sum_{i=1}^{N} n_i^{bulk} z_i \exp\left(-\frac{z_i e\psi}{kT}\right)\right\} \text{ for } x < 0 \quad (32)$$

$$\frac{d^2\psi}{dx^2} = -\frac{1}{\varepsilon_s \varepsilon_o}\left\{eN_A \sum_{i=1}^{N} n_i^{bulk} z_i \exp\left(-\frac{z_i e\psi}{kT}\right)\right\} \text{ for } x > 0 \quad (33)$$

where ε_m and ε_s are the relative dielectric constants of the membrane and the solution respectively. Equations (32) and (33) can be solved numerically after applying the appropriate boundary conditions [117, 119, 120] to yield the electric potential profile across a cell membrane.

4.4 Microbe-catalyst electrical double layer interactions

Since contact between the catalyst and the microbe is a prerequisite for photocatalysis, interactions which enhance contact without destabilizing the suspension should result in more effective disinfection. The interaction between the two colloids, as described by classical DLVO theory [121], is governed by the balance of repulsive and attractive forces, usually summed up in electrostatic and van der Waals forces. Electrostatic forces can be both repulsive and attractive depending on the overall charge

of the colloids, while van der Waals interactions are usually attractive. Bacterial surface polymers may also play a major role during the interaction [112, 113, 122-124].

For simplicity, it may be assumed that both catalyst and microbes are spherical particles (even though *E. coli* is rod-shaped). It is likely that given the relative size of a bacterium to an individual TiO_2 particle, that the system may best be described as a hard spherical particle interacting with an ion-penetrable plate. However, for generality, both particles will be considered spheres (Figure 13). Taguchi et al [125] calculated the potential energy for the interaction between a sphere covered with an ion-penetrable membrane and a solid spherical particle. Many other cases can be found in the literature which describes specific interactions [126-129], particularly the interaction of a spherical particle covered with an ion-penetrable layer and a flat solid plate [129]. The latter may be applicable to thin film photocatalysis systems.

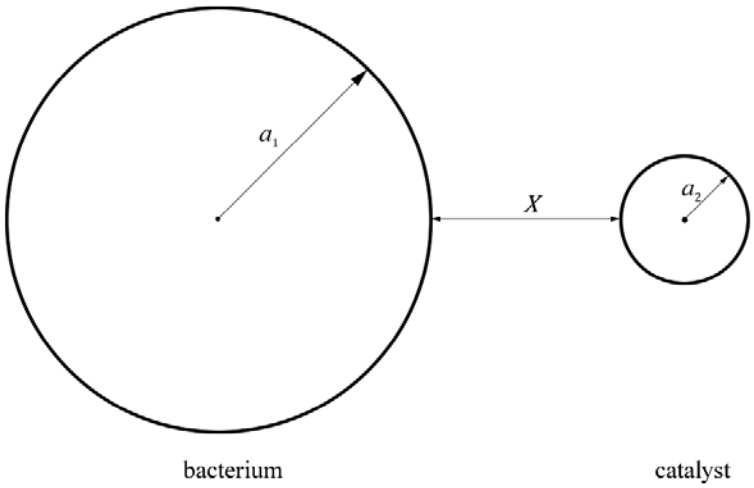

Figure 13: Proposed model for the interaction between a bacterium and a catalyst particle of radii a_1 and a_2 respectively, separated by X between their surfaces

The total potential energy V_T of two spherical particles is given by the sum of their van der Waals and electrostatic interaction energies [125, 127],

$$V_T(X) = V_v(X) + V_e(X) \tag{34}$$

Consider two spheres of radii a_1 and a_2 separated at a distance X (Figure 13). The potential energy for van der Waal interaction between the two particles is given as,

$$V_v(X) = \frac{a_1 a_2}{a_1 + a_2} \frac{A}{6X} \tag{35}$$

where A is the Hammaker constant. The potential energy of double layer interaction between the two spheres is

$$V_e(X) = \frac{2\pi a_1 a_2}{a_1 + a_2} \int_X^\infty V_{pl}(x)\, dx \tag{36}$$

where $V_{pl}(x)$ is the potential energy of the electrostatic interactions per unit area between two plates at separation x. During the interaction of the double layers, two cases are introduced for the solid particle [125, 127, 129]; (1) constant surface potential; and (2) constant surface charge. The potential inside the organism may be assumed to remain constant at the Donnan potential. Terui et al [126] derived V_{pl} for solid particles under assumptions (1) and (2) above interacting with an ion-penetrable particle, respectively,

$$V_{pl}(x) = 2\varepsilon_r \varepsilon_o \kappa \left[\psi_1 e^{-\kappa x} \psi_2 - \frac{1}{2} (\psi_1)^2 e^{-2\kappa x} \right] \tag{37}$$

$$V_{pl}(x) = 2\varepsilon_r \varepsilon_o \kappa \left[\psi_1 e^{-\kappa x} \psi_2 + \frac{1}{2} (\psi_1)^2 e^{-2\kappa x} \right] \tag{38}$$

By substituting equations (37) and (38) into (36), the potential energy of double layer interaction for a bacterium with TiO_2 particle under the constant potential assumption is,

$$V_e(X) = \frac{4\pi a_1 a_2}{a_1 + a_2} \varepsilon_r \varepsilon_o \left[\psi_1 e^{-\kappa x} \psi_2 - \frac{1}{4} (\psi_1)^2 e^{-2\kappa x} \right] \tag{39}$$

and under the constant surface charge assumption is,

$$V_e(X) = \frac{4\pi a_1 a_2}{a_1 + a_2} \varepsilon_r \varepsilon_o \left[\psi_1 e^{-\kappa x} \psi_2 + \frac{1}{4} (\psi_1)^2 e^{-2\kappa x} \right] \tag{40}$$

These reactions are important as they define the potential energy of interaction between the suspended colloids. The net interaction energy gives an indication of the colloidal suspension. If the interaction is dominated by van der Waals, then overwhelming attractive forces can lead to irreversible coagulation. If the electrostatic forces dominate, then the particles should be stabilized.

CHAPTER 5: REVIEW OF WATER DISINFECTION MODELING

5.1 Introduction

There have been few attempts to define specific models for photocatalytic disinfection, with most of the current applications based primarily on chemical disinfection. The modeling of water disinfection is important to establish the process kinetics of a specific disinfectant with particular microorganisms. In general, water disinfection modeling began as a purely empirical science based on the principles expressed in Chick's law [130]. Chick observed that under certain conditions, the inactivation kinetics of microorganisms closely mirrored chemical reactions. Therefore, the fundamental laws governing chemical reaction kinetics were applied to reactions involving microorganisms and a chemical disinfectant. For a constant disinfection concentration, Chick concluded that the rate of disinfection is proportional to the concentration of microorganisms, thus:

$$r = -kN \tag{41}$$

where r is the rate of disinfection given as the number of microbes per volume per unit time, N is the concentration of organisms (cells per unit volume), while k is a rate constant, which varies with the nature and concentration of the disinfectant. In a simple batch reactor, the solution of Equation (41) is an exponential decay curve, where N_0 is the initial count of bacteria.

$$\frac{N}{N_0} = \exp(-kt) \tag{42}$$

Chick's model is a very simplistic formulation, but it has found extensive application where chemical disinfectants such as chlorine, ozone, hydrogen peroxide and chloramines are used [131]. In addition to its simplicity, it is restricted to first order kinetics, which is just one, and very often, a seldom case in practical disinfection [132]. Even though it is based on homogeneous reactions, some researchers have applied Chick's formulation to calculate disinfection rate constants for photocatalytic inactivation of viruses and coliform bacteria [27].

Disinfection models can be classified into two broad groups, empirical and mechanistic. Empirical models are mathematical expressions aimed at replicating the observed behavior of inactivation curves. Such curves can take a variety of shapes as shown in Figure 14. The combination of a number of factors may be responsible for producing each curve, but empirical models are not concerned with the underlying mechanisms. They are applied in areas where the kinetics of a disinfectant is well established. On the other hand, in the mechanistic approach a specific inactivation mechanism is first defined and then the model is developed. These models tend to be more robust than empirical models, which often cannot be extended beyond the data with which they are calibrated. Mechanistic models can be more flexible and allow the incorporation of many variables. However, microbial inactivation is extremely complex and depends on a wide range of defined and undefined variables [133]. This means that even mechanistic models are simplifications and often require empirical approaches to complete them.

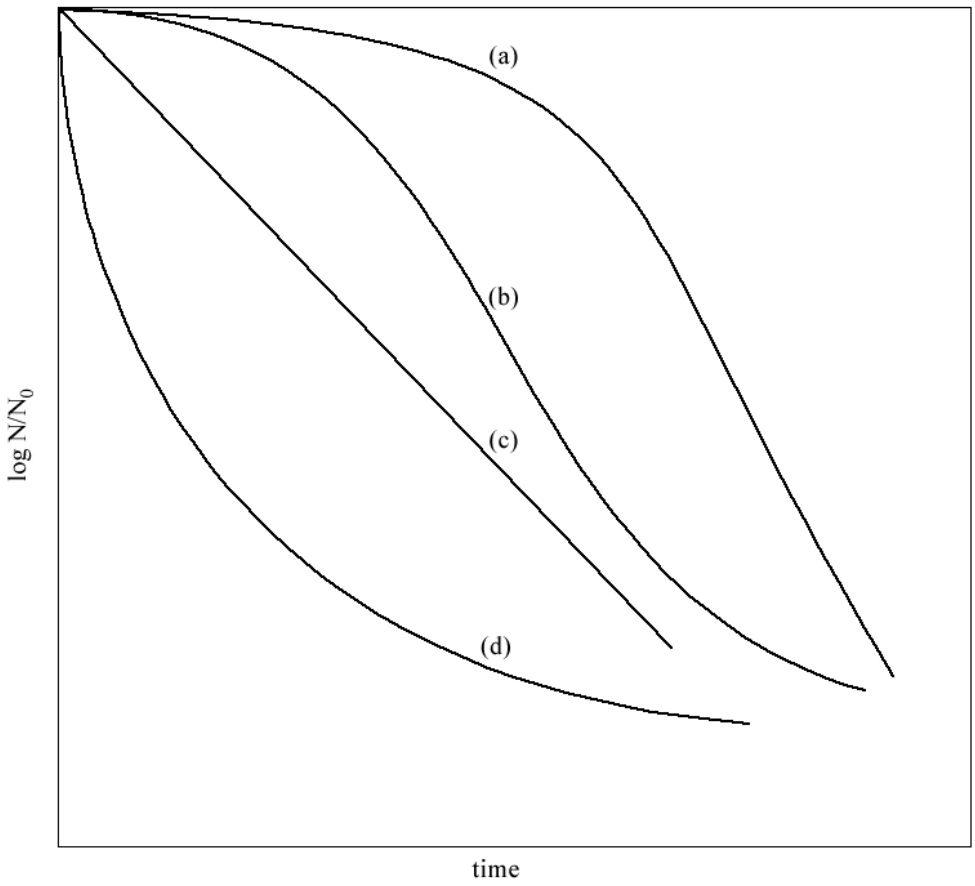

Figure 14: Typical bacterial inactivation curves: (a) lag-survival followed by exponential decay; (b) sigmoidal; (c) exponential (log-linear); and (d) concave downward

5.2 Empirical models

5.2.1 Chick-Watson model

Watson [134] found that under first order kinetics the relationship between the concentration of a chemical disinfectant and the time of exposure was a constant that produced a specific level of inactivation. Thus,

$$c^d t = constant = \lambda \tag{43}$$

In the above equation, d is the coefficient of dilution and c is the disinfectant concentration. This led to the development of CT values, which allow practitioners to calculate how much disinfectant is required to adequately disinfect water, given certain microorganisms and under specified conditions [135]. Assuming no disinfectant demand (i.e., c and n are constants), then the Chick-Watson model for a batch system is given by:

$$\frac{N}{N_0} = \exp\left(-kc^d t\right) \tag{44}$$

Rincón et al [136] demonstrated that the model can sometimes fit observed data for photocatalytic inactivation. The inherent assumption is that the disinfectant concentration during photocatalysis is constant and inactivation is first order. In this case, Equation (44) is reduced to,

$$\frac{N}{N_0} = \exp\left(-k' t\right) \tag{45}$$

However, it is difficult to make far-reaching conclusions and compare different studies based on the Chick-Watson model, especially when the studies are conducted under dissimilar conditions.

5.2.2 Delayed Chick-Watson model

The delayed Chick-Watson model [74] is a modification in which a time lag parameter (t_{lag}) is introduced to approximate an initial lag phase in the disinfection

process (Figure 14a). For $t < t_{lag}$ the pseudo-first order loss of viability is replicated. The model may be represented as shown below,

$$\frac{N}{N_0} = \begin{Bmatrix} 1 & \text{for } t < t_{lag} \\ \exp\left(-k'\left(t - t_{lag}\right)\right. & \text{for } t > t_{lag} \end{Bmatrix} \tag{46}$$

The delayed Chick-Watson model has been used by researchers to estimate *CT* values for the photocatalytic inactivation of *E. coli* [68] and *Cryptosporidium* [30]. The hydroxyl radical was assumed to be the dominant disinfectant in these reactions.

5.2.3 Hom model

The Hom model [137] presented a generalized differential equation for the time-concentration relationships for the effect of a disinfectant on microbes. The expression is given as,

$$\frac{dN}{dt} = -kNc^d t^m \tag{47}$$

In the case where the reaction is zero-order with respect to time and disinfectant concentration, it reduces to the first-order relationship of Chick's law. Under condition where m = 0 and $d \neq 0$, it reduces to the Chick-Watson model. However, in the case where $m \neq 0$ and $n \neq 0$ and $c^d = \frac{\lambda}{t}$, then the following expression may be derived,

$$\frac{N}{N_0} = \exp\left(\frac{-k\lambda t^m}{m}\right) \tag{48}$$

The Hom model is useful for fitting disinfection curves with either an initial lag (when $m > 1$) or trailing curve (when $m < 1$). It cannot replicate both conditions simultaneously.

5.2.4 Kinetic power law models

Kinetic power law models do not make assumptions about the reaction rate order with respect to microbial concentration. The general form is

$$r = -kN^{y}c^{n} \tag{49}$$

The integration of Equation (49) gives the following for the survival ratio of organisms:

$$\frac{N}{N_0} = exp\left[\frac{-1}{y-1} ln\{1 + (y+1)kc^{n}t{N_0}^{y-1}\}\right] \tag{50}$$

Similar to the Hom model, Equation (50) can fit observed data displaying shoulders ($y < 1$) or tailing off behavior ($y > 1$).

Chang et al [138] used a kinetic power law model and reported a reaction order of $x = 1.06$ for the inactivation of *E. coli* with TiO_2. They also found that the disinfection rate was proportional to the square root of TiO_2 concentration and proportional to incident light intensity within a range of 180-1660 μE $s^{-1}m^{-2}$.

5.2.5 Probabilistic models

An alternative modeling approach to disinfection used extensively in food microbiology includes the use of probability functions to determine the distribution of inactivation times for a population of organisms exposed to a disinfectant [139]. The

approach is to consider each cell with a specific sensitivity to a certain level of disinfectant exposure. The survival S of an organism i during a certain exposure E can be described as either alive ($S = 1$) or dead ($S = 0$). This may be written as [140],

$$E < E_{c,i} \;\; S = 1 \tag{51}$$

$$E \geq E_{c,i} \;\; S = 0 \tag{52}$$

where $E_{c,i}$ is the characteristic lethal exposure dose for the particular organism. The survival of this organism is essentially a step function and can be approximated by a sigmoid decay function [140-143],

$$S_i = \frac{1}{\{1 + \exp\left[\left(E - E_{c,i}\right)/a_i\right]\}} \tag{53}$$

where a_i is the inactivation rate around the inflection point. For the total population of organisms, the survival curve is given by,

$$S(E) = \sum_{i=0}^{1} S_i(E)\Delta\phi_i \tag{54}$$

where $\Delta\phi_i$ is the fraction of the population with a critical exposure of $E_{c,i}$, such that $\sum \Delta\phi_i = 1$.

Like empirical models, probability-based models are not directly concerned with specific reaction kinetics. Instead, it is only important to define the probability distribution of the population's sensitivity to certain levels of exposure. Peleg and Shetty [140] and van Boekel [144] used the Weibull distribution function to describe microbial population sensitivity because it is a flexible function able to account for symmetric and asymmetric distributions. The Weibull probability density function is given as

$$\frac{\mathrm{d}\phi}{\mathrm{d}E_c} = b_1 b_2 {E_c}^{b_2-1} \exp\left(-b_1 {E_c}^{b_2}\right) \tag{55}$$

where $\phi(E_c)$ is the fraction of organisms having a critical exposure of E_c. Equation (55) can be algebraically transformed into the explicit function

$$E_c(\phi) = \left\{\frac{1}{b_1[-\ln(1-\phi)]}\right\}^{1/b_2} \tag{56}$$

The survival curve $S(E)$ of the entire population, is obtained by integrating the curves of all the individual organisms, that is,

$$S(E) = \int \frac{1}{\{1 + \exp[(E - E_c(\phi))/a]\}} \mathrm{d}\phi \tag{57}$$

5.3 Mechanistic models

5.3.1 Series-event model

The series event model can be represented by Equation (58). The inactivation process is modeled as a progression of discrete damage levels. The organism is assumed to be inactivated at a threshold level of damage [145, 146].

$$D_0 \overset{k_1}{\rightarrow} D_1 \overset{k_2}{\rightarrow} D_2 \overset{k_i}{\rightarrow} D_i \ldots D_{n-1} \overset{k_n}{\rightarrow} D_n \tag{58}$$

Each step is characterized by first order kinetics with respect to a constant concentration of chemical disinfectant. Each damage level D_i has a kinetic constant k_i and n is the threshold level of damage. The concentration of the disinfectant is assumed constant, so that k_i is really a pseudo-kinetic constant which can be represented by kc. The disappearance of organisms at damage level D_0 is given as,

$$\frac{dN_{D_0}}{dt} = -k_1 N_0 \tag{59}$$

and for level D_1 the expression is,

$$\frac{dN_{D_1}}{dt} = k_1 N_0 - k_2 N_{D_1} \tag{60}$$

where N_{D_0} and N_{D_1} are the concentrations of the organisms at the two damage levels respectively. The total number of surviving organisms is therefore the summation of all organisms below the threshold damage level, i.e., up to D_{n-1}.

The main limitations of this model are: (1) it requires a large number of damage levels to accurately describe inactivation, and (2) it is not flexible for analyzing disinfection data since it can only be used to analyze concave curves. In addition, it is unlikely that the underlying chemical reactions which lead to inactivation would proceed in the very same manner or would have the same effect in every cell. However, by assuming that the kinetic constant is the same at each level, the following generalized expression can be derived for the series-event model

$$\frac{N}{N_0} = exp\left\{-kt + ln\left(1 + \sum_{i=1}^{n} \frac{(kt)^i}{i!}\right)\right\} \tag{61}$$

5.3.2 Multi-target model

The multi-target model is similar to the series-event model, but instead of damage levels, it assumes each organism contains a finite number of discrete critical targets (n_c), each of which must be attacked for full inactivation of the organism. When derived for batch reactor conditions, the multi-target model takes the following form.

$$\frac{N}{N_0} = 1 - (1 - e^{-kt})^{n_c} \tag{62}$$

All the targets are assumed to be equivalent and the damage is randomly distributed among the targets. The probability of inactivating a specific target is given as $(1 - e^{-kt})$. As a target is destroyed, the probability of hitting the remaining targets is reduced.

5.3.3 Haas model

Haas [147] developed a model which was applied for the inactivation of viruses by chlorine. However, the model has general applicability. The model was formulated on chemical reaction principles and assumes the existence of an intermediary organism-disinfectant complex.

$$C + Org_{live} \overset{k_1}{\rightarrow} C\text{-}Org \overset{k_2}{\rightarrow} Org_{dead} \tag{63}$$

With a constant disinfection concentration and first order assumption with regard to cell concentration, the survival of organisms has a Monod-type expression given by,

$$\frac{N}{N_0} = exp\left\{\frac{-k_2 C\beta}{C + K_D}\left(t + \frac{\exp[-k_1 t(C + K_D)] - 1}{k_1(C + K_D)}\right)\right\} \quad (64)$$

where K_D and β are empirical constants.

5.3.4 Marugán model

A mechanistic model was presented by Marugán et al [21] to describe photocatalytic disinfection based on Langmuir-type interactions between the microbes and catalyst particles. In this model, organisms are assumed to be undamaged, damaged and inactivated. The model takes the form of two different equations which are solved numerically for the adsorption interaction, inactivation, and reaction order constants. These are given as

$$\frac{dN_{undam}}{dt} = -k\frac{K_{pseudo}N_{undam}^{y}}{1 + K_{pseudo}N_{undam}^{y} + K_{pseudo}N_{dam}^{y}} \quad (65)$$

$$\frac{dN_{dam}}{dt} = k\frac{K_{pseudo}N_{undam}^{y} - K_{pseudo}N_{dam}^{y}}{1 + K_{pseudo}N_{undam}^{y} + K_{pseudo}N_{dam}^{y}} \quad (66)$$

where N_{undam}^{η} and N_{dam}^{η} are the concentrations of undamaged and damaged cells, the sum of which gives the total cells surviving the disinfection process; K_{pseudo} and k are the pseudo Langmuir parameters for adsorption and reaction rate, respectively. The main challenge of this model is that the application of Langmuir-type interactions may not be appropriate to describe colloids, especially those as large as TiO_2 particles and microbes [148].

With the exception of the Marugán model, no other model has been developed around the mechanisms of photocatalytic disinfection. While a straightforward approach to modeling may be desirable, simplistic formulations tend to neglect many important factors that influence the process. For example, it is impossible to deduce the influence of catalyst concentration and light intensity from the foregoing models. Therefore, a comprehensive model is needed and should consider the most important mechanisms of the process. It would appear that microbe-catalyst particle interactions should be an integral part of such a model, as well as light absorption and scattering, OH radical generation, and inhibition processes.

CHAPTER 6: CONCEPTUAL MODEL FOR PHOTOCATALYSIS

6.1 Introduction

In this chapter, a theoretical model for photocatalytic disinfection is presented, taking into account the factors influencing bacterial and catalyst particle interaction. The main goal is to derive the reaction rate parameters and show how they can be measured from experiment. A quantitative analysis of colloidal adsorption and the subsequent chemical reactions of photocatalytic disinfection is important to the overall process kinetics. Previous attempts to apply models developed for molecular adsorption phenomena and reaction kinetics have proven to be inadequate, because colloidal adsorption proceeds via more complex pathways. In addition, reactions confined to the interface are influenced by the properties of the micro-environment of the double layer. As indicated in Chapter 4, double layer interactions have considerable influence on the absorption process. The adsorption of colloids is a kinetic process that involves diffusion across the double layer, charge readjustment, and ion exchange processes, each with a characteristic time constant. Due to the fundamental differences between these processes and molecular dynamics, colloidal interaction cannot always be treated with classical statistical-mechanic theories [148].

6.2 Theoretical model formulation

Consider a reaction suspension containing catalyst particles and bacterial cells. The catalyst is assumed to be Degussa P25 TiO_2 with an average particle diameter of 25 nm. On the other hand, the bacterial cells are much larger having a length of 1000 nm and diameter of 500 nm. Due to the relative size relationship, it is expected that multiple catalyst particles will adsorb to a cell. The electrostatic surface potential of the catalyst is defined by Equation (20). In like manner, the surface potential profile of the cells is defined by Equations (32) and (33). Under the pH conditions of interest (6 to 8, i.e., mostly neutral) and low electrolyte concentration, the TiO_2 surface is dominated by non-charged surface hydroxylated species, while the cell surface is mostly negative. The potential energy of interaction between the particles can be described mathematically according to Equations (34) to (40). However, it is easy to see that under the given conditions TiO_2 particles would not experience significant repulsion from the bacterial surface because the particles are close to the point of zero charge. Therefore, adsorption of TiO_2 to the bacterial cells will mostly be governed by short-range van der Waal, hydrophilic, and hydrophobic forces.

For simplicity, it is assumed that the bacterial cell can be represented as a sphere of diameter 1000 nm. Therefore, imagine a situation where the small spherical catalyst particles surround the much larger bacterial cell as shown in Figure 15. However, it should be noted that catalyst particles in suspension can agglomerate to sizes comparable with cells [149]. Since the repulsive forces are low, the catalyst particles are able to approach the cell at very close separation distances (possibly on the order of angstroms).

In some cases, specific bonding may occur with bacterial surface appendages and polymers.

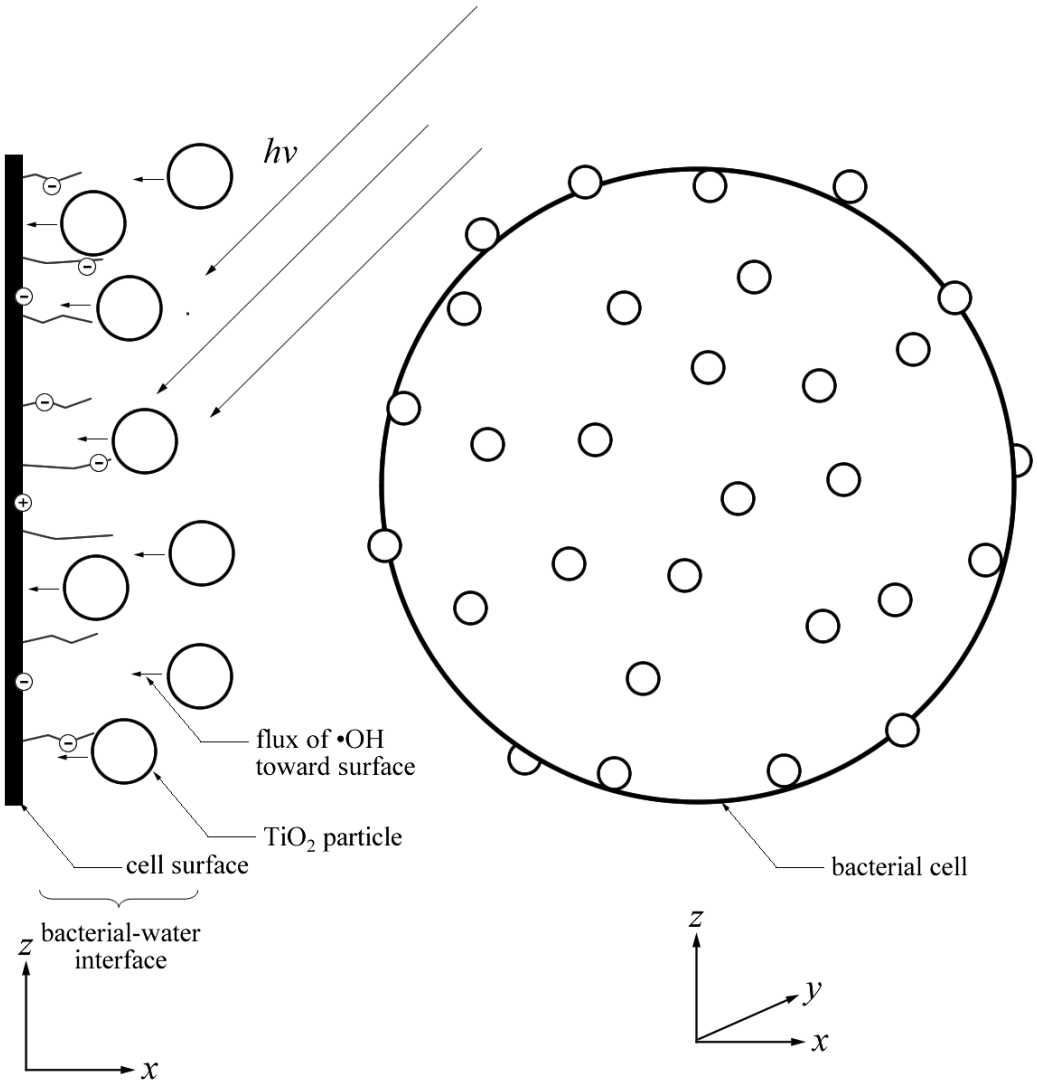

Figure 15: Surface coverage of catalyst particles on bacterial cell

Hence, with time, TiO_2 particles are immobilized at the cell surface. Under illuminated conditions, free radicals, mostly hydroxyl radicals, are formed on the surface of the TiO_2 and begin to react with bacterial surface sites. The reaction produces byproducts which diffuse away from the interface towards the bulk, but in the process they also react with radicals within the interface. With sufficient time, the cell would have experienced significant radical attack which eventually results in the inactivation of the bacterium.

6.3 Adsorption kinetics of catalysts and cells

It is important to analyze the amount of TiO_2 particles reaching the bacterial surface, since only these particles are really involved in the photocatalytic process. The analysis would also provide insight into the expected dependence of the process on catalyst concentration. The transport of catalyst particles from the bulk solution to the bacterial surface can be described by the general continuity equation,

$$\frac{\partial n_p}{\partial t} + \nabla \cdot j = s \tag{67}$$

where n_p is the number concentration of catalyst particles and, t is time, j is a vector function describing the flows (flux) of n_p, and s is the sink function describing, for example, bulk aggregation of the particles. The flux function involves particle diffusion and convection functions and may be defined as

$$j = -D \cdot \nabla n_p + U n_p \tag{68}$$

where D is the particle diffusivity tensor and U is the particle translation velocity vector. The terms described in Equations (67) and (68) can be determined by considering the specific particle-particle interactions as presented in the Chapter 4.

However, if the system shown previously in Figure 13 is considered in which catalyst particles are approaching the bacterial surface in a dilute colloidal suspension (i.e., $n \ll 10^{12}$ mL^{-1}), then the initial adsorption flux can be considered independent of the concentration of particles at the interface [148]. The particle concentration varies only along coordinate axis indicated by *X*, i.e., perpendicular to the bacterial surface. Assuming that there is no bulk aggregation of particles, Equation (67) may then be adopted in a one-dimensional form as

$$\frac{\partial n_p}{\partial t} - D_b \frac{\partial^2 n_p}{\partial x^2} + v_x(x) \frac{\partial n_p}{\partial x} = 0 \tag{69}$$

where D_b is the diffusion coefficient in the bulk and $v_x(x)$ is the fluid velocity component directly perpendicular to the interface. If it is assumed that there is a primary minimum distance x_m at the interface where particles approach and are irreversibly adsorbed [102], then the boundary condition at the bacterial interface is given as

$$n_p = 0 \; at \; x = x_m \tag{70}$$

and away from the surface

$$n_p \rightarrow n_b \tag{71}$$

where n_b is the concentration of particles away from the surface (i.e., in the bulk solution). After applying the boundary conditions, the uniform flux of particles towards the bacterial surface can be obtained as [148]

$$j_0 = \left(D_b \frac{\partial n_p}{\partial x} \right)_{x=x_m} = \frac{D_b}{x_d} n_b \tag{72}$$

where x_d is the thickness of the organism's diffusive boundary layer, which for small organisms is of a similar magnitude with the characteristic length, a_1 in this case, the organism's radius.

6.3.1 Adsorption in the absence of mechanical mixing

It is not uncommon during experiments to have a standing suspension of catalyst and bacteria in which the colloids are neutrally buoyant. The one-dimensional transport equation for the condition in which $v_x(x) = 0$ is given as [148]:

$$\frac{\partial n_p}{\partial t} - D_{rel}\frac{1}{r^2}\frac{\partial}{\partial r}\left(r^2\frac{\partial n_p}{\partial r}\right) = 0 \tag{73}$$

where $r = X + a_1 + a_2$ (see Figure 13) and $D_{rel} = D_{bac} + D_{cat}$ is the relative diffusion coefficient (D_{bac} is the diffusion coefficient of the bacteria and D_{cat} is the catalyst particle diffusion coefficient; when $a_2 \ll a_1$ the bacterial diffusion can be neglected). After applying the same boundary conditions as before, the uniform adsorption flux of particles towards the bacterial surface under these conditions is given by [148];

$$j_0(t) = \frac{D_{rel} n_b}{a_1}\left(\frac{1}{\sqrt{\pi\tau_d}} + \frac{1}{1 + a_r}\right) \tag{74}$$

where $a_r = a_2/a_1$ and the dimensionless parameter $\tau_d = t/t_r$. Here $t_r = {a_1}^2/D_{rel}$ and is time required for the catalyst particle to get across the organism's diffusive boundary layer. Therefore, the first term in the parentheses describes the transient adsorption flux which becomes negligible when $\tau_d \gg 1$ (that is, when $t \gg t_r$). It is then clear to see that a constant flux is achieved for times exceeding the relaxation time, hence

$$j_0 = \frac{D_{rel} n_b}{a_1}\left(\frac{1}{1 + a_r}\right) \tag{75}$$

The relaxation time for a catalyst particle with $D_{cat} = 10^{-12}$ m^2 s^{-1} diffusing across a layer of 500 nm thickness would be 0.25 sec which is a negligible time compared to the exposure time required for disinfection (on the order of minutes).

6.3.2 Adsorption in the presence of mechanical mixing

Mechanical mixing of the suspension introduces hydrodynamic shearing forces, which maintains suspension uniformity, but reduces mass transfer for colloids. The quantitative analysis for the effects of hydrodynamic forces can be complicated, but approximations are available for simplified scenarios, including colloids in uniform flow in the absence of electrostatic forces. The flux of spherical particles towards a spherical surface can be approximated by [148],

$$j_0 = 0.89 \frac{{D_b}^{2/3} {v_b}^{1/3}}{a_1} n_b \tag{76}$$

where v_b is the velocity of the fluid flow in the bulk phase.

6.4 Surface coverage of catalyst on bacteria

6.4.1 Surface coverage with low catalyst concentration

The dimensionless surface coverage is denoted by θ and is the ratio of the area covered by particles to the total surface area of the collector (in this case the bacterial surface). Mathematically, this may be expressed as,

$$\theta = \frac{n_s \pi {a_2}^2}{\Delta S} \tag{77}$$

where n_s is the number of particles with diameter a_2 collected on an element of area ΔS. If the elemental area is defined by vector r_s, then the rate of change of surface coverage with time is [148],

$$\frac{d\theta}{dt} = \pi {a_2}^2 n_b \bar{j}(r_s, t) \tag{78}$$

where $\bar{j}(r_s, t)$ is the normalized flux given by $j(r_s, t)/n_b$. By integrating equation (78), the expression for $\theta(t)$ is obtained as,

$$\theta(t) = \theta_t + \pi {a_2}^2 n_b \bar{j}_0(r_s)t \tag{79}$$

where θ_t is the surface concentration of particles adsorbed during the transient conditions and $\bar{j}_0$ is the normalized stationary adsorption flux previously defined. Equation (79) is only valid when the initial surface concentration is low so that already adsorbed particles do not have a significant influence (blocking) on the adsorption of new particles. This condition is true when $\theta_t \ll 1$ and can be determined from [148],

$$\theta_t = \pi {a_2}^2 n_b \bar{j}_0 \tau_d \tag{80}$$

For a suspension of spheres not subject to mechanical agitation, θ_t can be approximated as,

$$\theta_t = \pi {a_2}^2 a_1 n_b \tag{81}$$

Similarly, for spherical particles in a uniform flow,

$$\theta_t = 0.55\pi {a_2}^2 {a_1}^{2/3} n_b {v_x}^{-1/3} {D_b}^{1/3} \tag{82}$$

6.4.2 Surface coverage with high catalyst concentrations

The kinetics of adsorption differs for systems with high colloid concentrations [148, 150]. Catalyst particles already adsorbed at the surface of the bacteria essentially preclude or block other particles from adsorbing within an exclusion zone. Therefore, the

time evolution of the surface coverage is affected by existing coverage. A number of other models can be employed to model these systems (see, for example, reference [148]). One of the simplest, but powerful approach is the random sequential adsorption (RSA) model [151]. In an RSA simulation, particles are randomly placed at the surface at a constant rate. Once the particle is placed, it is permanently affixed to the surface. Particles are not allowed to overlap, so a surface saturation is eventually reached when there are no more available spaces to fit particles. With this model, the surface is never completely covered. Even though spaces remain, they are not large enough to allow the positioning of other particles. Hence, the saturation level is commonly referred to as the "jamming" limit and has a value of 54.7% for monodispersed spheres when only steric effects are considered [151]. RSA models have been developed to incorporate short-range interactions between particles [150]. Even though these assumptions are straightforward, the RSA configuration for high surface concentration, especially in three dimensions can usually only be predicted by numerical simulation [150, 152].

However, the kinetic curves describing the dependence of surface coverage θ on the adsorption time have been extensively calculated for hard and soft spheres by other authors under many different scenarios including no mixing conditions, electrostatic interactions, and hydrodynamic flows [148, 152, 153]. Adamczyk et al [148] provide approximations which can be used in place of complex numerical simulations. The RSA derived expression for the time evolution of surface coverage can be approximated by,

$$\theta(\tau) = \frac{\theta_\infty}{(1+\mathrm{H}^*)^2}\left[1 - 0.432\left(\frac{1}{\sqrt{\pi {a_2}^2 \mathrm{j_0 n_b t}}}\right)\right] \tag{83}$$

where H^* is a dimensionless parameter that defines the effective interaction range and depends on the energy of interaction and the double layer thickness as indicated by κa^{-1}. H* may be approximated from,

$$H^* = L_e \ln\xi - L_e \ln\left(1 + \frac{1}{2} L_e \ln\xi\right) \tag{84}$$

where L_e is the dimensionless double layer thickness give by κa^{-1} and ξ is the dimensionless interaction energy [148].

For colloidal particles affected by hydrodynamic shear forces, the surface coverage can be approximated by,

$$\theta(t) = \frac{1}{\theta_h}\left[1 - \exp\left(-\frac{\theta}{\theta_h}\tau\right)\right] \tag{85}$$

where θ_h is given as

$$\theta_h = \frac{1}{[4(1 + H^*)^2 + C_h \bar{G}]} \tag{86}$$

and

$$\bar{G} = \frac{G {a_2}^2}{D_b} \gg 1 \tag{87}$$

where G is the shear rate at a given point on the interface and C_h is a dimensionless fitting parameters which must be determined by simulations.

6.5 Kinetics of hydroxyl radicals at interface

6.5.1 Generation rate

During the illumination of TiO_2 particles hydroxyl radicals are produced at the catalyst-water interface according to equations (3) and (5). The generation of the radicals is central to the overall photocatalytic process. At steady state conditions, it is the difference between the rate of light absorption and the recombination rate. As can be imagined, the latter process would be nearly impractical to measure in a real system. The rate of light absorption is more amenable to experimentation, but intense light scattering effects still makes this a difficult task. However, the incident photon flux I_0 in a solution can be determined by use of actinometry [154-157], and the absorbed flux I_a can be estimated for a sample by determining its integrated absorption fraction F_s from spectrophotometric methods. Hence,

$$I_a = I_0 F_s \tag{88}$$

F_s has been previously determined for a range of TiO_2 concentrations [158]. The chart in Figure 16 has been reconstructed based on interpolation and extrapolation of the literature data. Once the rate of adsorbed photon flux is determined, the rate of OH radical generation can be estimated by [159],

$$G_{\cdot OH} = I_a \varphi_{\cdot OH} \tag{89}$$

where $\varphi_{\cdot OH}$ is the quantum yield of radical generation. The rate of generation of OH radicals and quantum yields for TiO_2 in chemical photocatalytic reaction systems were determined by Sun and Bolton [158] according to the method described above. The radical generation rate is a function of catalyst concentration, the physical and chemical

properties of the catalyst, light intensity, and dissolved oxygen concentration. Also important to note is that the addition of hydrogen peroxide has a positive effect on the generation rate [63, 158, 160-162].

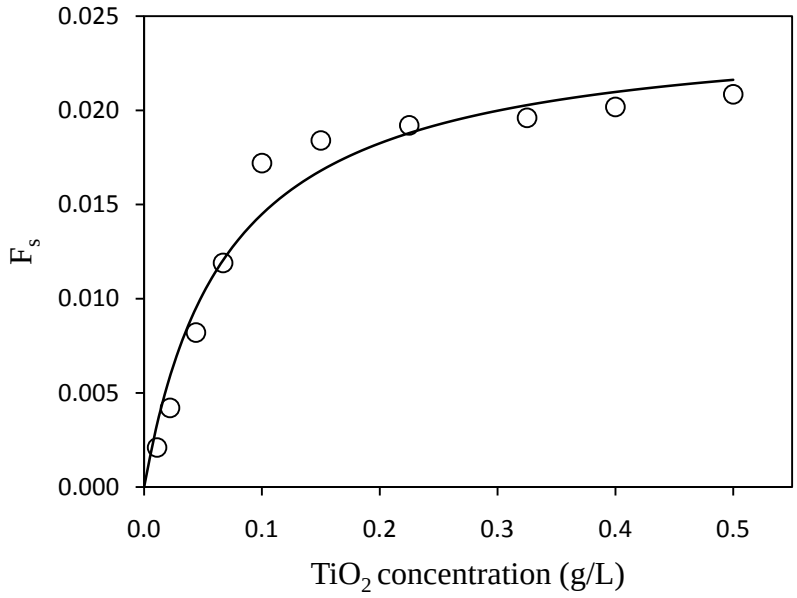

Figure 16: Plot of integrated absorption fraction F_s for TiO_2 concentration

6.5.2 Nature of OH radicals at the bacterial membrane

In general, there are two theories concerning the nature of radicals at the catalyst surface; (1) radicals remain surface-bound to the catalyst during reaction with adsorbed species [19, 48, 64]; and (2) radicals diffuse away from the surface to react with compounds in solution or on the catalyst surface [64, 163-165]. It would be very difficult to distinguish between these two possibilities in the overall kinetics of the process. However, in the latter case, it is recognized that hydroxyl radicals, in particular, are diffusion limited owing to their high reactivity. Depending on the concentration of oxidizable species, hydroxyl radicals have been found to diffuse up to a distance of 10

nm away from the site of generation [166, 167]. Therefore, it is possible that radicals can diffuse into a bacterial membrane during very close approach with a catalyst surface. The diffusion coefficient of hydroxyl radicals in water has been estimated to be on the order of 10^{-9} m^2s^{-1} at 25°C [168-170]. If the nearest substrate is 10-100 nm away from the site of generation, it would take a radical much less than a fraction of a second to move across this range of distance. However, a number of factors may hinder diffusion near the vicinity of the cell membrane, including electrolyte ions, hydrophobic zones, and the solvation shell around the radical [168, 171, 172].

6.6 Microbial survival

The model presented by Haas [147] may be adopted for the reaction of hydroxyl radicals with cells in a simple bimolecular reaction,

$$m[\cdot\mathrm{OH}] + [\mathrm{cell}]_l \xrightarrow{k_{dis}} [\mathrm{cell}]_d + m\mathrm{OH}^- \tag{90}$$

where the subscripts l and d denote live and dead cells respectively, and k_{dis} is the observed rate constant for disinfection. The overall disinfection reaction rate for this bimolecular reaction is given as

$$R_d = -k_{dis}[\cdot\mathrm{OH}]^n[\mathrm{cell}]_l{}^y \tag{91}$$

where n and y are the reaction orders related to radicals and cells respectively. The concentration units for hydroxyl radicals are moles per liter, but for the cell they are given as cell number density (cells per liter). The observed disinfection rate k_{dis} has contributions from (1) the diffusion-controlled rate constant k_d at which the cell-radical complex $[\mathrm{cell}\cdot\mathrm{OH}]_d$ is formed,

$$m[\cdot\mathrm{OH}] + [\mathrm{cell}]_l \underset{k'_d}{\overset{k_d}{\rightleftharpoons}} [\mathrm{cell}\cdot(\mathrm{OH})_\mathrm{m}]_d \tag{92}$$

(2) the rate constant for dissociation (or radical quenching and repair) $k_{d'}$, and (3) the rate constant k_{inv} at which the cell is eventually inactivated after being exposed to the radical.

$$[\mathrm{cell}\cdot(\mathrm{OH})_\mathrm{m}] \xrightarrow{k_{inv}} [\mathrm{cell}]_d + m\mathrm{OH}^- \tag{93}$$

It can be shown that the observed disinfection rate has the form

$$k_{dis} = \frac{k_d k_{inv}}{k_{inv} + k'_d} \tag{94}$$

If the inactivation rate constant is much faster than the repair/radical quenching, that is, $k_{inv} \gg k'_d$, then as radicals encounter the cell, it is rapidly inactivated without time for repair or quenching. In this case, the observed rate is equal to the diffusion rate constant ($k_{dis} = k_d$) and the reaction depends on how fast radicals can encounter the cells. However, if the inactivation rate is much slower than the repair and quenching mechanisms, then the observed rate is given by

$$k_{dis} = \frac{k_d}{k'_d} k_{inv} = K_{[\mathrm{cell}\cdot(\mathrm{OH})_\mathrm{m}]} k_{inv} \tag{95}$$

where $K_{[\mathrm{cell}\cdot(\mathrm{OH})_\mathrm{m}]}$ is the equilibrium constant for the formation of the cell-radical complex.

6.7 Kinetics of byproduct evolution

The effect of free radicals on cellular molecules has long been reported (see for example [173, 174]). In particular, the hydroxyl radical is very reactive and is capable of injuring virtually all biological macromolecules. Free radicals associated with the

photocatalytic process can react with macromolecules on the bacterial surface, including proteins, polysaccharides, and lipids. Of these, lipids are known to be the most prone to oxidative damage, particularly lipids with unsaturated fatty acids. Proteins are also very susceptible to radical oxidation. The extent of the damage to particular targets depends on a number of factors, including the concentration of the target, the reaction rate constants, the relative locations of the target and oxidant, the occurrence of secondary damaging events, occurrence of transfer reactions, and repair and scavenging reactions [175-177]. In addition, the oxidation of intracellular constituents can occur through the generation of secondary oxidants, such as lipid radicals, hydrogen peroxide and superoxide [178-180]. Superoxide and hydrogen peroxide can also produce hydroxyl radicals in the intracellular environment through the Fenton reaction involving “free” iron [181, 182].

For *E. coli*, most of the outer membrane is made up of phospholipids. In addition to their abundance, their ease of oxidizability makes this group of biomolecules prime targets for hydroxyl radical attack. Lipid peroxidation has been identified as a leading reaction mechanism during photocatalysis [20, 178, 183-185]. The peroxidation of lipids involves three distinct steps: initiation, propagation and termination. Figure 17 illustrates these processes schematically. The initiation reaction occurs when ·OH abstracts an H atom from the unsaturated fatty acid, forming a carbon-centered radical. In the propagation reactions, the carbon-centered radical reacts with oxygen and yields a peroxyl radical. The peroxyl radical then abstracts an H atom from a second fatty acid forming a lipid hydroperoxide (LOOH) and leaving another carbon-centered free radical [173, 174]. The lipid hydroperoxide eventually degrades into malondialdehyde (MDA)

and other unsaturated aldehydes. Termination occurs when two radicals react together forming neutral products (Figure 17). The peroxidation of lipids can often result in damage to biomolecules at sites considerably distant from where the initial free radical reaction occurred [186]. Lipid peroxidation can be monitored by assessing the rate of oxygen uptake or the production of byproducts including MDA and lipid hydroperoxides [187, 188].

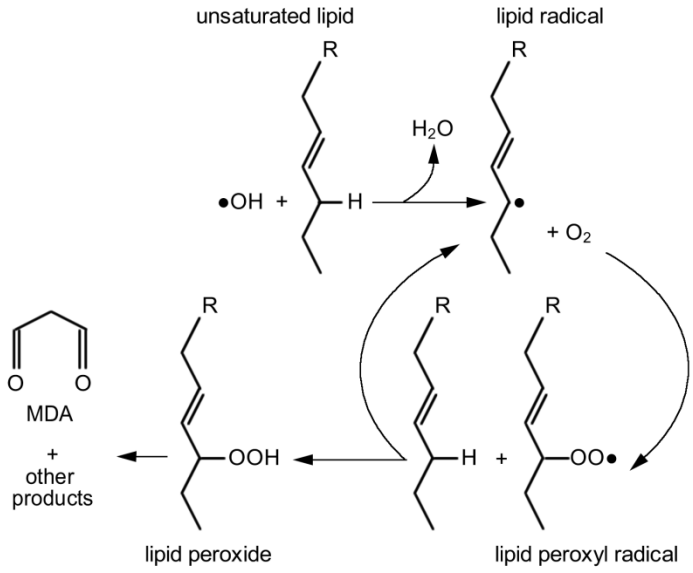

Figure 17: Schematic of lipid peroxidation

Most of the byproducts are formed within the interface where the hydroxyl radicals react with the cell surface. Since byproducts can be considered molecular fragments of disinfection, they diffuse throughout the solution and absorb to the catalyst surface. For simplicity, it is assumed that adsorption kinetics can be described by the Langmuir model. Hence, in the absence of other adsorbing molecules the rate of byproduct oxidation is given as

$$R_{BP} = -k_{BP} \frac{K_{BP}^{ads} C_{BP}}{1 + K_{BP}^{ads} C_{BP}} \quad (96)$$

where $-k_{BP}$ is the reaction rate constant, K_{BP}^{ads} is the Langmuir adsorption rate constant, and C_{BP} the concentration of all byproducts. The OH radical is known to react very efficiently with biomolecules at a diffusion-controlled rate with a reaction rate constant on the order of 10^9 M^{-1} s^{-1} in homogeneous solutions [189-191].

6.8 Adsorption and inhibition kinetics of inorganic ions

Inorganic electrolyte ions, particularly anions such as chloride (Cl^-), sulfate (SO_4^{2-}), phosphate (HPO_4^{2-}), bicarbonate (HCO_3^-), and nitrate (NO_3^-), are known to adsorb to the surface of TiO_2 [100, 101] and inhibit the photocatalytic process [192-196]. However, there has never been any model to quantify the effect of these ions on photocatalytic disinfection efficiency. To include these effects in the current model, the formation of surface complexes is analyzed. The adsorption of inorganic ions to the surface of TiO_2 can be described in terms of ligand exchange reactions with surface hydroxyl groups. This process is similar to complex formation in homogeneous solution, but the apparent equilibrium constants are adjusted to account for the electrostatic effects of the double layer [197]. The adsorption kinetics is governed by the properties of the adsorbing ion and the properties of the surface. The primary parameters for a quantitative description of ion adsorption are the acidity constants (K_a) of the ionic species and the surface hydroxyl groups, and the constants for the formation of the complexes (K_A^s). With these constants the surface speciation can be computed as a function of pH and concentration of ionic species.

However, for a given pH and low surface coverage, anion adsorption on metal oxide surfaces can be described by the Langmuir equation [101, 198],

$$K_{An}^{s} = \frac{[\text{Ti-An}]}{[\text{Ti-OH}][\text{C}_{\text{An}}][\text{H}^{+}]} \tag{97}$$

where [Ti-An] is the concentration of an adsorbed anion, $[\text{Ti-OH}]$ is the activity of all protonated surface moieties that can be displaced by the anion, and $[\text{C}_{\text{An}}]$ is the concentration of the anion in solution. Constants for the formation of complexes by common anions on the surface of TiO_2 have been reported in the literature [50, 197, 199] and are given in Table 2. In the absence of other absorbing molecules, Equation (97) can be rearranged to give the Langmuir equation.

$$\theta_{An,i} = \frac{K_{An,i}C_{An,i}[\text{H}^{+}]}{1 + \sum_{i=1}^{N} K_{An,i}C_{An,i}[\text{H}^{+}]} \tag{98}$$

where $\theta_{An,i}$ is the surface coverage of the *i*-th anion species, $C_{An,i}$ is the concentration of the specific anion species in solution.

Table 2: Adsorption equilibrium constants for some common anions on the surface of TiO_2

Anion	Equilibrium constant M^{-1}
Cl^{-}	1×10^{5} [197]
CO_3^{2-}	6×10^{4} [200]
SO_4^{2-}	2×10^{8} [201]
$H_2PO_4^{-}$	8×10^{6} [202]

In homogenous solutions inorganic ions react with hydroxyl radicals at diffusion-controlled rates. The rate constants and mechanisms for these interactions have been reported [203, 204]. However, since the rate of generation (and by extension, the concentration) of hydroxyl radicals in TiO_2 suspensions is significantly lower than the homogeneous diffusion-controlled rates, the overall reaction between the ions and the radicals is likely to be limited by the generation rate of radicals. The concentration of radicals during photocatalysis ($\ll 1\times10^{-8}$M) is usually much lower than the electrolyte concentration [205]. If it assumed that the generation of radicals is uniformed across the entire catalyst surface, then the rate of the inhibition reactions is directly proportional to the extent of coverage. The latter may be determined from the specific adsorption isotherms of the various ions in solution [194, 195]. Therefore, it is only important to determine the surface coverage of ions to understand the extent of inhibition on the disinfection process.

Guillard et al [195] found that electrolyte ions form a salt layer at the surface of TiO_2 which prevented the adsorption of organic substrate. In the same way, inorganic ions, due to their molecular size, can approach the catalyst surface and specifically adsorb in a much more efficient way than large micron-sized bacterial cells. However, at low salt concentration there is low screening of the cells and there are enough available hydroxyl sites to generate radicals. Under these conditions, the efficiency of disinfection is optimal. Conversely, at higher concentrations the opposite is true, that is, most of the radicals are consumed by inorganic ions and the cells are screened to a larger extent. Therefore, it can be argued that disinfection must occur as a result of the residual

hydroxyl radicals, which are able to escape the catalyst surface or interact directly through surface-to-surface contact. The residual hydroxyl radical generation is the difference between the photo-generation rate of radicals and the rate of inhibition. As before in the absence of other absorbing molecules, the rate of inhibition or radical quenching can be expressed as a factor of the ·OH generation rate $G_{\cdot OH}$ as

$$R_{q,i} = -\theta_T \times G_{\cdot OH} = \sum_{i=1}^{N} \frac{K_{An,i} C_{An,i}[H^+]}{1 + \sum_{i=1}^{N} K_{An,i} C_{An,i}[H^+]} G_{\cdot OH} \quad (99)$$

As $C \to \infty,\ \theta_T \to 1$, all active sites for hydroxyl radical generation are blocked, then the rate of disinfection is at its lowest. θ_T is the total surface coverage found by summing the individual coverage of all ionic species.

6.9 Model for overall inactivation kinetics

Now that the important mechanisms for the photocatalytic disinfection process have been defined, the kinetics for the overall process may be determined by performing mass balances for specific variables. This analysis

6.9.1 Mass balance of live cells

The survival of cells is given by Equation (91). The differential form of the equation can be written as

$$\frac{d[cell]_l}{dt} = -k_{dis}[\cdot OH]^n [cell]_l{}^y \quad (100)$$

The disinfection reaction is peculiar in that it involves the reaction of molecules (usually given in mol L^{-1}) and cells (given in CFU L^{-1}). Therefore, it is important to recognize that Equation (91) can be expressed in two ways with respect to the reactants; (1) the rate of

disinfection (CFU L^{-1} s^{-1}) as given in Equation (100), where the units of the disinfection rate constant k_{dis} are M^{-n} s^{-1}, and (2) the rate of consumption of hydroxyl radicals given in concentration per time (M s^{-1}). To reconcile this irregularity, Equation (100) can also be expressed in terms of radical consumption,

$$\frac{\mathrm{d}[\cdot\mathrm{OH}]}{\mathrm{dt}} = -k_{.\mathrm{OH}}[\cdot\mathrm{OH}]^{n}[\mathrm{cell}]_{l}^{y} \tag{101}$$

where $k_{.\mathrm{OH}}$ is the reaction rate constant given in units of L^{n} M^{n-1} CFU^{-1} s^{-1}.

6.9.2 Mass balance of byproducts

In order to account for the accumulation of byproduct, Equation (92) is rewritten as

$$m[\cdot\mathrm{OH}] + [\mathrm{cell}]_{l} \rightarrow [\mathrm{cell}]_{d} + \gamma[\mathrm{BP}] \tag{102}$$

One of the inherent difficulties of Equation (102) is that one radical can set off a chain of reactions resulting in numerous byproducts being formed. However, if it is assumed that most of the byproducts result from oxidation of lipids, then the reaction kinetics in the membrane would be very similar to OH radicals reacting with lipids in solution (i.e., outside of a bilayer formation) [206-209]. Therefore, if $\gamma = m$ the accumulation of by products is given by

$$\frac{\mathrm{d}C_{BP}}{\mathrm{dt}} = k_{.\mathrm{OH}}[\cdot\mathrm{OH}]^{x}[\mathrm{cell}]_{l}^{y} - G_{.\mathrm{OH}}\frac{K_{BP}^{ads}C_{BP}}{1 + K_{BP}^{ads}C_{BP} + \sum_{i=1}^{N}K_{An,i}C_{An,i}[\mathrm{H}^{+}]} \tag{103}$$

6.9.3 Mass balance of OH radicals

The mass balance for OH radicals in the interface between a catalyst and the cell surface is given as

$$\frac{\mathrm{d}[\cdot\mathrm{OH}]}{\mathrm{dt}} = \mathrm{G}_{\cdot\mathrm{OH}}(1 - \theta_{An} - \theta_{BP}) \; - k_{\cdot\mathrm{OH}}[\cdot\mathrm{OH}]^{x}[\mathrm{cell}]_{l}{}^{y} \tag{104}$$

where $\theta_{An}$and θ_{BP} are the surface coverage of anions and byproducts, respectively. It is customary for researchers to assume that the concentration of OH radicals is constant during the reaction. However, that assumption is not applied here. Together, Equations (100) through (104) represent the overall kinetics of the photocatalytic disinfection process.

CHAPTER 7: EXPERIMENTAL DESIGN AND PROTOCOLS

7.1 Selection of experimental factors

The rate of inactivation of a target organism is the most important design variable for disinfection systems. For photocatalysis, the rate of disinfection depends on the synergistic effect of catalyst concentration and light intensity, which directly influences the rate of generation of OH radicals in the reactor. If the concentration of radicals can be significantly increased, it is clear to see that the disinfection rate would also increase. This effect has previously been observed when hydrogen peroxide was added to disinfection experiments with *E. coli* [160], and also in chemical photocatalysis studies [63, 161]. Likewise, sink terms such as byproducts or compounds that exert a demand on the OH radicals reduce the overall rate of the reaction [160]. The concentration of solution electrolytes (ionic strength) has also been studied and the effects can be explained based on the principles laid out in Chapters 4 and 6.

Based on the analysis in the previous chapters, the most important operational variables to be tested were catalyst concentration and light intensity. The synergistic effect of these two factors will determine the most efficient combination of contact time and dose to employ. Light intensity was tested at 3 levels; high, medium, and low. Each level corresponded to a specific light intensity value measured in Einstein per volume per time (E L^{-1} s^{-1}). Catalyst concentration was tested across 4 levels; 0.01, 0.10, 0.25, and 0.50 g L^{-1}.

In an attempt to account for biological variation in the model, one additional factor, fatty acid composition, was also selected. As previously discussed, unsaturated fatty acids have been identified as a major target during photocatalytic disinfection. By modifying the content of specific unsaturated fatty acids in the organism's membrane, the effect of this variable could be investigated. A factorial experimental design was employed to study the effect of the three independent variables on the disinfection rate and dose-responsive behavior of the organism during photocatalysis. Experiments were conducted in triplicates.

In addition to the response of microbial survival to various treatments, the evolution of byproducts was also monitored for a subset of experiments. MDA is a common biomarker for lipid peroxidation and was used in this study to evaluate the kinetics of byproduct formation [187, 210, 211]. Lipid hydroperoxides were also tested in some experiments. Both of these compounds are well known byproducts from membrane peroxidation resulting from a reaction with hydroxyl radicals [211-214]. The choice to focus on membrane fatty acids and the kinetics of byproduct evolution was validated by using model cellular membranes (liposomes) made from representative fractions of natural *E. coli* fatty acids.

7.2 Method of data analysis

7.2.1 Statistical analysis

To test for differences among groups, a one-way ANOVA was performed on survival data from 144 experiments, which included all factors at all levels. The null

hypothesis for this test was that there were no differences among the groups. The Tukey test was used to compare groups and examine interaction effects of the factors. Different levels of interaction were examined including main effects, and 2-way and 3-way interactions.

7.2.2 Numerical analysis

Equations (100), (103), and (104) were solved numerically by a Runge-Kutta method in a MatLab algorithm and constrained to fit the survival data from the 144 experiments using a non-linear least squares method (See Appendix A). From this procedure values for the disinfection rate constant and reaction order were obtained.

7.3 Microbiological methods

7.3.1 Preparation of *E. coli* culture

Pure cultures of *E. coli* (ATCC 25922) were grown aerobically in 100 mL of Luria broth at 37°C on an incubator shaker (250 rpm). The growth kinetics of the organism was determined from experiment by monitoring the turbidity of the suspension with time (Figure 18). The turbidity was measured at 550 nm with a DR/2000 spectrophotometer (HACH Company).

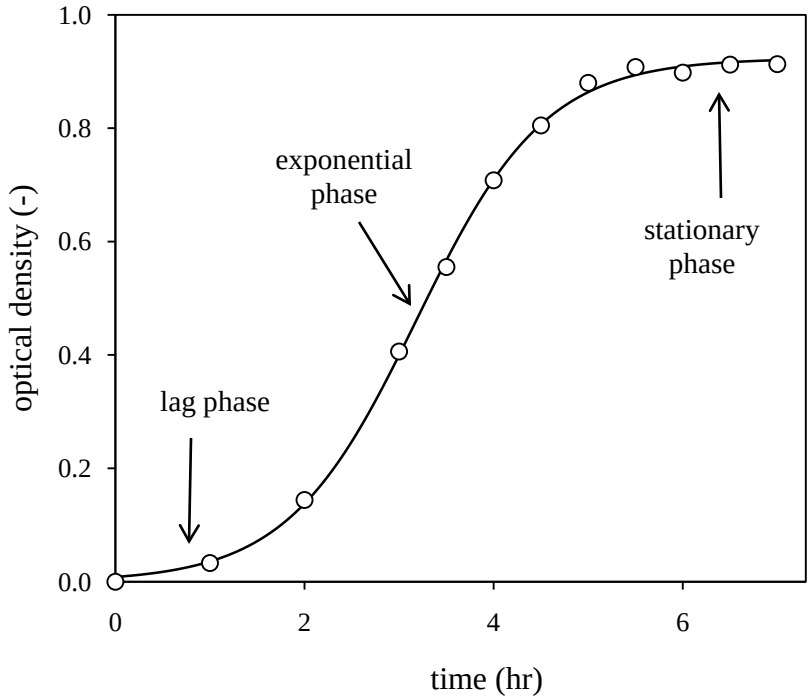

Figure 18: *E. coli* growth curve fitted with a continuous logistic function

7.3.2 Cell harvesting and enumeration

Bacteria are known to modify their fatty acid content depending on the growth phase [105, 215-217]. Therefore, it was important to select a standard time during growth to harvest the organisms since fatty acid content was an independent variable in the experiments. *E. coli* cells were always harvested after 6 hours of growth from an actively growing media broth by centrifugation at 1380 × *g* for 10 min in a 15-mL tube. The cell pellet was washed and re-suspended in sterile deionized water (resistivity >16 Mohm-cm). This process was performed twice to ensure that most of the broth solution was removed. The turbidity of the suspension was determined as described before using visible light spectrophotometry. A standard curve was developed to correlate turbidity readings with cell density (CFU m L^{-1}) by performing serial dilutions to obtain between 30 and 300 CFU in 100 μL on TSA plates. The plates were incubated at 37ºC and the

viable cells which appeared after 24 hours were manually counted. The cell suspension was diluted to the required final concentration for all experiments.

7.3.3 Preparation and storage of growth media

Luria broth was obtained from US Biological (Swampscott, MA) as a dry powder and prepared according to the manufacturer's instructions. The powder (7.75 g) was added in 450 mL of deionized water while being heated and gently stirred until it was completely dissolved. The pH of the media was adjusted to 7.0 with 1 N NaOH, brought to 500 mL, and finally autoclaved for 15 minutes at 121ºC and 15 psi. The solution was cooled to room temperature before use and the remainder stored at 4ºC in the refrigerator. Liquid media was used within 14 days.

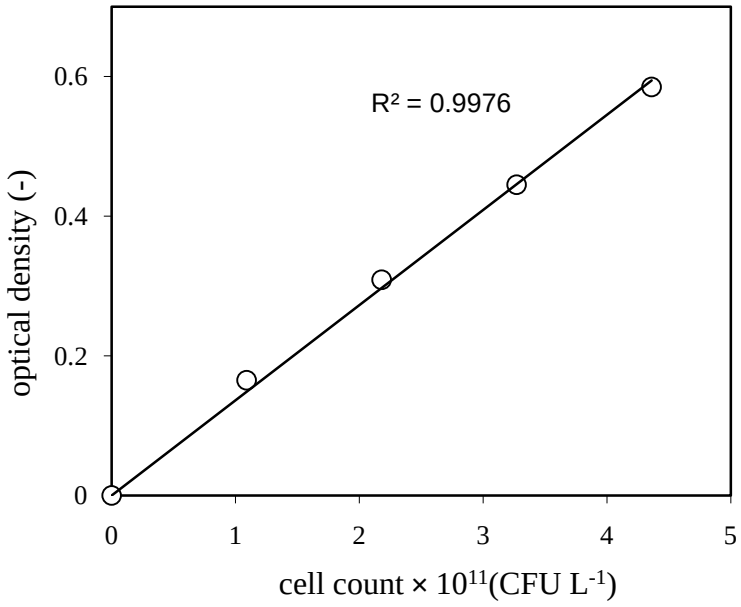

Figure 19: Standard plot for the correlation of cell density and optical density

7.3.4 Preparation and storage of agar plates

Tryptic soy agar was obtained from MP Biomedicals (Solon, OH) as a dry powder and prepared according to the manufacturer's instructions. The media was prepared with 40 g of dry powder to 1 L of deionized water. The solution was stirred and heated until it boiled, and then sterilized for 15 minutes at 121ºC and 15 psi in an autoclave. Sterile media was chilled to 55ºC before pouring into 100-mm × 15-mm sterile polystyrene Petri plates. Agar plates not used immediately were stored at 4ºC in a refrigerator and used within 7 days.

7.4 Photocatalytic experiments

7.4.1 Reactor design and setup

Experiments were conducted in 30-mL borosilicate test tubes (15.35 mm diameter) which were placed in the center of a reactor holder surrounded by lamps (Figure 20). The coefficient of transparency for a 10-mm thick borosilicate glass is within the range of 0.95-0.99 for wavelengths from 360-500 nm [218]. This provided a suitable economic alternative to the commonly used, but expensive quartz vessels. The reactor holder was fabricated with different slots for the lamps. This was done so that the light intensity could be varied by adjusting the distance of the lamps to the reactor vessel. Two lamps were always used and kept equidistant to the reactor. Three positions were used to achieve the range of high to low intensity. Lamps were turned on at least 15 minutes prior to experiments to allow them to warm up for stable output. The entire unit shown in Figure 20 was placed centered on a magnetic stir plate to continuously stir the solution with a mini-stir bar (12.7 cm long × 0.64 cm dia.)

7.4.2 Catalyst stock solution preparation and storage

Degussa P25 TiO_2 was used as the catalyst for all photocatalytic experiments. The formulation of this catalyst has been published extensively as containing 75% anatase and 25% rutile with an average surface area of 50 $m^2 g^{-1}$ (see for example [51, 219-221]). A stock solution of 10 g L^{-1} was prepared by vigorously mixing the white-powdered catalyst with deionized water, autoclaving and storing the suspension at room temperature in a sealed container.

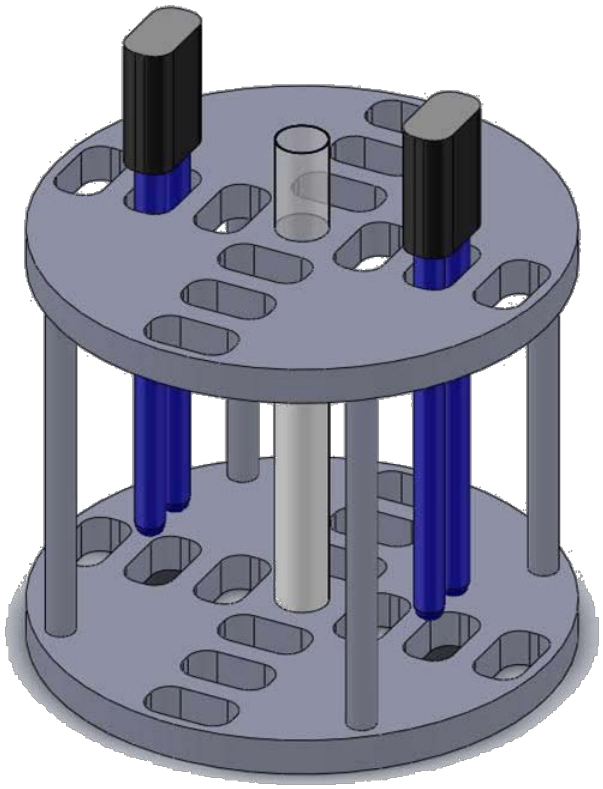

Figure 20: Reactor apparatus

7.4.3 Light source

Light for the photocatalytic experiments was provided by 9-W UVA lamps (model PL9W/08) from the Phillips Lighting company (Figure 21). They have overall dimensions of 167 mm × 28 mm. The lamps have a spectral maximum of 365 nm (Figure 22) and the UVA radiation output is 1.7 W.

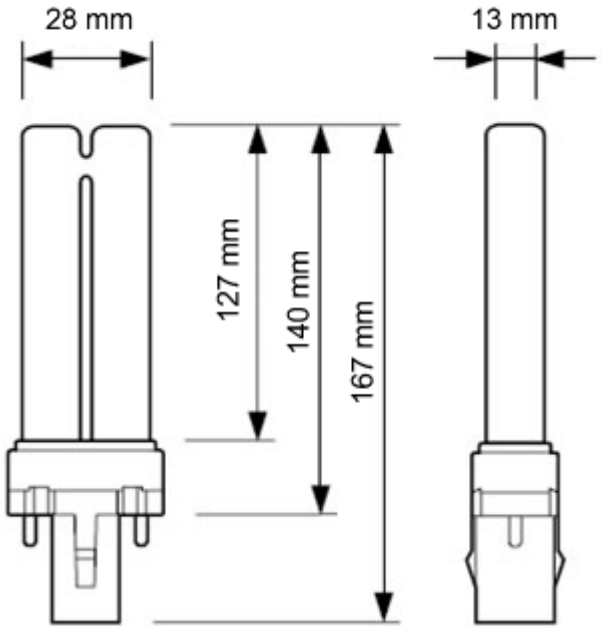

Figure 21: Schematic of UVA fluorescent lamp used in experiments

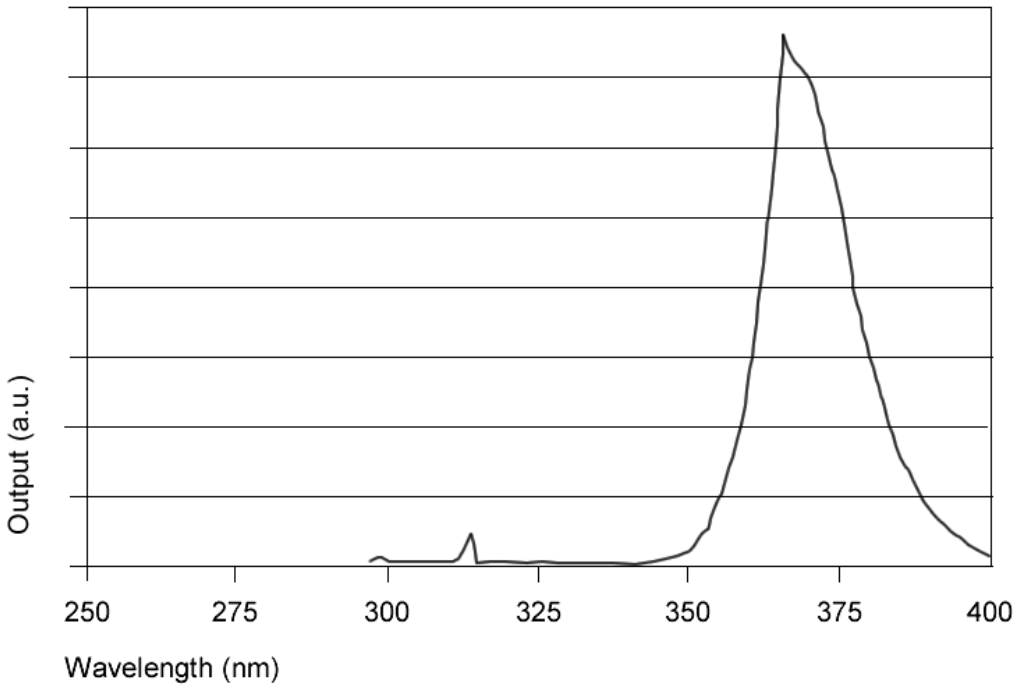

Figure 22: Spectral power distribution of PL-S 9W/08 lamp (source: manufacturer)

7.4.4 Light intensity measurements

Since there were two reactors, light intensity measurements were done for two pairs of lamps at three different positions on the reactor holder. The lamps were numbered 1-4 and the positions were numbered 1-3 from the closest to the farthest (Figure 23). The incident light intensity in the reactor solution was determined by azoxybenzene actinometry [157]. The quantum yield Φ for azoxybenzene is about 0.02 across the UV region 200-380 nm and is unreactive in the visible range. Azoxybenzene has a sharp absorption cut-off near 380 nm and this, combined with the low quantum yield, means that solutions of azoxybenzene are conveniently handled under ambient light.

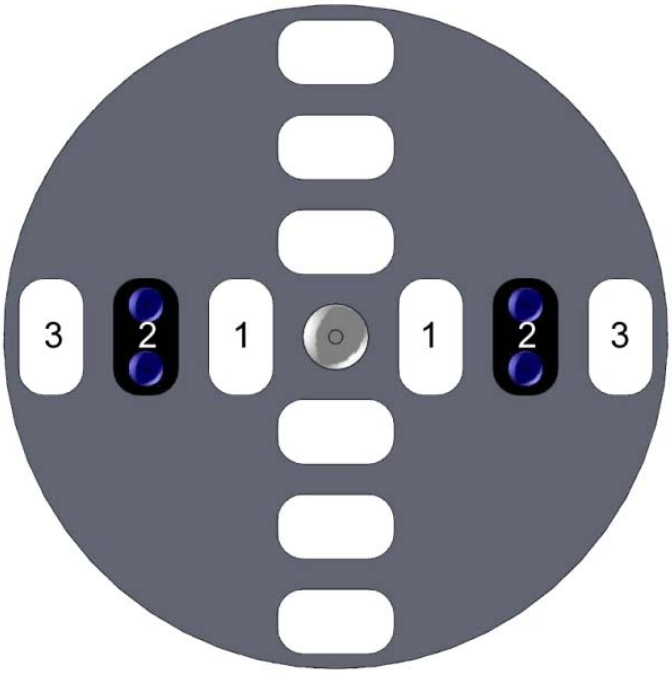

Figure 23: Lamp locations on reactor

The procedure included irradiating 20 mL of 4.89 mM azoxybenzene solution in ethanol in the same borosilicate reactor vessel used for photocatalytic disinfection experiments. During irradiation, 2-mL aliquots were sampled at one-minute intervals for 5 minutes. Two drops of potassium hydroxide solution in ethanol (0.10 N) were added to convert the photoproduct (hydroxyazobenzene) to its anion form. The samples were analyzed for visible light absorption at 458 nm (ε = 7600). The relationship between photon dose and concentration is given as

$$A_0 \ln\left(1 - \frac{P}{A_0}\right) = -\Phi_r I_0 t \tag{105}$$

where A_0 is the initial concentration of azoxybenzene (mol L^{-1}), P is the concentration of the photoproduct (mol L^{-1}) at time t, and I_0 is the incident light intensity (E $L^{-1}s^{-1}$). The slope of the plot $\ln\left(1-\frac{P}{A_0}\right)$ versus t was used to determine I_0 (Figure 24).

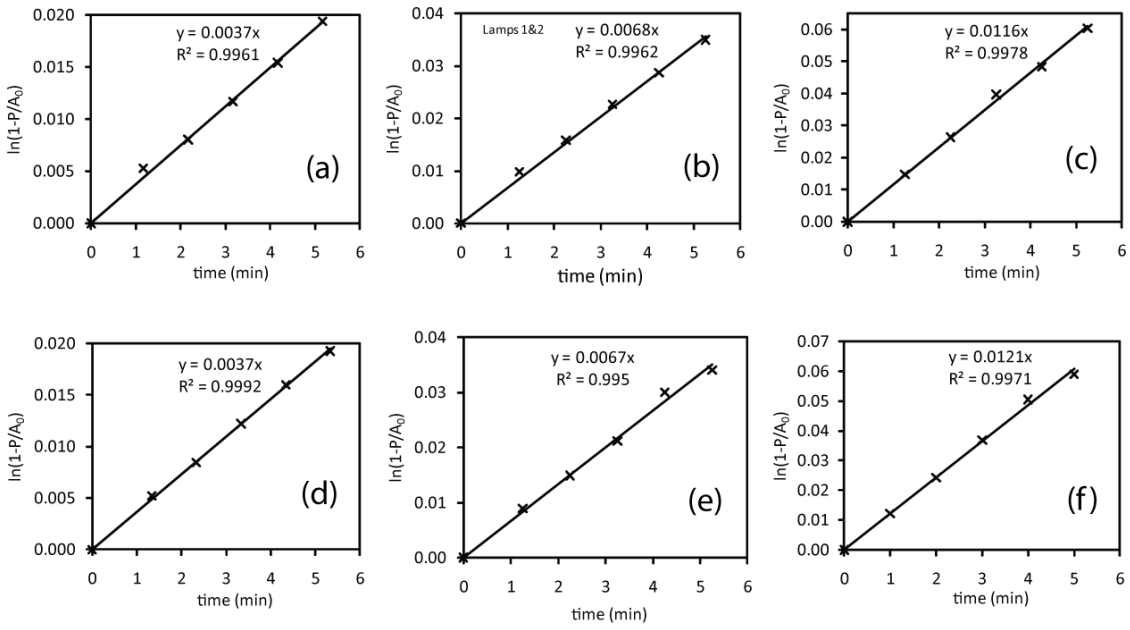

Figure 24: Typical plots used to determine incident light intensity by actinometry for pair-wise combination of lamps 1 and 2 [(a)-(c)], and 3 and 4 [(d)-(f)]

The measurements were conducted periodically over the course of the study. The incident intensity for the pairs of lamps is given in Table 3.

7.4.5 Preparation of working reaction solutions

All liquids and vessels, including PBS solution, deionized water, reaction tube, and stir bar were autoclaved for 15 minutes at 121ºC and 15 psi prior to being used in experiments. The reaction pH was monitored over a series of preliminary experiments and found to be stable during the course of the experiments. Therefore, only initial pH

was recorded for final experiments. Three sets of control experiments were conducted; (1) solution of catalyst and microbes with no light (dark experiments); (2) irradiated solutions of microbes with no catalyst present (irradiated blank); and (3) non-irradiated solution of microbes only (organism control). The final composition of the reaction solution was made up by adding the appropriate volumes of stock solutions together and then pouring the mixture into the reaction vessel (Table 4). The final composition of electrolytes is shown in Table 5.

Table 3: Incident light intensity in reactors according to lamp combinations

Lamps	Position	Incident intensity, I_0 (E L^{-1} s^{-1})
1-2	1	$4.37\times10^{-5} \pm 5.19\times10^{-6}$
1-2	2	$2.40\times10^{-5} \pm 5.19\times10^{-6}$
1-2	3	$1.35\times10^{-5} \pm 2.30\times10^{-6}$
3-4	1	$4.85\times10^{-5} \pm 1.18\times10^{-6}$
3-4	2	$2.59\times10^{-5} \pm 2.00\times10^{-6}$
3-4	3	$1.51\times10^{-5} \pm 8.53\times10^{-9}$

7.4.6 Sampling and error analysis

During the course of a typical photocatalytic experiment, samples were taken at specified time intervals using a pipette. The sample was serially diluted (Figure 25) and incubated as described in section 7.2.2 to determine the microbial survival. The appropriate dilution level for each time interval was plated in triplicate.

Table 4: Composition of working reaction solutions

Working solution#	1	2	3	4	5
Deionized water (mL)	18.60	18.58	18.40	18.10	17.60
10 g L^{-1} of P25 (mL)	0.00	0.02	0.20	0.50	1.00
5×10^{10} CFU L^{-1} cells (mL)	0.40	0.40	0.40	0.40	0.40
1×PBS (mL)	1.00	1.00	1.00	1.00	1.00
pH measurement	pH~7.3	pH~7.3	pH~7.3	pH~7.3	pH~7.3
Solution filled to 20 mL with deionized water and poured into reaction vessel					
Total volume (mL)	20	20	20	20	20
Final P25 conc. (g L^{-1})	0.00	0.01	0.10	0.25	0.50
Final cell count (CFU L^{-1})	1×10^9	1×10^9	1×10^9	1×10^9	1×10^9
Ionic strength (M)	0.01	0.01	0.01	0.01	0.01

Table 5: Composition of electrolytes in final solution

Constituent	Concentration (mM)
NaCl	6.85
KCl	0.14
Na_2HPO_4	0.50
KH_2PO_4	0.09

The standard deviation and standard error of viable counts for each sample were determined based on the Poisson distribution. The mean of triplicate experiments $\bar{x}$ was calculated in the usual way and relative error was determined according Equation (106).

$$e_r = \sqrt{\frac{1}{\bar{x}} + \sum_{i=1}^{m} {e_i}^2} \tag{106}$$

where e_r is the overall relative error and e_i is the error contribution from technical sources including volume measurements and dilutions. For the Poisson distribution, the mean $\bar{x}$ is equal to the variance σ^2. Therefore, the standard deviation is given as the square root of the mean.

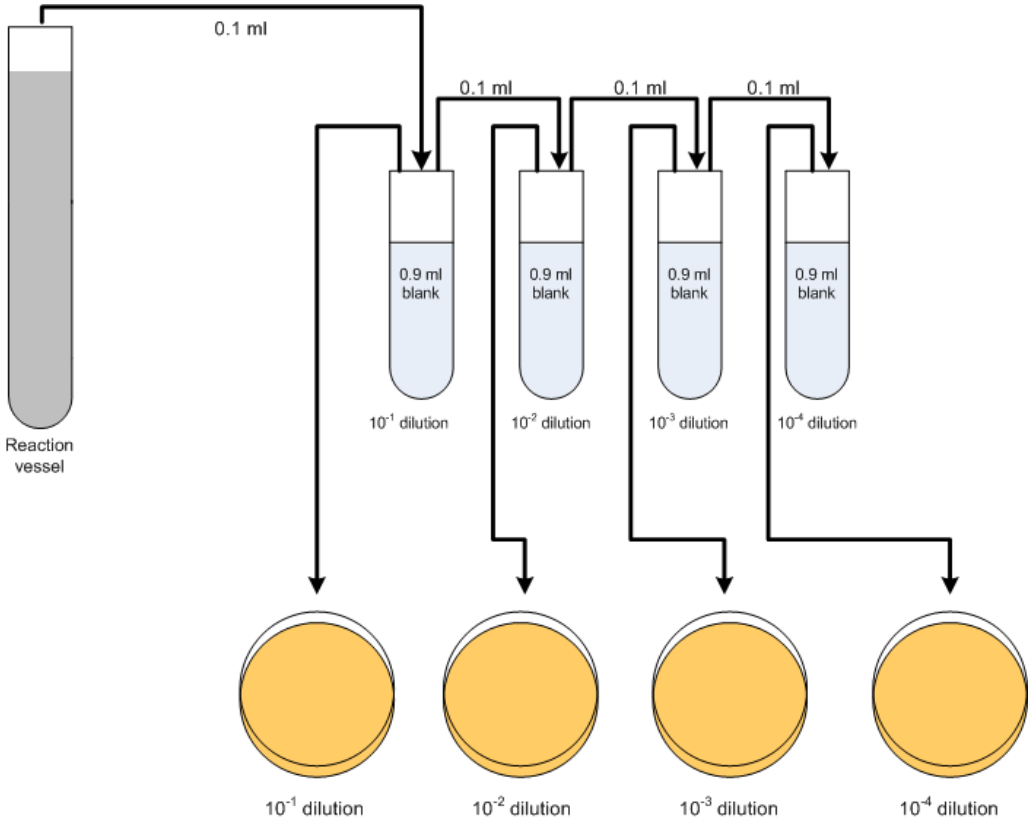

Figure 25: Schematic of serial dilution of sample

7.5 Fatty acid modification and analysis

Lipid modification of the *E. coli* cells was achieved by supplementing the Luria broth growth media with 32 µM of palmitoleic (C16:1 n-7), oleic (C18:1 n-9), and α-linolenic (C18:3 n-3) acids. These are long chain unsaturated fatty acids with the number of carbons, double bonds, and double bond location indicated in parenthesis respectively.

At least 20 mg of cells was harvested from an actively growing culture at 6 hours and twice pelletized by centrifugation at 1380 × *g* for 15 min in a 15-mL tube. The cell pellets were washed and suspended in sterile deionized water between centrifugation. The samples were sent frozen to Microbial ID (Newark, DE) to determine the fatty acid composition by fatty acid methyl ester (FAME) analysis. The general steps in a FAME analysis (Table 6) include extraction of the fatty acids by a procedure which consists of saponification in dilute sodium hydroxide/methanol solution, followed by derivatization with dilute hydrochloric acid/methanol solution to give respective methyl esters. The methyl esters are then extracted from the aqueous phase by the use of an organic solvent and the resulting extract was analyzed by gas chromatography (GC).

Table 6: Steps in FAME analysis

Step	Purpose
Harvesting	Removal of cells from culture media
Saponification	Lysis of cells to liberate fatty acids from cellular lipids
Methylation	Formation of fatty acid methyl esters (FAME)
Extraction	Transfer of FAMES from the aqueous phase to the organic phase
Base wash	Aqueous wash of the organic extract prior to GC analysis

7.6 Preparation and characterization of model cell membranes

7.6.1 Preparation of lipid film

The dominant phospholipids in the membrane of *E. coli* are phosphatidylethanolamine (PE) and phosphatidylglycerol (PG). These natural lipids were obtained from Avanti Polar Lipids (Alabaster, AL) dissolved in chloroform at a

concentration of 5 g L^{-1} each. The lipids were mixed in equal molar proportions. Higher ratios of PE to PG were initially used, but the stability of the liposomes was not consistent. The PE/PG solution was transferred to a clean and dry 100-mL round bottom flask and continuously rotated by hand in a water bath at 60°C until the solvent evaporated and a uniform thin lipid film was formed on the surface of the flask. A gentle stream of N_2 gas was passed over the film to remove solvent vapor. The flask was left overnight in a chemical hood to allow complete evaporation of all the chloroform.

7.6.2 Lipid film hydration and extrusion

The lipid films were hydrated with 5 mL of 1×PBS solution by continuously rotating the flask in the water bath maintained at 60^{o}C until all the film was completely dissolved (smooth milky white appearance). At this stage of the process, the lipids are present as sheets of hydrated lamellar films. In order to transform the films to the characteristic cell membrane structure, the solution was forced through 0.8-µm polycarbonate membrane. This size reduction step was performed using a mini extruder obtained from Avanti Polar Lipids (Alabaster, AL). It consisted of two 1-mL syringes inserted on opposite ends of a filter support assembly. The solution is passed from one syringe to the other across the filter. The entire assembly sits on a custom-fit heating block. The extruder was maintained at 60^{o}C and the solution was passed 12 times across the membrane.

7.6.3 Size distribution measurement

The size distribution of the liposomes was determined by photon correlation spectroscopy using a Malvern Zetasizer Nano series device. The liposome suspension was diluted with 1×PBS prior to measurement.

7.6.4 Transmission electron microscopy

A drop of the PE/PG solution was placed on a Formvar carbon film with 150 square mesh copper grids and visually examined with a FEI Morgagni 268 TEM after staining with 0.50% uranyl acetate in water. The TEM was operated at 60kV and an Olympus Soft Imaging MegaView III camera was used to collect images.

7.7 Measurement and analysis of byproducts

7.7.1 MDA assay

A thiobarbituric acid reactive species (TBARS) assay kit was obtained from Northwest Life Science Specialties (Vancouver, WA) and used to measure MDA in the samples. Aliquots of 250 µL sample solution were added to a micro-centrifuge vial containing 10 µL of butylated hydroxytoluene (BHT), an antioxidant. The acid reagent (250 µL) was added and the mixture was centrifuged at 11,000 × g for 35 min and then for an additional 20 min to remove solids. The supernatant was transferred to new vials and 250 µL of thiobarbituric acid (TBA) reagent was added. The mixture was vigorously shaken on a vortex for 5 counts and then incubated in a water bath at 60°C for 1 hour. After incubation, the solution was centrifuged at 10,000 × g for 3 minutes and absorbance of the supernatant was recorded from 400-700 nm on an Ocean Optic USB2000

spectrometer using the OOIBase 32 software and DH-2000-BAL UV-VIS light source. The spectrometer was calibrated with a standard mercury emission lamp according the manufacturer's instructions prior to measurement.

7.7.2 Derivative spectroscopy analysis

Derivative spectroscopy analysis was performed on the absorbance spectra to negate the effects of non-linear baselines and enhance the spectral signals. A smoothing function was first applied to the spectra according to the method by Savitzky and Golay [222]. The second derivative was then selected and the absorbance evaluated at 511 nm. The technique was programmed into a computer code to ensure that the same treatment was performed on all the spectra.

7.7.3 LOOH assay

A lipid hydroperoxide analysis kit was obtained from Northwest Life Science Specialties (Vancouver, WA). The method is based on the fact that a hydroperoxide present in solution oxidizes ferrous iron (Fe^{2+}) to ferric iron (Fe^{3+}) under acidic conditions [188, 223]. The resulting ferric iron was detected using xylenol orange, which forms a Fe^{3+}-xylenol orange complex. The complex was measured on a spectrophotometer at 560 nm. The manufacturer's assay protocol was followed precisely, except for an additional final centrifugation step to remove solids in the samples.

CHAPTER 8: RESULTS AND DISCUSSION

8.1 Fatty acid modification and analysis

The fatty acid profile of the unmodified *E. coli* was a close match to published profiles of the organisms; see for example [105, 215, 224]. The distribution of the main fatty acids is shown in Table 7 (see Appendix B for full list). The predominant fatty acid was the saturated 16-carbon (palmitic acid). Palmitoleic (C16:1 n-7) and *cis*-vaccenic (C18:1 n-7) acids were present in equal proportions and accounted for most of the monounsaturated content. The total polyunsaturated fatty acid content was below 0.50%. Organisms supplemented with oleic acid (C18:1 n-9) had an enrichment of this fatty acid in their membrane, even though it was not detected in the control population. The enrichment of oleic acid was accompanied by a reduction in its positional isomer, *cis*-vaccenic acid.

The addition of α-linolenic acid (C18:1 n-3) had a pronounced effect on the fatty acid distribution. The presence of α-linolenic was not detected in the samples indicating that the supplemental fatty acid was converted by the organisms to other less unsaturated fatty acids. There were significant changes particularly in the C18:1 group of fatty acids and the appearance of a small fraction of C18:2 in the organism.

Table 7: Percent distribution of major fatty acids

Fatty acids	Unmodified cells[1]	Fatty acid supplement			Lipid Vesicles[2]
		C16:1 n-7	C18:1 n-9	C18:3 n-3	
Saturated					
C14	8.5	7.0	7.6	7.4	1.8
C15	1.9	1.5	1.6	1.5	8.5
C16	34.8	35.0	31.9	32.6	28.8
C17	2.1	2.0	1.6	2.1	10.9
C18	0.6	0.4	0.3	1.0	0.0
Monounsaturated					
C16:1 n-7	12.5	19.9	5.2	9.5	7.1
C18:1 n-7	12.6	8.6	6.7	17.3	17.1
C18:1 n-9	0.0	0.0	22.2	2.8	4.5
Polyunsaturated					
C18:2 n-6	0.4	0.4	0.0	2.7	0.0
Cyclopropane					
C17	11.1	11.4	6.3	9.0	14.5
C19	1.3	0.5	1.9	1.2	4.0
Total saturated	73.2	70.3	63.6	66.6	68.5
Total unsaturated	26.2	29.2	35.9	32.8	28.7
Unsaturated/Saturated	0.4	0.4	0.6	0.5	0.4

[1]*E. coli* cells grown in Luria broth and harvested at 6 hours. Only major fatty acids are shown. Total fatty acids include all fatty acids detected in analysis. See supplemental information
[2]Fatty acid spectra obtained from manufacturer

8.2 Factorial analysis: Main effects

In order to make fair comparisons across all groups, the log survival at 20 minutes was selected as the response variable to perform the factorial analysis. This corresponded with the shortest experimental time. Survival data are usually distributed log-normally and this was confirmed by conducting a probability plot as shown in Figure 26.

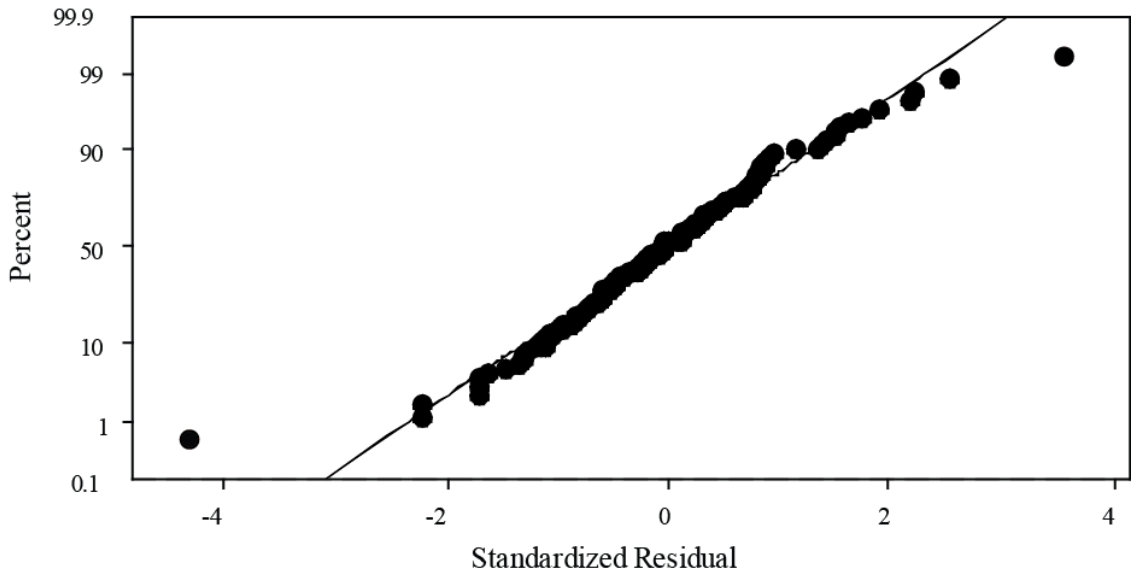

(a) normal probability plot

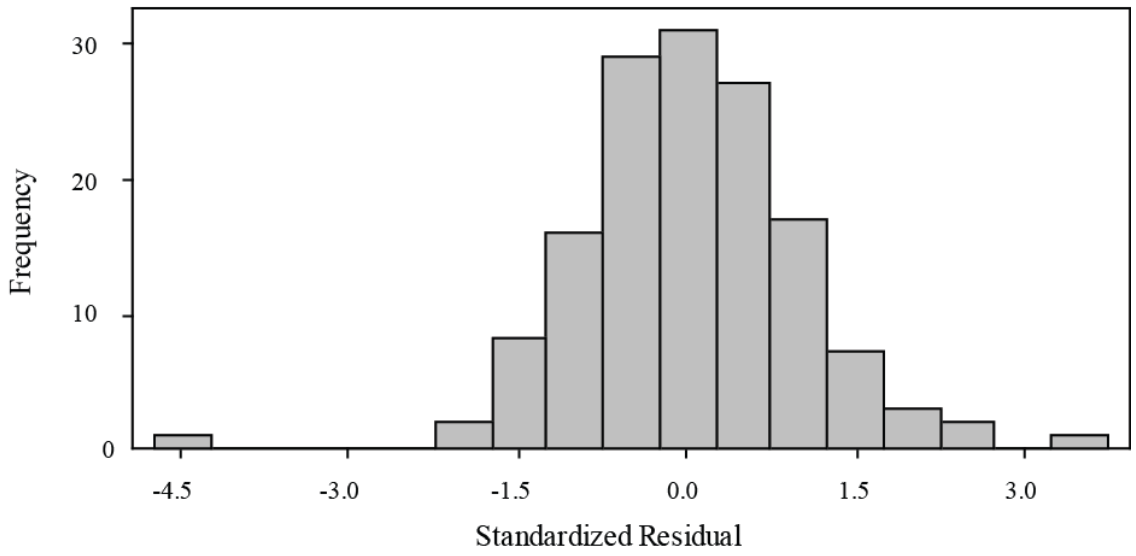

(b) histogram

Figure 26: Probability distribution of survival data for *E. coli*

The main effects are illustrated in Figure 27. The mean of the log of survival is plotted on the vertical axis against the levels of each factor.

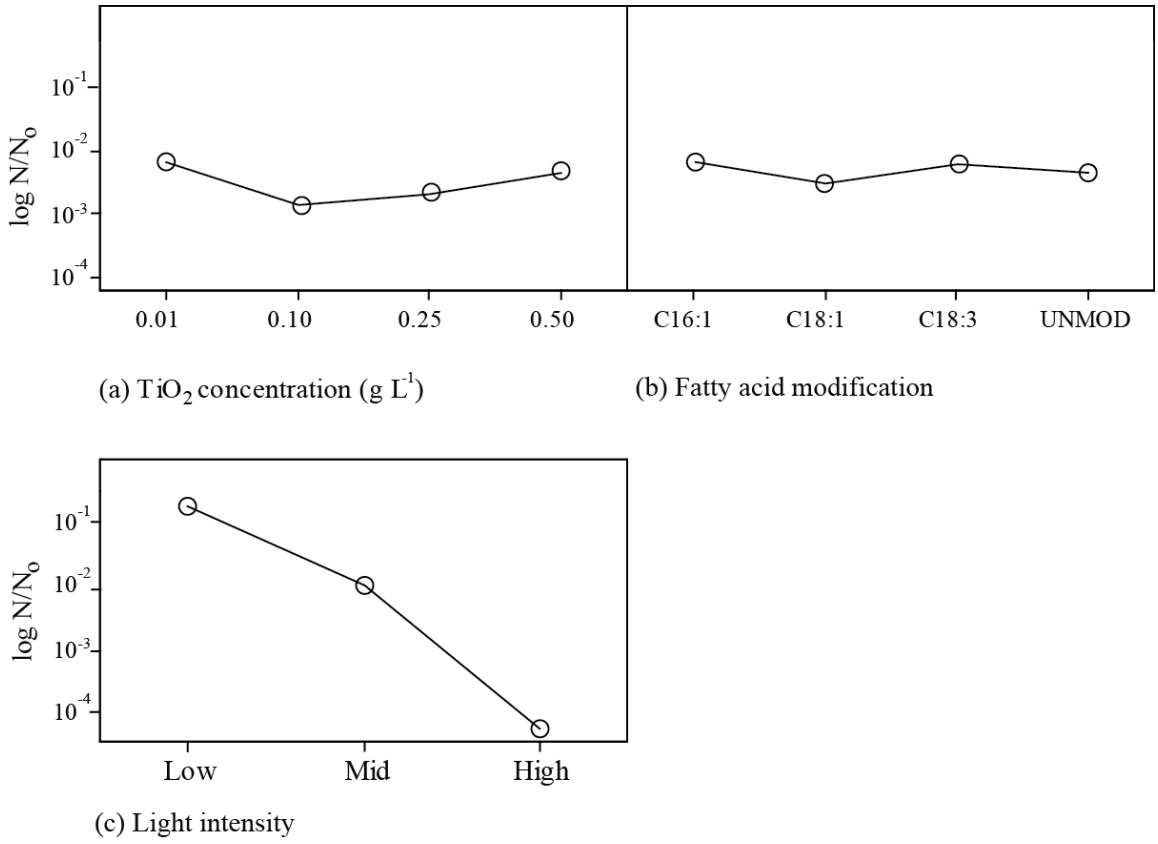

Figure 27: The main effects plots for (a) TiO_2 concentration; (b) fatty acid modification; and (c) light intensity on mean survival data at 20 min

8.2.1 Light intensity

In the study, light intensity was confirmed as the most significant effect on the disinfection process (Figure 27c). Figure 28 shows the variation in survival for the three different light intensity levels at the lowest TiO_2 concentration. The trend is typical for other concentrations, except that the variation is greatest at concentration value shown. Many workers have found that the disinfection rate is usually proportional to the square root of light intensity at relatively high photon fluxes and linear at low flux [22, 23, 158, 160, 225, 226]. The latter is true for this study. Compared to most literature values, the intensity levels used in this research would be classified as low fluxes. The results

indicate that disinfection response is linearly proportional to light intensity as illustrated in Figure 29.

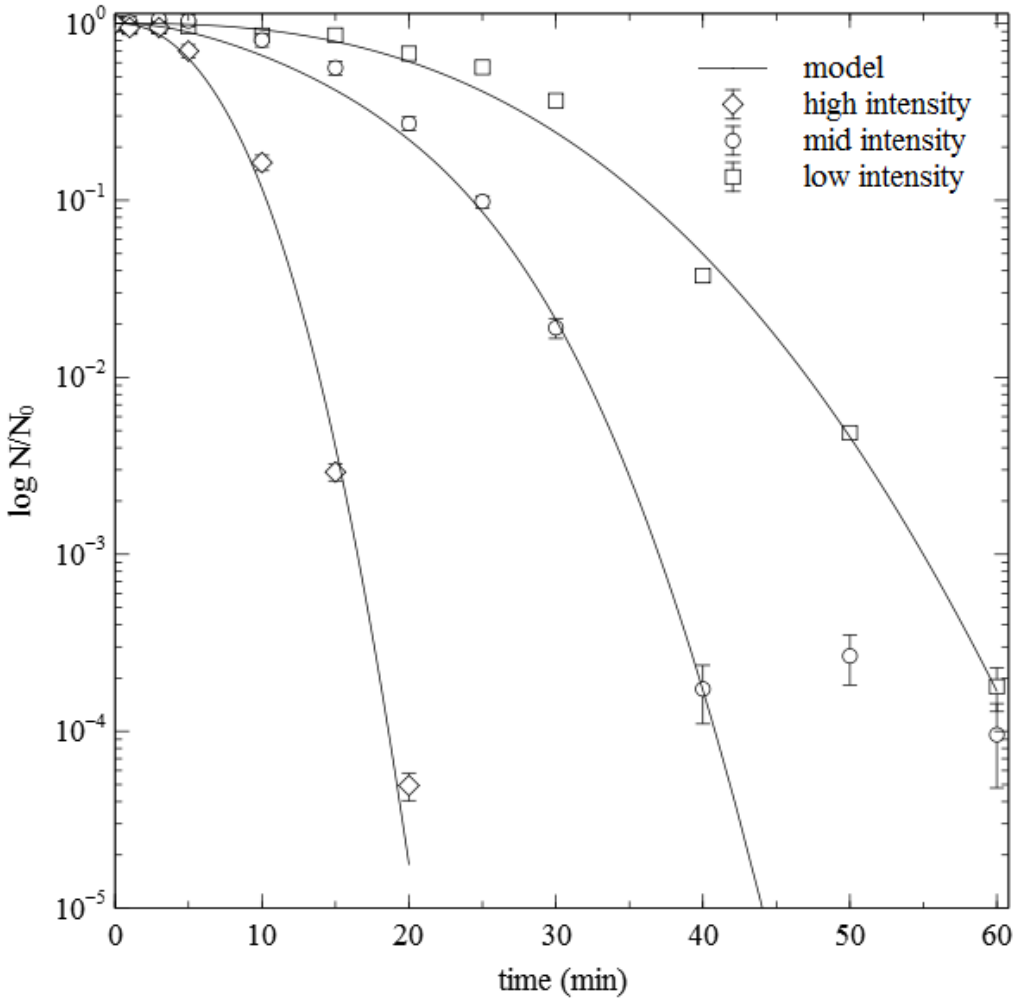

Figure 28: Effect of light intensity on disinfection for control organisms at 0.01 g L^{-1} Degussa P25 TiO_2

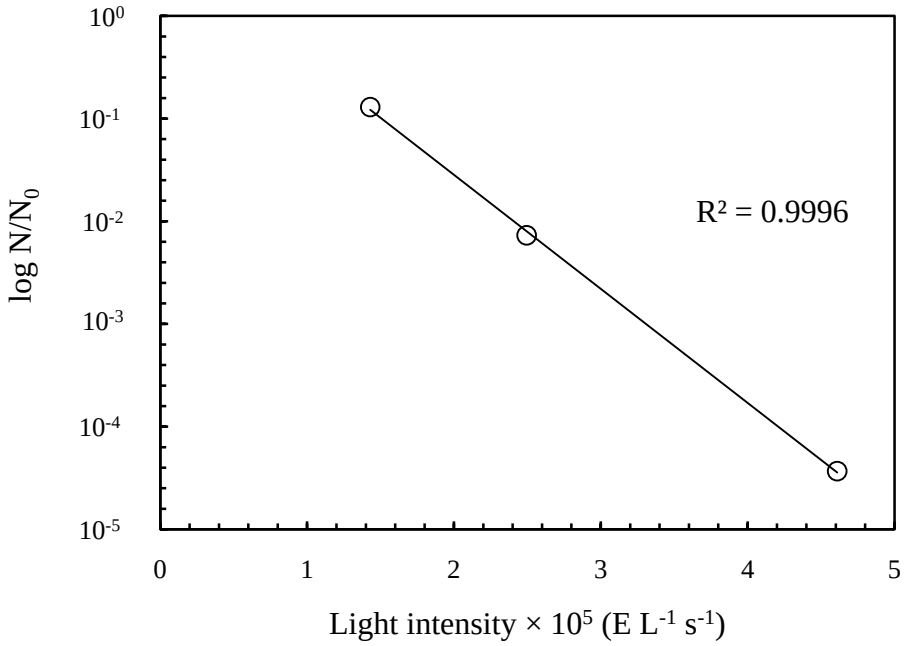

Figure 29: Relationship between intensity and average survival at 20 min

This behavior is directly related to the generation of hydroxyl radicals that occurs as a result of the interaction of the catalyst and light energy. At high light intensity the recombination of the electron-hole pair is enhanced, while at low fluxes OH radical formation can compete with recombination [227-229]. Further, the rate becomes independent of light intensity at higher fluxes and the expected rate-limiting factor becomes the mass transfer [230].

8.2.2 TiO_2 concentration

The average across all factors (light intensity and fatty acid distribution) shows that disinfection levels at 20 minutes had a log linear relationship with catalyst concentration from 0.10-0.50 g L^{-1} of TiO_2 (Figure 30). Disinfection is much lower on average for 0.01 g L^{-1}. However, it must be kept in mind that these are main effects; the

results are averages for the various combinations. Specific interactions are discussed in the next section. The interaction between light intensity and catalyst concentration produced completely different results.

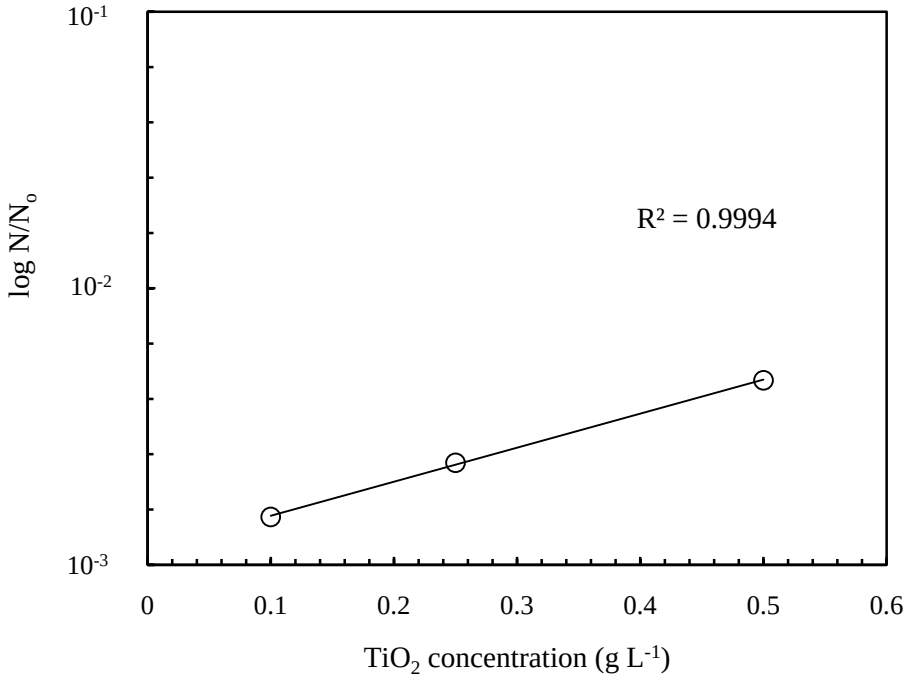

Figure 30: Log-linear relationship between relatively high catalyst concentration (0.10-0.50 g L^{-1}) and *E. coli* survival

Without reference to the specific interactions, the general trend for increased disinfection is to reduce catalyst concentration. Block et al [34] made this observation for a similar range of catalyst concentrations. This behavior is a direct result of colloidal absorption phenomena and light distribution in the reactor. The surface coverage of catalyst particles on the cells is expected to be relatively lower at low concentrations of TiO_2. Very high catalyst concentrations (>0.5 g L^{-1}) actually result in destabilization of the colloidal suspension. As the catalyst concentration is increased without a change in

pH, the condition for heterocoagulation is met as the total interaction energy V_T of the colloidal system approaches zero according to Equation (34) [125]. The result is that the catalyst and microbes particles co-flocculate and rapidly settle out of solution (Figure 31).

Since the process is synergistic, that is, it depends on the interaction of light and TiO_2, the level of disinfection is significantly reduced due to the increase shading and scattering of light in high TiO_2 suspensions. It indicates that the effectiveness of the process is determined by some optimum surface coverage and a maximum penetration of light. Beyond these values, increased catalyst concentration retards the disinfection process.

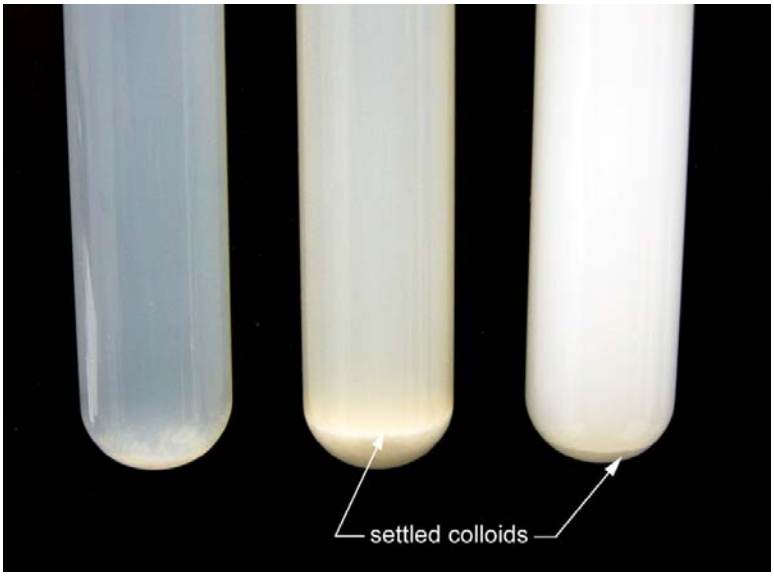

Figure 31: Instantaneous formation and settling of TiO_2-cell aggregates; stable solution of 0.10 g L^{-1} TiO_2 with 1×10^6 CFU mL^{-1} cells (left); highly unstable suspension of 1 g L^{-1} TiO_2 with 1×10^9 CFU mL^{-1} cells; and unstable suspension of 1 g L^{-1} with 1×10^6 CFU mL^{-1} cells

8.2.3 Fatty acid modification

The effect of fatty acid modification on disinfection did not show a statistically significant difference at the 95% confidence level ($p = 0.071$). Even when the fatty acid modification is analyzed at a specific intensity and catalyst concentration, there are no significant differences. Other researchers [231] working with lipids found that monounsaturated fatty acids tend to retard the progression of peroxidation by acting similar to antioxidants [231]. It is believed that they may react with radicals, but somehow slow their progression and block radical chain reactions. However, the specific explanation for this result is still not yet very clear. Even if the same effect is true in *E. coli*, the effect is not significant in the overall disinfection of the organism for the variation of fatty acids in the study. It indicates that while peroxidation of the cell membrane is a key process during disinfection, small changes in the fatty acid content are not sufficient to cause major changes in the disinfection kinetics.

8.3 Interaction effects: Light intensity and TiO_2 concentration

Light intensity and catalyst concentration are evidently the two most important factors to be considered for photocatalysis. The interaction of these two factors is significant at all levels ($p = 0.000$). By analyzing the main effects, it can be seen that disinfection efficiency increases as light intensity increases and catalyst concentration decreases. Even though there is some minor sensitivity to high light intensity (result not shown), disinfection was always greater in the presence of the catalyst. At low and mid light intensity there is much less variation in effectiveness for concentrations from 0.10-0.50 g L^{-1} TiO_2 (Figure 32). Also, the effectiveness at the same light intensity for 0.01 g

L^{-1} is much less at the chosen time interval when compared to all other concentration values.

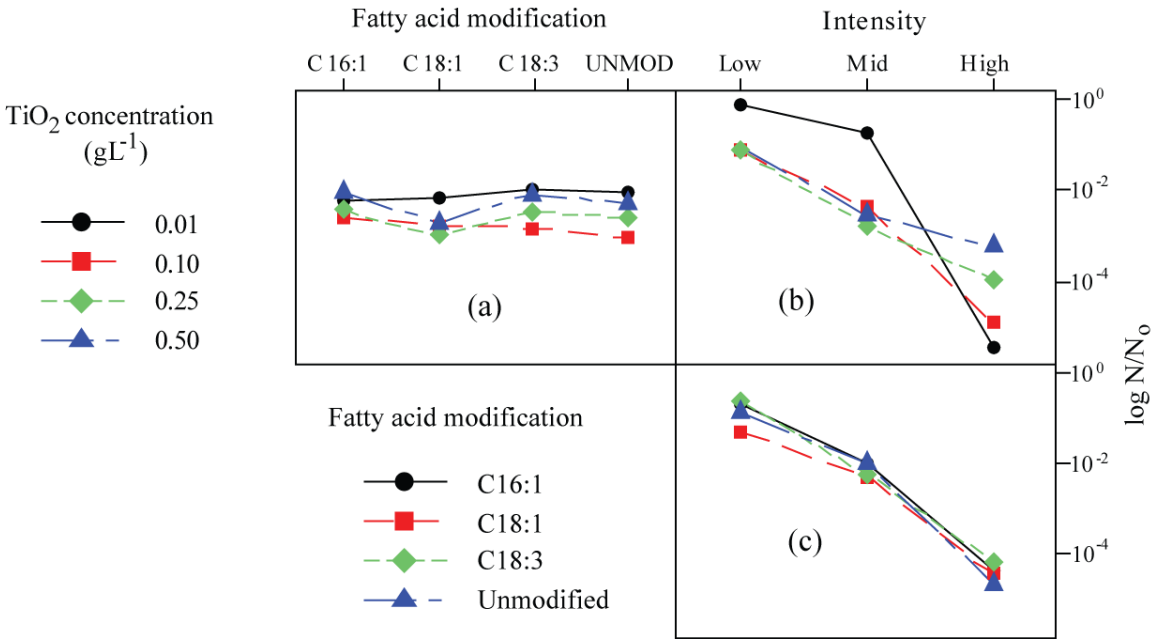

Figure 32: Interaction plots for the three independent factors at 20 min: (a) fatty acid modification vs. TiO_2 concentration; (b) light intensity vs. TiO_2 concentration; and (c) fatty acid modification vs. light intensity.

At high light intensity the interaction effects change dramatically. The lowest concentration of TiO_2 becomes the most effective and the effectiveness decreases with catalyst concentration across 2 orders of magnitude (Figure 33). By doubling the light intensity from the mid to high position, an increase of 5 log units of disinfection was achieved within the same 20 minutes. Whereas, the same increase in light intensity for other concentrations produced much less disinfection (Figure 32).

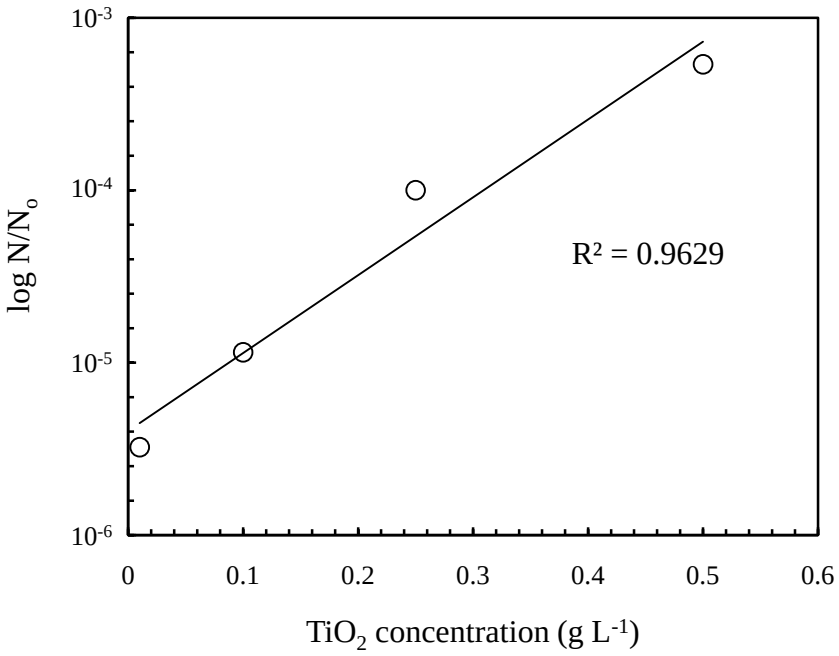

Figure 33: Relationship between survival and TiO_2 concentration at high light intensity

The interaction between light intensity and catalyst concentration is the most important interaction because the main oxidants in the disinfection process are produced as result of the absorption of light by the catalyst. However, with increasing catalyst concentrations, the reaction solution becomes saturated and only a portion of the particles receive irradiation. Although more surface area may be available for reaction, the additional catalyst particles do not participate in the reaction and the reaction rate does not increase with growing catalyst load beyond the optimum level [232].

Three main factors are responsible for these observations; colloidal adsorption and interaction, light transmission through the solution, and ·OH generation. The interaction of these phenomena is illustrated in the simple model of Figure 34.

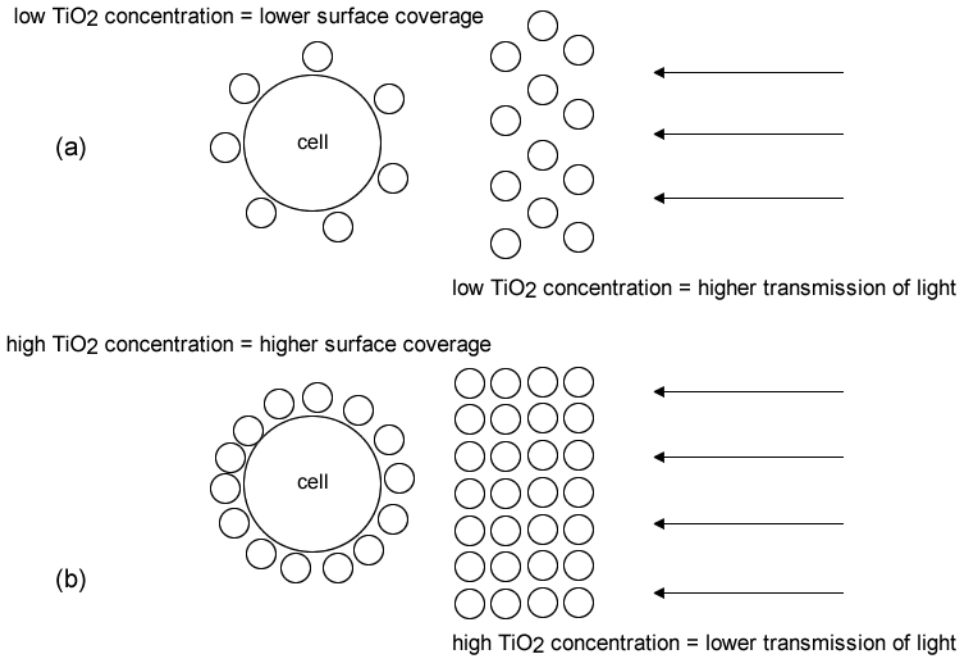

Figure 34: Particle interaction and light transmission in TiO_2 suspensions

Firstly, the effects of absorption of TiO_2 unto a bacterial surface can be theoretically illustrated based on colloidal absorption theory. From TEM analysis it appears that there is very strong specific adsorption between the TiO_2 particles and microbial cells at neutral pH. According to Figure 35, the catalyst particles (dark spots) are bound to the cells (rod-shaped features). They also form secondary layers or clusters with each other in some areas. It is interesting to note that the TiO_2 particles are not found in isolated areas with themselves, but predominantly occur with the cells.

Further, when the theoretical adsorption kinetics of TiO_2 to the cell surface is analyzed, it reveals that there is a transition from linear to non-linear adsorption for the range of TiO_2 concentration used in the research. Linear adsorption occurs when the existing adsorption of particles at the bacterial surface does not significantly prevent

other particles from adsorbing [148]. This occurs mostly at low particle concentrations ($<10^{12}$ mL^{-1}).

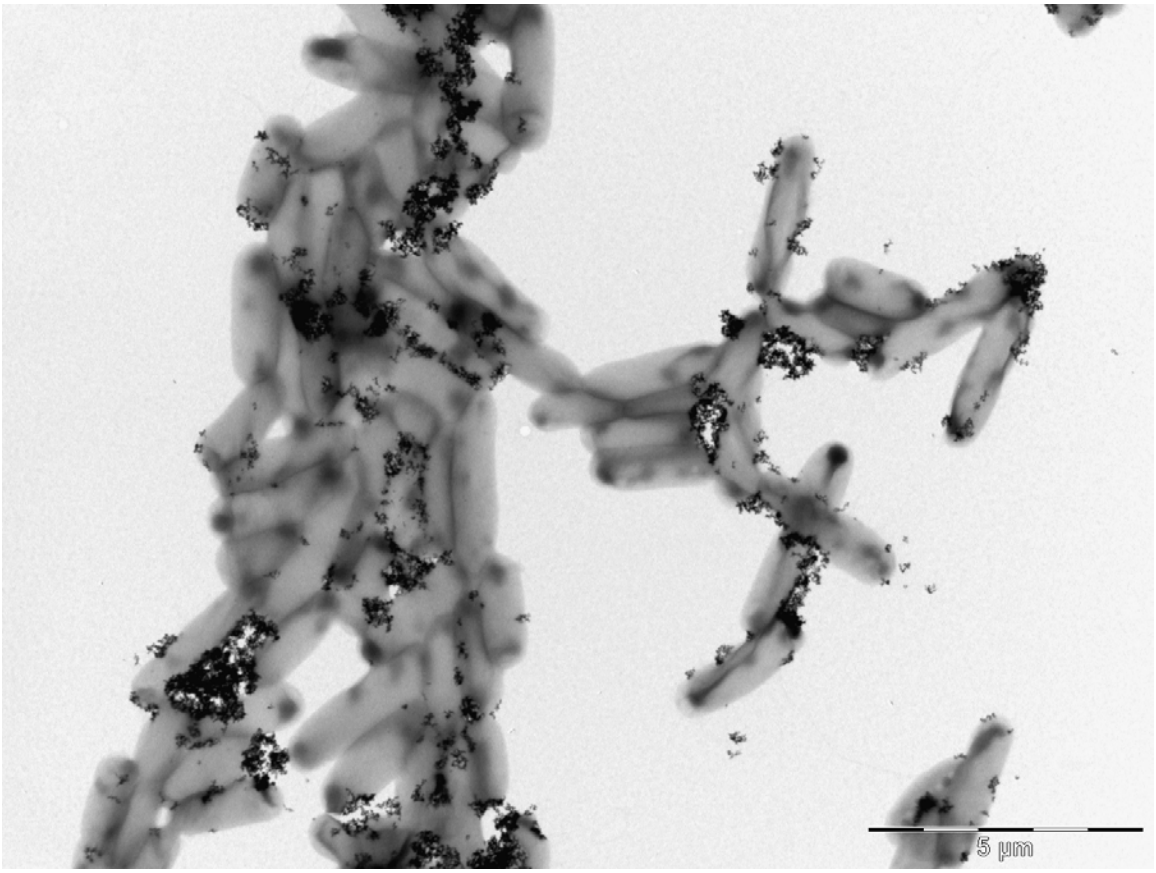

Figure 35: TEM image of TiO_2 particles (dark spots) attached to *E. coli*. Images courtesy of Integrative Biology Microscopy Core Facility, University of South Florida.

However, at higher particle concentrations, the existing coverage blocks other particles and prevents access to the surface. Under these circumstances, if TiO_2 particles could be viewed as carriers of hydroxyl radicals, then it is easy to see that the access of radicals to the surface is also reduced under high concentration. However, for concentrations ranging from 0.10 to 0.50 g L^{-1}, this effect does not vary significantly. At

concentration values lower than 0.01 g L^{-1} it appears that this phenomenon is important. Based on Equations (80) and (81), the concentrations that produce linear and non-linear adsorption under flow and no-flow conditions can be estimated as shown in Figure 36. The lower domain of the curves shows the region where linear adsorption occurs. According to the figure, the given TiO_2 concentrations all lie within the non-linear adsorption phase for flow conditions.

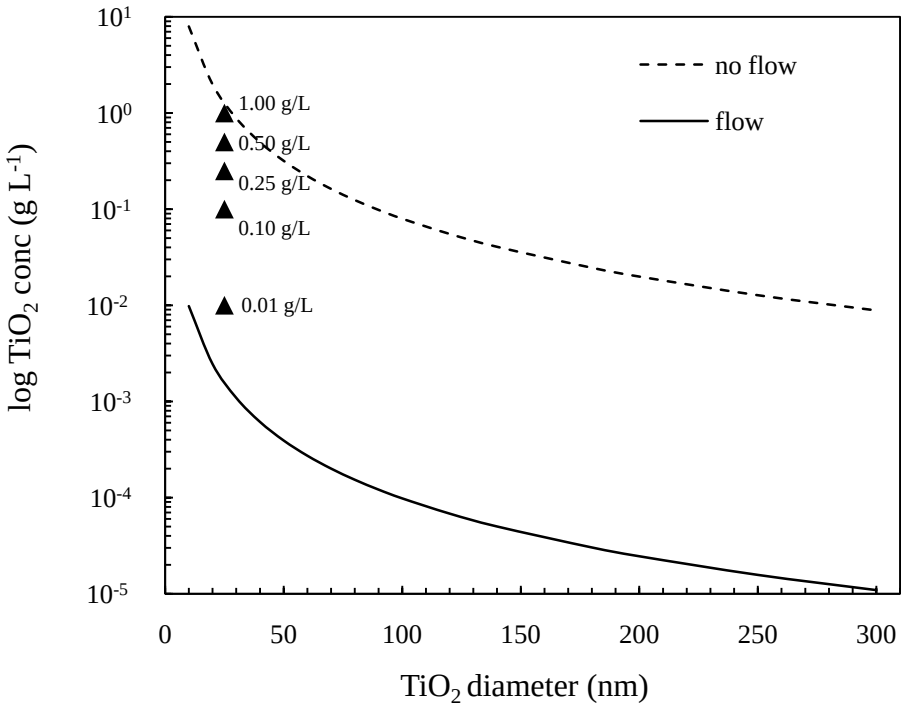

Figure 36: Dependence of limiting catalyst concentration and catalyst diameter

The TiO_2 particle number density was estimated according to published data available for the P25 catalyst such as specific surface area and particle size.

Even though the RSA model does not account for hydrodynamic forces very well, it was still used to estimate the adsorption kinetics for the given concentrations (Figure 37). It can be shown that the equilibrium coverage is reached within seconds, even though the kinetics is relatively slower for 0.01 g L^{-1}. However, given the time scale of the experiments it can be assumed that the surface coverage is similar for all TiO_2 concentrations and ranges between 20-25%.

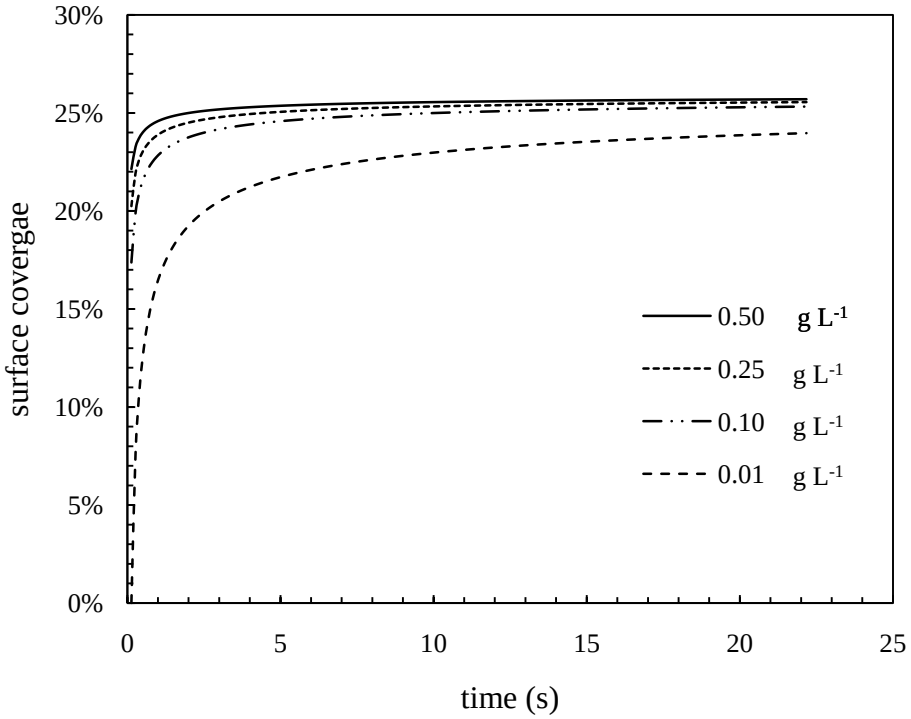

Figure 37: Theoretical adsorption kinetics of TiO_2 particles (25 nm dia.) unto *E. coli* surface under hydrodynamic conditions (stir speed was 600 rpm in test tube reactor)

According to colloidal adsorption processes, hydrodynamic shear forces tend to reduce surface coverage. For a catalyst particle of radius of 25 nm, cell radius of 1000 nm, and

TiO_2 concentration of $4x10^{-12}$ mL^{-1} (0.10 g L^{-1}), there is an estimated theoretical initial surface coverage of 52%, which is reduced to 25% at equilibrium under flow conditions.

The second important factor, light transmission, varies with TiO_2 concentration as well. There is usually an uneven distribution of light in a TiO_2 reactor because the light is attenuated as it is transmitted through the solution. As much as 50 percent of the incident light can be absorbed within the first 30 mm from the reactor wall in a suspension of 0.50 g L^{-1}. A light transmission test was conducted to develop the profile of light through the reactor used in this study. TiO_2 suspension corresponding to the various concentrations was gradually added to a borosilicate Petri plate of similar thickness to the reactor test tube. The light intensity passing through the solution was measured with a UV radiometer placed directly below the plate. The transmission of light is plotted in Figure 38.

More than 95% of the incident light passes directly through a suspension of 0.01 g L^{-1}, while just about 1% passes through 0.5 g L^{-1}. Based on the analysis, an exponential decay of light intensity inside the reactor could be established according to:

$$I_t = I_0 \exp(-\alpha\, c_{cat} x_{rw}) \tag{107}$$

where I_t is the transmitted light intensity, α is the coefficient of attenuation per mass concentration of catalyst (L g^{-1} cm^{-1}), c_{cat} is the mass concentration of catalyst (g L^{-1}), and x_{rw} is the distance from the reactor wall (cm). The coefficient of attenuation was found to be 0.72±0.10 L g^{-1} cm^{-1}.

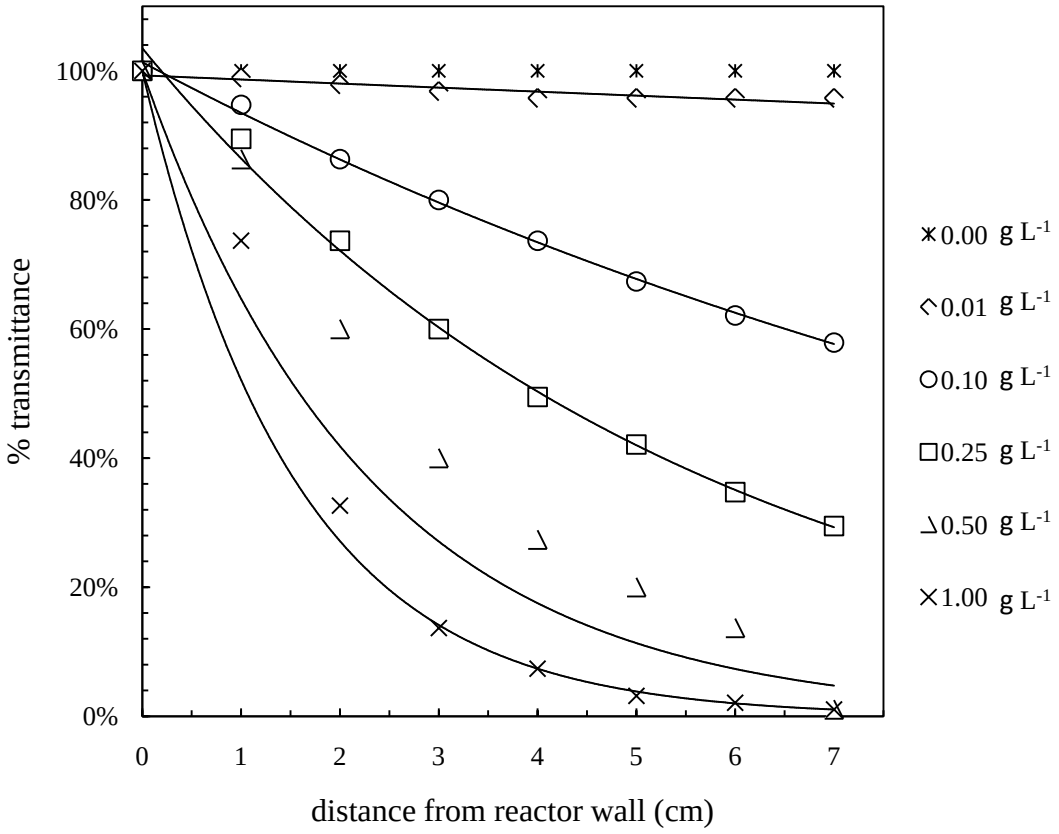

Figure 38: Light transmission through reactor at high light intensity

According to Figure 38, active photocatalytic activity occurs within a gradually reducing zone close to the reactor surface as the concentration is increased. This means that microorganisms in high concentration suspensions are not exposed to the light as frequently as organisms in lower concentration suspensions [84, 154]. Since the bacterial surface coverage of catalyst particles is comparable for all concentrations used in the study, it is clear to see why light intensity has the largest overall effect on the process under the given conditions. This information was used to update the code for the model by writing an algorithm which accounts for the radial variation of intensity in the reactor. Equations (100) and (104) were adjusted accordingly,

$$\frac{d[cell]_l}{dt} = \int_0^r \{-k_{dis}[\cdot \mathrm{OH}]^n [cell]_l{}^y\} \pi r \, dr \quad (108)$$

$$\frac{\mathrm{d}[\cdot \mathrm{OH}]}{\mathrm{dt}} = \int_0^r \{G_{\cdot \mathrm{OH}}(1 - \theta_{An} - \theta_{BP}) - k_{dis}[\cdot \mathrm{OH}]^x [\mathrm{cell}]_l{}^y\} \pi r \, dr \quad (109)$$

where r is the radius of the reactor.

Finally, the generation of OH radicals accounts for the significant influence of light intensity and catalyst concentration. The generation of OH radicals as given by Equation (89) depends on the integrated absorption fraction F_s of the catalyst suspension (see Equation (88)). Values of F_s were determined by Sun and Bolton [158]. The absorption fraction increases to a maximum with TiO_2 concentration. Beyond about 0.10 g L^{-1}, there is no significant increase. Values for F_s were interpolated and extrapolated to construct Figure 39, which shows the expected OH radical generation rate as a function of catalyst concentration.

There is no significant increase in the generation rate $G_{\cdot OH}$ for catalyst suspensions exceeding 0.1 g L^{-1}. However, the influence of the generation rate on the interaction effect is made much more apparent when the generation rate per mass or per particle is considered (Figure 40). There is an exponential drop in the generation rate per mass of catalyst beyond 0.1 g L^{-1}. This is a clear indication that the additional catalyst particles reduce the efficiency of the process.

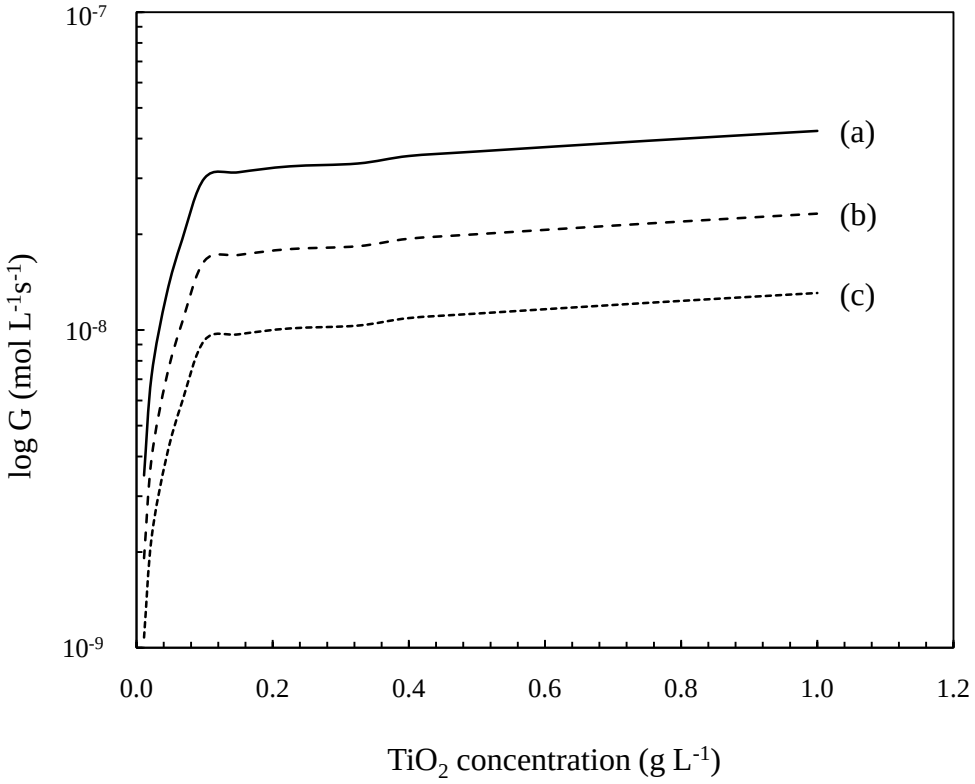

Figure 39: OH radical generation rate in TiO_2 suspension at pH 7 in deionized water; (a) high intensity $I_0 = 4.37\times10^{-5}$ E L^{-1} s^{-1}, (b) mid intensity $I_0 = 2.40\times10^{-5}$ E L^{-1} s^{-1} and (c) low intensity $I_0 = 1.35\times10^{-5}$ E L^{-1} s^{-1}

In conclusion, the significance of the interaction of TiO_2 and light intensity on disinfection favors lower catalyst concentration and higher light intensity within an optimum range. At low TiO_2 concentrations, the colloidal suspension is more stable, the distribution of light is fairly uniform, and there is a higher radical generation rate per mass of catalyst.

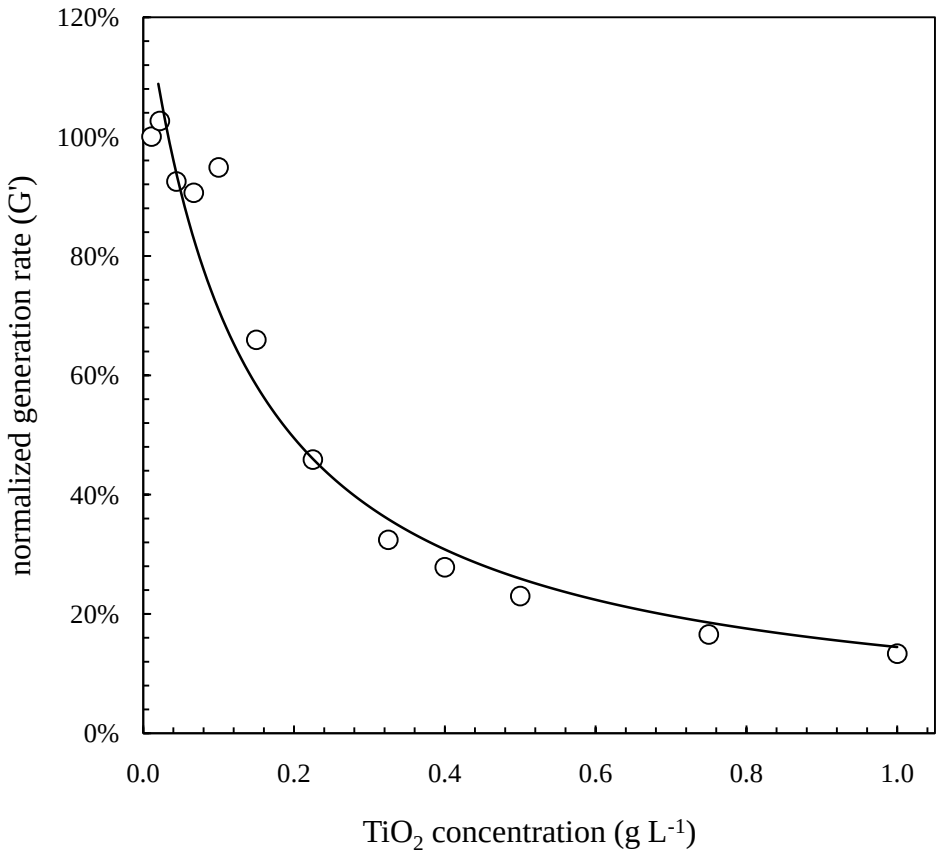

Figure 40: Dependence of normalized OH radical generation rate on catalyst concentration

8.4 Model validation

8.4.1 Inputs and fitting parameters

The model developed in the study was very complex, but potentially useful for estimating the effect of a number of parameters such as catalyst concentration, light intensity, salt concentration, and pH. Inputs to the model included published data on adsorption constants for anions (Table 2), electrolyte concentration (Table 5), the integrated adsorption fraction for specific catalyst concentrations (Figure 16), the incident light intensity (Three sets of control experiments were conducted; (1) solution of catalyst

and microbes with no light (dark experiments); (2) irradiated solutions of microbes with no catalyst present (irradiated blank); and (3) non-irradiated solution of microbes only (organism control). The final composition of the reaction solution was made up by adding the appropriate volumes of stock solutions together and then pouring the mixture into the reaction vessel (Table 4). The final composition of electrolytes is shown in Table 5.

Table 3), the reactor radius, and the quantum yield of OH radical generation according to Sun and Bolton [158]. The entire model was solved numerically using a fifth-order Runge-Kutta method in MATLAB coupled with a least-square solver to obtain three unknown parameters; these included the disinfection rate constant k_{dis}, the reaction order with respect to OH radicals n, and the OH radical consumption rate constant k_{OH}. This is a particular strength of the model. It is able to utilize predetermined values without the need to over fit the model with too many unknown independent parameters.

The expectation of the fitting procedure was that the rate constants and reaction order should not vary significantly, particularly for a given organism. Previous studies have reported dependence of the rate constant on TiO_2 concentration [21], but this study considered that to be at odds with reaction kinetic theory. Table 8 and Table 9 show the fitting parameters and the coefficient of determination of the regression (R^2). However, much confidence cannot be placed in the R^2 value because the data was fitted across many orders of magnitude. This means that the least-square procedure is biased towards the largest numbers which occur at the beginning of the survival curve. A more reliable test was to observe the overall survival curve shape and make actual comparisons

between the final predicted disinfection values and experimental results. Further, to improve the accuracy of the fit, the least-square fit was performed between a unit matrix and the reciprocal of the model data multiplied by the experimental values.

Table 8: Rate constants and reaction order as predicted by the model for unmodified and C16:1 modified organisms

		Unmodified				C16:1			
	TiO2	k_{dis} ($pM^{-n}s^{-1}$)	n (-)	k_{OH} ($L^n CFU^{-1} s^{-1} pM^{n-1}$)	R^2	k_{dis} ($pM^{-n}s^{-1}$)	n (-)	k_{OH} ($L^n CFU^{-1} s^{-1} pM^{n-1}$)	R^2
HIGH	0.01	1.50E+05	1.3	1.00	0.988	1.16E+05	1.2	3.36	0.984
	0.10	9.30E+04	1.5	3.49	0.963	1.33E+04	1.3	1.00	0.998
	0.25	3.43E+05	1.6	1.08	0.985	1.59E+04	1.3	1.00	0.971
	0.50	1.49E+05	1.4	1.72	0.968	5.78E+04	1.4	1.00	0.947
MID	0.01	1.15E+05	1.3	4.25	0.969	1.47E+05	1.4	2.78	0.933
	0.10	1.05E+04	1.3	1.00	0.995	1.32E+04	1.3	1.00	0.992
	0.25	1.46E+04	1.2	1.00	0.984	1.71E+04	1.3	1.00	0.991
	0.50	3.32E+05	1.5	1.00	0.979	3.84E+04	1.3	1.00	0.988
LOW	0.01	7.50E+05	1.6	1.00	0.968	2.17E+05	1.5	1.00	0.982
	0.10	1.69E+04	1.3	1.00	0.981	3.35E+04	1.4	1.00	0.987
	0.25	4.94E+04	1.4	1.00	0.941	9.16E+05	1.8	1.00	0.960
	0.50	1.50E+05	1.6	2.34	0.992	9.31E+04	1.5	1.00	0.948

Table 9: Rate constants and reaction order as predicted by the model for C18:1 and C18:3 modified organisms

		C18:1				C18:3			
	TiO2	k_{dis} ($pM^{-n}s^{-1}$)	n (-)	k_{OH} ($L^n CFU^{-1} s^{-1} pM^{n-1}$)	R^2	k_{dis} ($pM^{-n}s^{-1}$)	n (-)	k_{OH} ($L^n CFU^{-1} s^{-1} pM^{n-1}$)	R^2
HIGH	0.01	2.53E+05	1.4	1.00	0.956	1.59E+05	1.3	1.00	0.970
	0.10	6.48E+04	1.5	1.00	0.966	5.69E+04	1.5	3.56	0.987
	0.25	1.78E+04	1.3	1.00	0.983	1.01E+05	1.4	3.29	0.995
	0.50	2.30E+04	1.3	1.00	0.993	2.02E+04	1.2	1.00	0.999
MID	0.01	1.35E+05	1.3	3.40	0.971	5.93E+05	1.5	1.32	0.922
	0.10	9.82E+03	1.2	1.00	0.966	3.45E+04	1.3	3.49	0.943
	0.25	4.37E+04	1.4	1.00	0.996	3.06E+04	1.3	1.00	0.986
	0.50	7.11E+04	1.4	1.00	0.977	4.52E+04	1.4	1.00	0.981
LOW	0.01	1.62E+05	1.3	8.44	0.857	4.74E+05	1.6	1.00	0.974
	0.10	1.26E+04	1.3	1.00	0.991	1.12E+04	1.3	1.00	0.966
	0.25	1.75E+04	1.3	1.00	0.996	9.67E+03	1.2	1.00	0.975
	0.50	6.30E+04	1.2	1.00	0.952	1.00E+06	1.7	1.00	0.951

Since the concentration of OH radicals measured in TiO_2 suspensions is usually very low [68, 233], the use of pico-moles appears to be appropriate to describe the disinfection rate constants. It was observed that the values k_{dis} varied within two orders of magnitude across all experiments. This is in keeping with the expectation that the rate constant should not vary significantly for the same organism. However, when the rate constant is examined as a function of concentration and light intensity, the variation is much greater at higher concentrations. At TiO_2 concentrations of 0.01 and 0.10 g L^{-1} the variation is within an order of magnitude. It is believed that these variations are related predominantly to colloidal interactions and the ratio of TiO_2 particles to cell numbers, both of which are explained in later sections.

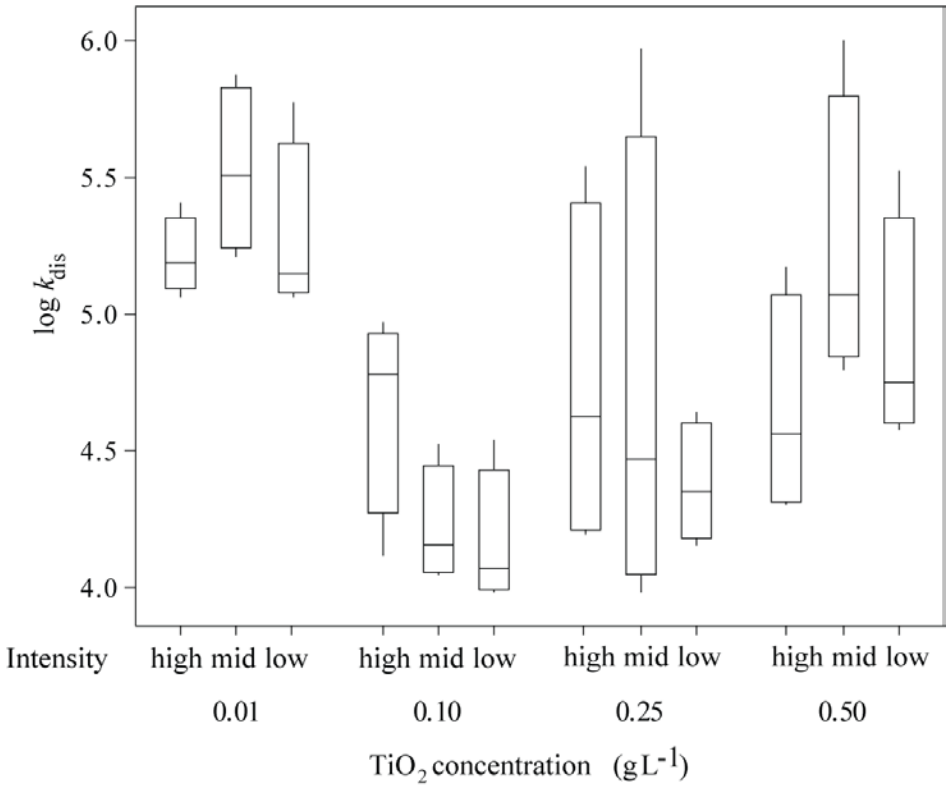

Figure 41: Box plot of the disinfection rate constant k_{dis} obtained from the model

The reaction order with respect to ·OH concentration also exhibited a small range of variability (1.4±0.1). In many chemical disinfection studies, the reaction order is usually assumed to be unity. However, the fact that the reaction order had to be greater than one to fit the data is not all that surprising. This is largely because there are numerous reactions of ·OH with biomolecules which eventually lead to cell inactivation. While ·OH may be the main oxidant, it does not preclude other radicals and oxidizing agents such as $O_2^{\cdot-}$ and H_2O_2 from participating in disinfection reactions. Hydroxyl radicals are short-lived even in pure buffered water because they undergo a recombination reaction to form hydrogen peroxide according to Equation (110). The second order hydroxyl radical recombination competes with slower first order reactions especially at higher doses when higher concentrations of hydroxyl radicals are produced.

$$2\,\cdot OH \rightarrow H_2O_2 \tag{110}$$

The formation of hydrogen peroxide also leads to the generation of other radicals, either through the reaction with ·OH or homolytic scission [50, 61]. The hydroxyl radical reacts with H_2O_2 at a relatively slower rate (2.7×10^7 mol^{-1} dm^3) and consumes only a small amount of the formed H_2O_2 [234],

$$\cdot OH + H_2O_2 \rightarrow HO_2^{\cdot}/O_2^{\cdot-} + H_2O \tag{111}$$

Even though the concentration of the superoxide radical is usually lower than the hydroxyl radical in solution, it has been shown that the former can contribute about 20% of the radical concentration [234].

8.4.2 Survival curve predictions

Under the given conditions, the model produces a sigmoidal survival curve when plotted on the linear axes in accordance with the typical inactivation behavior of *E. coli* (Figure 42). The initial lag and the onset of the log-linear phase for most of the disinfection data are well defined by the model (Figure 43). However, the greatest challenge seems to be replicating the latter end of the disinfection curves close to the limit of detection. There are a number of factors responsible for this deviation.

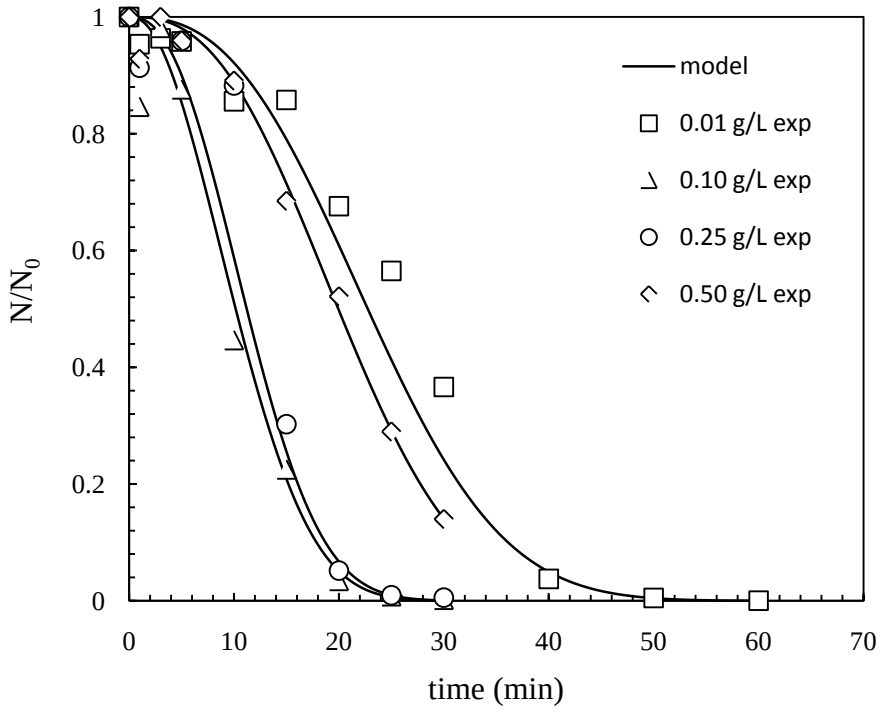

Figure 42: Typical sigmoidal survival of *E. coli* at low intensity illumination, N_0 = 1×10^6 CFU L^{-1}.

Firstly, an implicit assumption in the development of the model is that the disinfection process is deterministic. This assumption works well for molecules because their numbers are so incredibly high. However, it can be argued that disinfection begins

as a deterministic process when the number of microbes in solution is high (10^9 L^{-1}). This means that each microbe has about the same chance of being inactivated. However, as the microbial numbers drop significantly, it transitions to a stochastic process where the probability of inactivation varies from one organism to the next. The stochastic approach to model this behavior would be to define a function which accounts for the changing survival probabilities of individual cells [139]. The challenge, however, is that stochastic models are mostly empirical and cannot be obtained from deterministic formulations. Even though there may be mechanistic contributions to the probability function, such as uneven distribution of light, particularly in high concentration suspensions of TiO_2, it is still very difficult to formulate such a function and determine the influence of many other parameters as in the current model.

A second challenge, which occurs towards the end of the survival curve, is the determination of cell numbers close to the limit of detection. At very low concentrations, there is an inherent restriction on the number of cells which can appear on agar plates with sufficient accuracy to allow a resolution of the true cell count. In this study the lowest count that could be determined was 1 CFU per 100 μL (that is, 10 CFU mL^{-1}). This corresponds to 1 CFU on an agar plate with an associated relative error of 100%. The results indicate that there are significant fluctuations when determining cells at low concentration. The challenge for the model is that close to limit of detection, it predicts a uniform rate of disinfection. It is unlikely that this level of disinfection can be realized in a real population of cells or replicated in the lab.

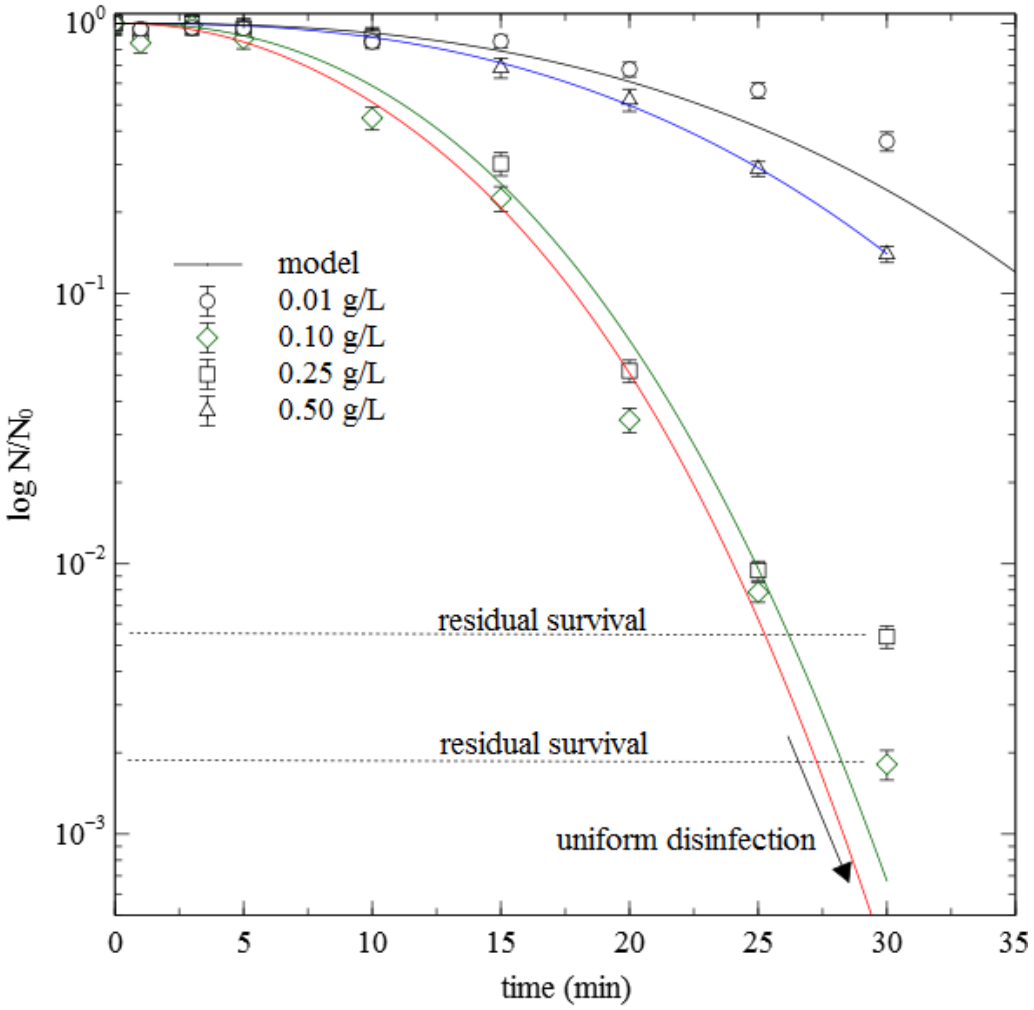

Figure 43: Survival curve for E. coli treated at low light intensity

Lastly, the existence of a finite residual survival, particularly for high catalyst concentration was observed. The residual survival is characterized by a sudden tailing off of the disinfection curve following the exponential decay (Figure 44). This was determined to be a real phenomenon because the cell count was usually to the right of the limit of detection. As previously explained, it is believed that the uneven distribution of

light in the high concentration suspensions reduces the exposure of cells in the irradiated fraction of the reactor. This is accompanied by a sharp reduction in the disinfection rate. Recall that for suspensions with less catalyst loading the irradiation zone is much wider, that is, the light distribution is more uniformed. As the cells are disinfected, the probability of entering the irradiated zone also drops, but not as much as in the case of high catalyst concentration. The consequence of this phenomenon is that disinfection is more "complete" in the case of lower concentrations, even if the overall process is slower (Figure 33).

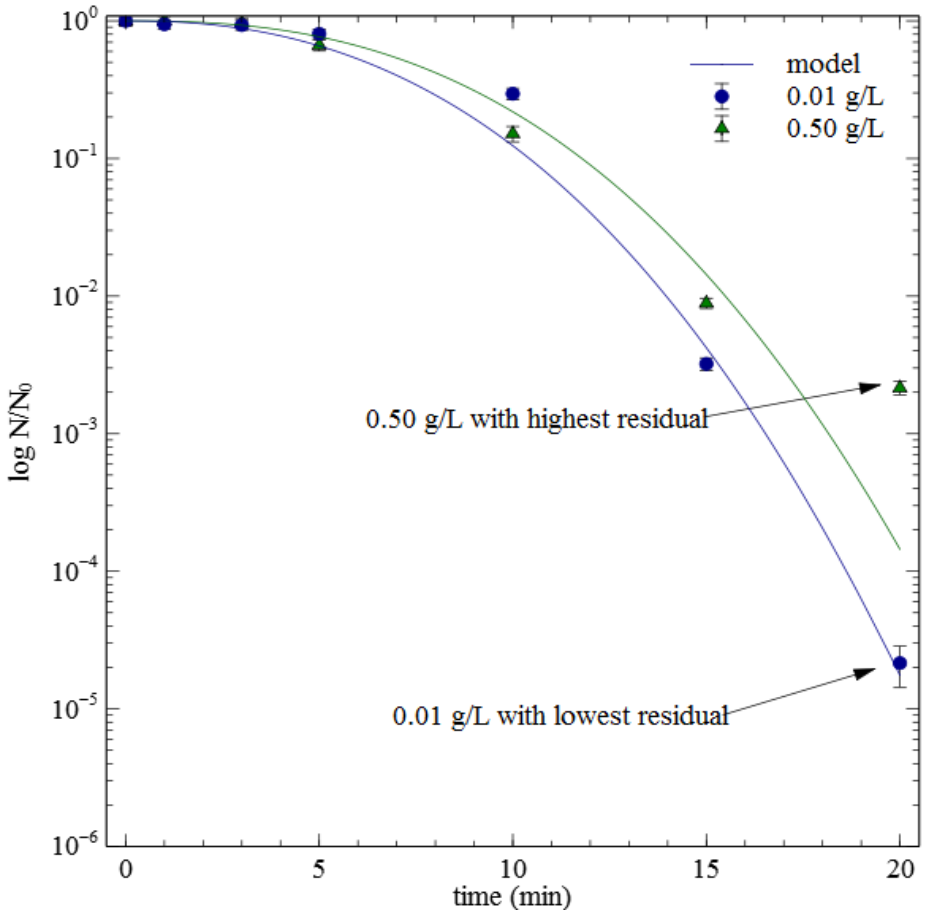

Figure 44: Effect of concentration loading on residual survival of *E. coli* at high light intensity

8.4.3 Influence of light intensity and catalyst concentration

The model captures the effect of light intensity and catalyst concentration on the disinfection very well. Without much change in the rate constants, it shows that the main effects are dominated by the interaction of these variables as determined previously. The processes involved in this interaction include light transmission, OH radical generation, and the absorption effects between colloids. Most of the variations from one survival curve to another are related to changes in light intensity and catalyst concentration, since other parameters were held constant.

8.5 Particle interaction effects and colloidal stability

Apart from the light absorption processes and chemical reactions involved in photocatalytic disinfection, the results indicate that the interaction of particles in the colloidal suspension has a very significant impact on the disinfection efficiency. These interactions are controlled by such factors as pH, ionic strength, particle size, and particle concentration. The interaction of TiO_2 particles and bacterial cells can be explained by DLVO and the soft-particle theory [125, 129, 235]. These theories provide the basis for explaining the effect of the above parameters on colloidal stability, and hence, on the photocatalytic disinfection process. Colloidal stability is here defined as the ability of the colloids to resist rapid aggregation and settling.

The total interaction energy of the particles in solution is given as the sum of the van der Waals and electrostatic interactions given in Equations (34) through (40). As can be observed from these relationships, the interaction depends on the surface potential of

the particles and the separation distance. The former is most commonly derived from electrophoretic studies, in which the electrophoretic mobility μ_e is related to the zeta potential (ζ-potential) at the particle surface through the Smoluchowski equation,

$$\zeta = \frac{\eta \mu_e}{\varepsilon_0 \varepsilon_r} \tag{112}$$

The ζ-potential is a theoretical approximation of the potential of the inner portion of the diffuse layer which is often used to characterize the stability of colloidal systems. It defines the electric potential close to the plane of shear (hydrodynamic slip plane) where the solvent molecules are not bound to the particle surface. The ions located in the region from this point toward the particle are assumed to move as a unit with the particle.

Using the electrophoretic data of Liu et al [236], Fernandez-Ibanez et al [149], and Suttiponparnit et al [237] it was possible to construct a graph (Figure 45) of the ζ-potential of TiO_2 as a function of pH and ionic strength. Similarly, the electrophoretic data for *E. coli* reported by Sonohara et al [115] based on the soft-particle theory [117] were used to calculate the ζ-potential at 0.01 M and 0.10 M ionic concentration as a function of pH.

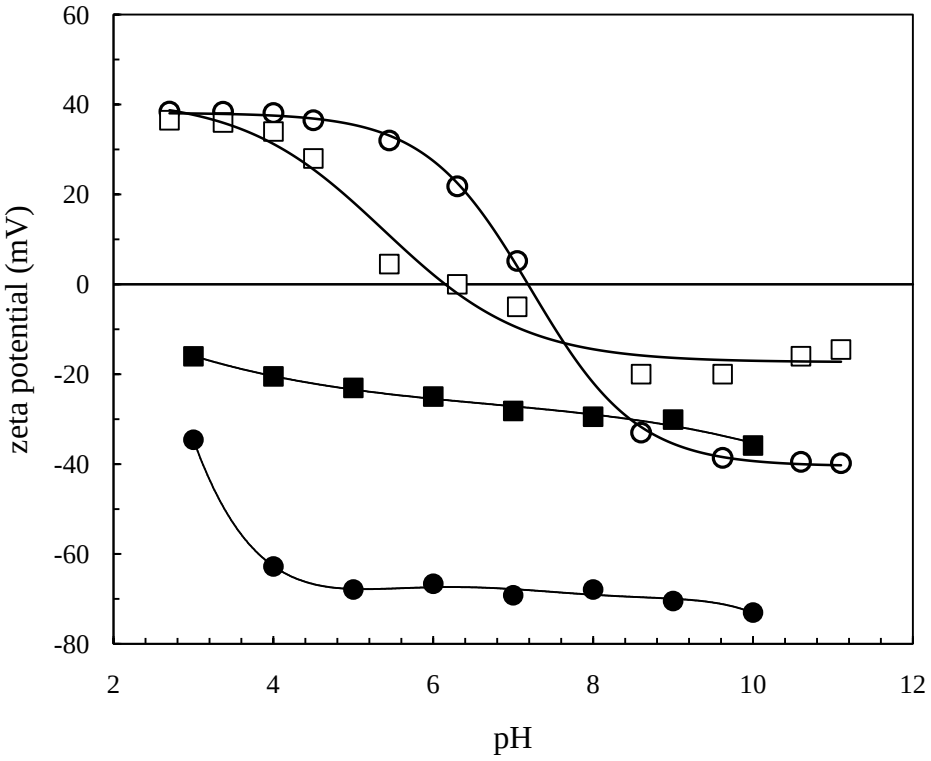

Figure 45: ζ-potential of P25 TiO_2 particles and *E. coli* cells as a function of pH in 0.01 M (open and filled circles) and 0.10 M (open and filled squares) ionic strength respectively. Data modified Liu et al [236], Fernandez-Ibanez et al [149], and Suttiponparnit et al [237].

8.5.1 Influence of ionic strength on disinfection

An analysis was performed to test the model for its response ionic strength. Two levels of ionic strength were investigated, 0.01 M and 0.2 M. The salt composition is reported in Table 5. Based on the experimental data, the overall disinfection process is significantly slowed by at least two orders of magnitude at the higher ionic strength (Figure 46). The constants obtained under the 0.01 M ionic strength analysis were used as inputs to the model to assess whether the increase in salt content alone could account for

the difference observed in the experiments. According to the model simulation there was no significant difference in disinfection at these two ionic strength levels.

A further theoretical simulation with an ionic strength of 20 M revealed that disinfection would be significantly reduced at this very high electrolyte concentration (Figure 47).

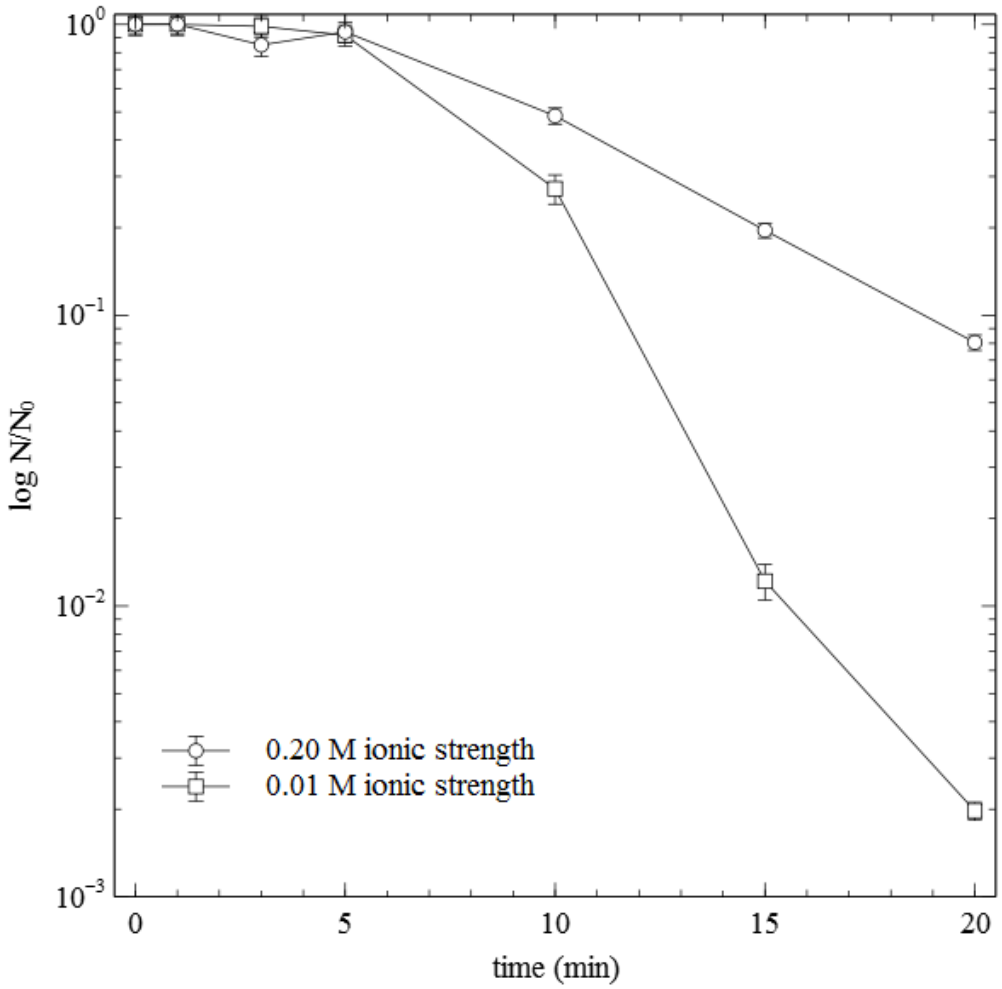

Figure 46: Influence of salt content on the disinfection process at pH 7 (light intensity = 2.4×10^{-5} E L^{-1} s^{-1}, TiO_2 = 0.50 g L^{-1})

As a second approach to modeling the effect of salt concentration on disinfection, the model was run without using the previously obtained kinetic constants for 0.01 M ionic strength. The newly obtained kinetic constants for the 0.20 M ionic strength were determined to be $k_{dis} = 1\times10^{-4}$ $pM^{-1.2}s^{-1}$ and $n = 1.2$. The results are shown in Figure 48. The differences between the disinfection rate constant for the two ionic strength solutions are attributed to colloidal stability effects.

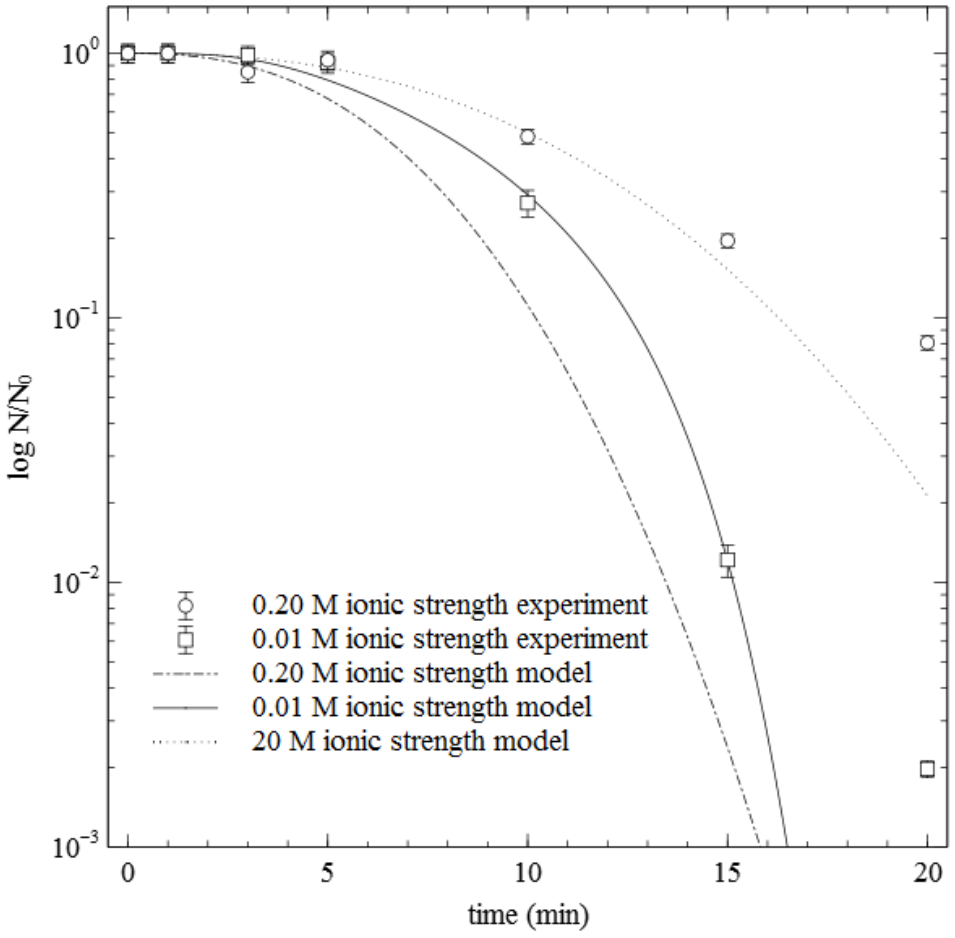

Figure 47: Model simulation of the effect of salt content with previously determined rate constants ($k_{dis} = 3.32x10^5$ $pM^{-1.5}s^{-1}$; $n = 1.5$; $k_{OH} = 1$ $L^{1.5}$ CFU^{-1} s^{-1} $pM^{0.5}$)

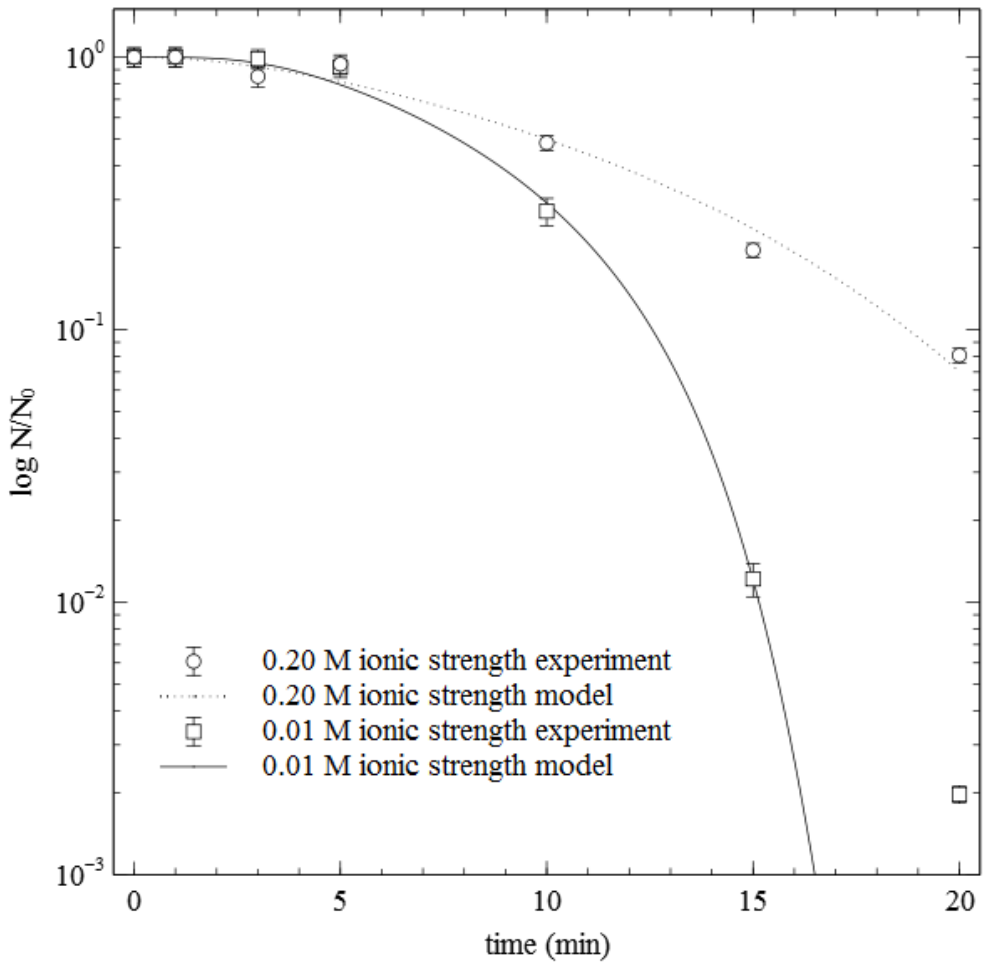

Figure 48: Simulated results for effect of salt concentration on disinfection (light intensity = 2.4×10^{-5} E L^{-1} s^{-1}, TiO_2 = 0.50 g L^{-1})

The effect of salt content in the model was built around a reduction in the generation rate through the blocking of OH sites as more electrolytes adsorb to the catalyst surface. However, the data suggests that colloidal stability is more sensitive to ionic strength than the blocking of OH sites. This is particularly true at neutral pH, where the adsorption of salts to the catalyst surface is not expected to be a significant factor since the TiO_2 surface has a very low charge.

However, visual observation of the TiO_2-microbe suspension shows that the colloids are unstable at salt concentrations exceeding 0.10 M; also confirmed experimentally by other researchers [84, 90, 92, 238]. The TiO_2 suspended in 0.10 M and 0.20 M ionic solutions flocculated and settled very rapidly, while the colloids remained dispersed in the 0.01 M ionic solution (Figure 49). This phenomenon is not currently captured in the model. The mechanisms through which colloidal destabilization reduces disinfection efficiency has not yet been studied. However, it is suspected that the increase in particle size reduces the rate at which OH radicals are generated.

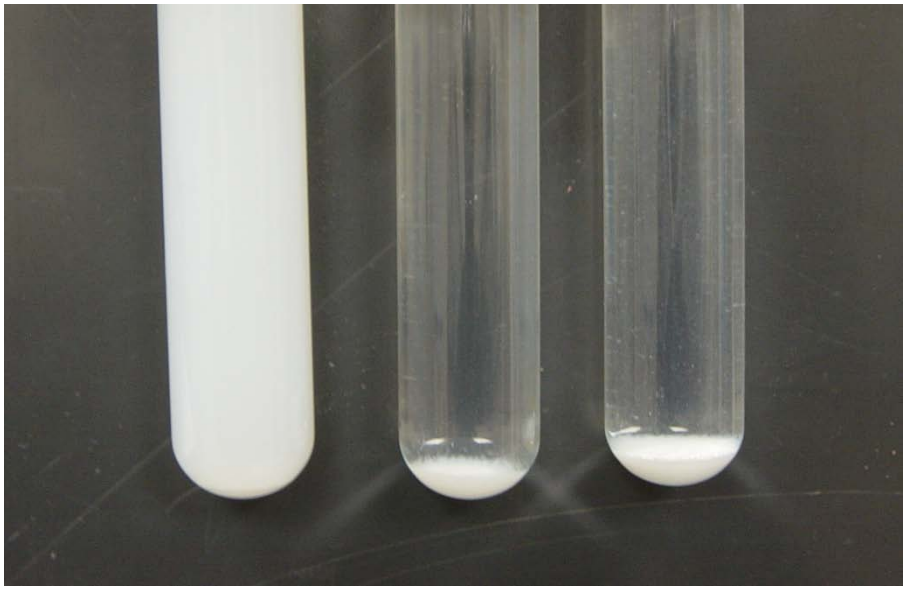

Figure 49: Settling of TiO_2-cell colloids (0.5 g L^{-1} and 1×10^6 CFU L^{-1} respectively) in 0.01 M (left), 0.10 M (center), and 0.20 M (right) ionic solutions at pH 7 and 25ºC.

The destabilizing effect of ionic strength on the TiO_2-cell suspension can be explained by considering the total interaction energy between the colloids at 0.01 and

0.10 M ionic strength (Figure 50). The interaction energy was calculated as a function of separation distance, according to Equation (34) for TiO_2 particles of 25 and 1000 nm and bacterial cells of 1000 nm diameter at pH 7. At the given pH, the surface charge of the catalyst is mostly neutral with less than 10% negative species. However, the cell surface is mostly negative at neutral pH. At a separation distance between 40 nm, the catalyst particles of 25 nm diameter begin to experience repulsion from the bacterial surface in the 0.01 M ionic solution. The strength of the repulsion rapidly increases as the catalyst particles get closer to the cell surface; as a result, the colloidal suspension is more stable. However, for larger TiO_2 particle, there is a primary minimum potential energy around 50 nm from the bacterial surface. At closer separation distances the large particles begin to experience repulsion.

In the 0.10 M ionic solution, the interaction energies are much lower. A 25 nm TiO_2 particle has virtually no energy barrier preventing it from adsorbing to the cell surface. A larger particle experiences a greater attraction with a primary minimum close to 10 nm from the surface. The low interaction energy and net attractive force creates the conditions for destabilizing the suspension and forces coagulation.

8.5.2 Influence of pH

The influence of pH on the disinfection process was simulated by the model and is illustrated in Figure 51. The simulation confirms the finding of other authors who studied the effect of pH on *E. coli* disinfection [27, 55, 160, 239]. It shows that in the pH range of 6-8 the disinfection rate is very similar. Simulations of lower and higher pH

were also conducted, but those results cannot be interpreted, since the influence of pH on natural survival of *E. coli* is not included in the model.

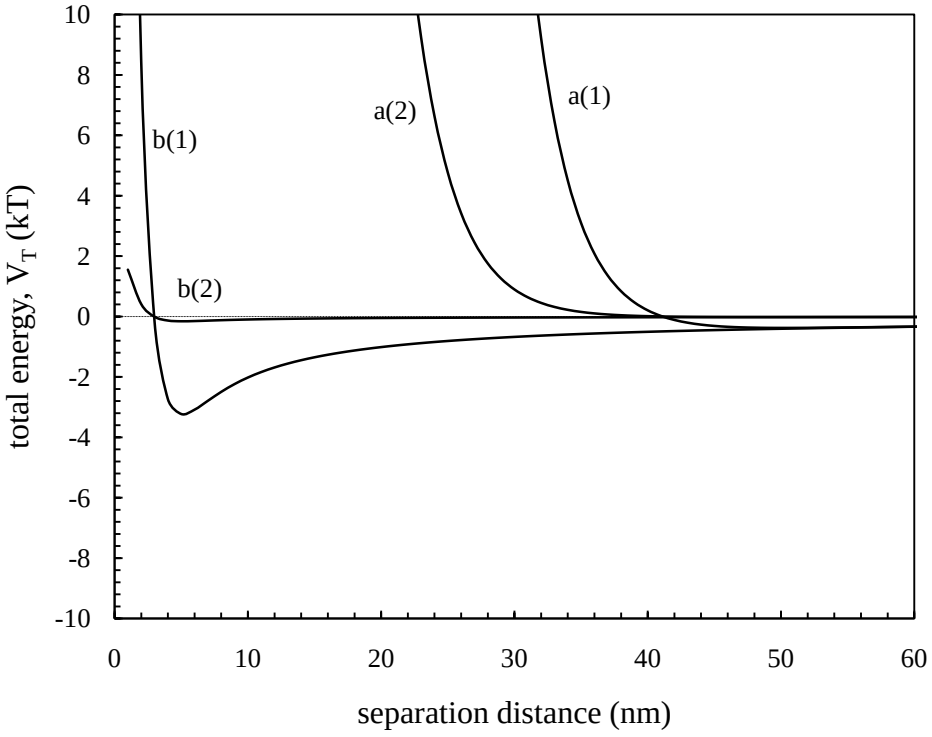

Figure 50: Total interaction energy (V_T) as a function of separation distance between *E. coli* (1000 nm dia.) and P25 TiO_2 at pH 7 and 25ºC: a(1) 0.01 M TiO_2 1000 nm dia.; a(2) 0.01 M TiO_2 25 nm dia.; b(1) 0.10 M TiO_2 1000 nm dia.; b(2) 0.10 M TiO_2 25 nm dia.

It is common knowledge that *E. coli* survives best within the pH range of 5-8, and is affected by low and high pH values. The model only accounts for changes in the catalyst surface chemistry and the effect of pH on absorption of anions. Apart from the ability of *E. coli* to thrive in neutral solutions, the isoeletric point of TiO_2 also occurs within this pH range.

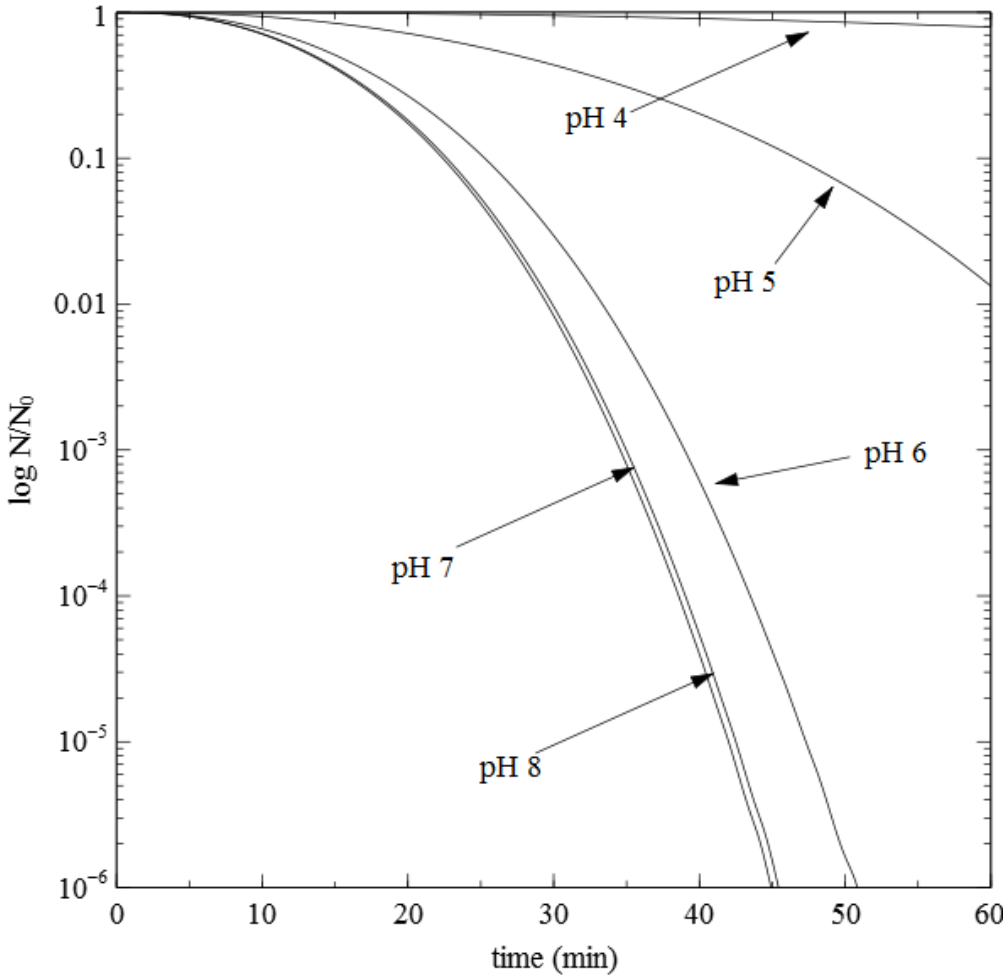

Figure 51: The effect of pH simulated by the model (unmodified cells treated at mid light intensity with 0.01 g L^{-1} TiO_2)

However, if the natural survival of the organism was ignored below pH 5, the process would be significantly retarded due to increase in the adsorption of anionic species. At higher pH values this effect would become negligible. The model does not include the effects of cations, which may influence the process at higher pH values.

From a colloidal stability perspective, it was found that pH has less of a destabilizing effect and slower coagulation kinetics than ionic strength. Settling

experiments were conducted at pH 3, 7 and 11 for TiO_2-cell suspensions. There instantaneous formation of large visible aggregates observed in solutions of ionic strength greater than 0.10 M was not observed for all pH values. However, after several hours (18-24 hrs), the colloids in solutions of pH 3 and 11 settled out completely almost complete, whereas the colloids suspended at neutral pH were still stable.

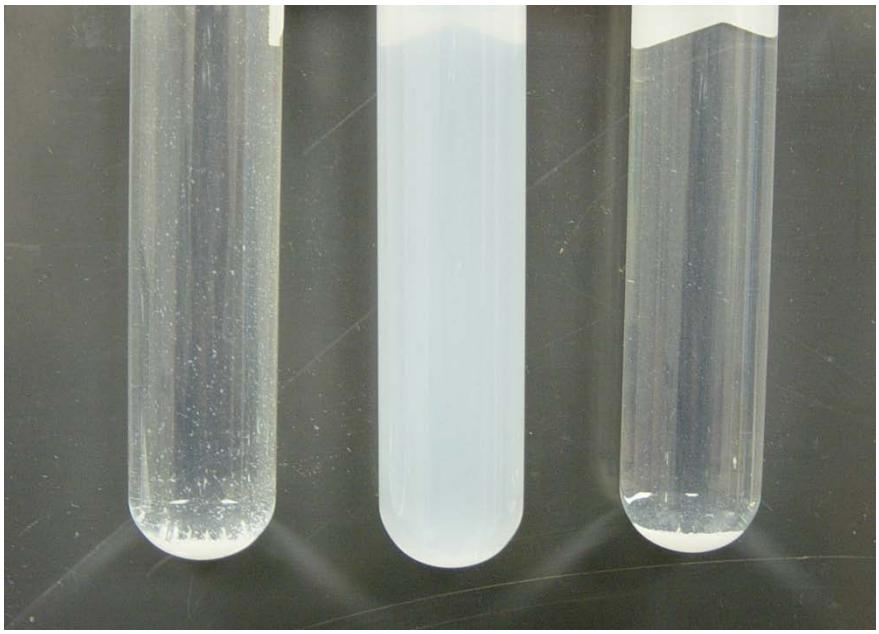

Figure 52: Long-term (24 hrs) settling of TiO_2-cell colloids in solutions of pH 3 (left), pH 7 (center), and pH 11 (right)

The interaction energy simulated from DLVO could not account for the destabilization at high pH, largely because the cells do not survive in such basic solutions. In the strictest theoretical sense, the solution should be stable at high pH because both the catalyst and cells are negatively charge. However, when the cells die, the ability to maintain osmotic balance with the solution is lost and the charges at the cell surface may induce conformations that allow the colloids to destabilize.

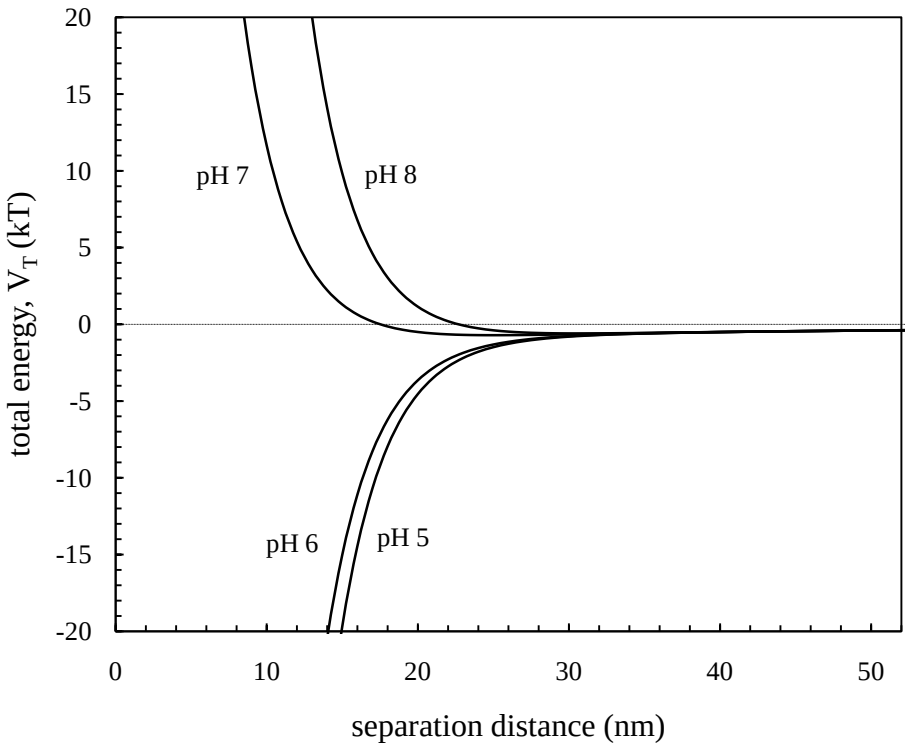

Figure 53: Total interaction energy (V_T) as a function of separation distance between *E. coli* (1000 nm dia.) and P25 TiO_2 (1000 nm dia.) at different pH values

8.6 Byproduct evolution and peroxidation kinetics

8.6.1 Lipid peroxidation as proof of membrane damage

In previous studies of photocatalytic disinfection, lipid peroxidation was used as an index to confirm the effects of OH radicals on cellular membranes during photocatalysis [20, 184]. In these studies the oxidation of PE in homogenous solution was compared to the disinfection of cells. However, while this approach yielded useful information about byproduct formation, they did not offer much information on the kinetics of cell membrane oxidation. Another consideration is that pure PE solutions or mixtures enriched in PE are notable for being unstable and adopt a hexagonal phase [240,

241]. They do not spontaneously form lamellar phases in aqueous media as do other phospholipids. They often require a stabilizing agent to maintain a bilayer structure similar to biological membranes.

In order to justify the use of peroxidation kinetics and rate constants in the model, lipid vesicles were used as model *E. coli* membranes. Lipid vesicles of PE were prepared with the addition of PG, which served as a stabilizing agent, but also represented a more realistic and natural *E. coli* membrane. The vesicles were also sized to be comparable to real cells. Cells and vesicles were then exposed to illumination with TiO_2 and the evolution of MDA and LOOH was measured during the experiments to assess membrane peroxidation.

8.6.2 Lipid vesicle composition and size distribution

The average diameter of the lipid vesicles was approximately 0.5 μm (Figure 54). Even though the vesicles are not rod-shaped like *E. coli*, the results correspond well to the published data on the size of *E. coli* cells, which measure on average 0.5 μm by 1 μm [70]. The size and shape of the vesicles were confirmed with TEM images as shown in Figure 55. The size distribution of the vesicles was important to establish the precise kinetic behavior of the system. The interaction of the particles (photocatalyst and cell) is based on particle size.

The very distinct darkened outline on the features in Figure 55 indicates that these were most likely multilamellar vesicles. Due to the nature of the TEM sample preparation, many of the vesicles seen in the figure were the very large vesicles which

settled out unto the TEM grid. The fatty acid composition of the vesicles was estimated from the manufacturer's data and is shown in Table 7. The predominant unsaturated fatty acid was *cis*-vaccenic acid (C18:1 n-7) in PE and oleic acid (C18:1 n-9) in PG.

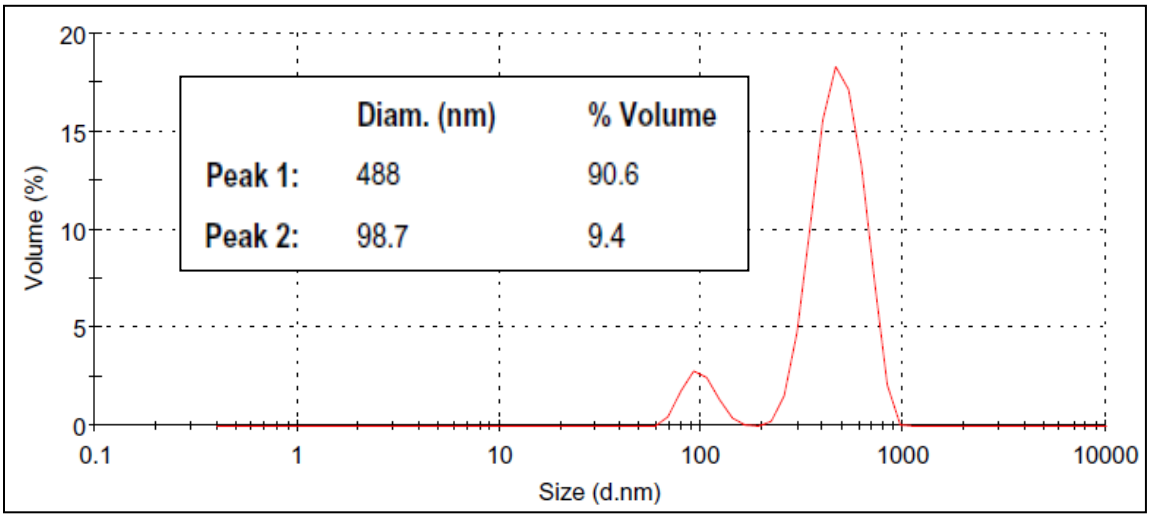

Figure 54: Size distribution by volume based on photon correlation spectroscopy of the lipids vesicles in 1×PBS solution (molar ratio 1:1 PE to PG)

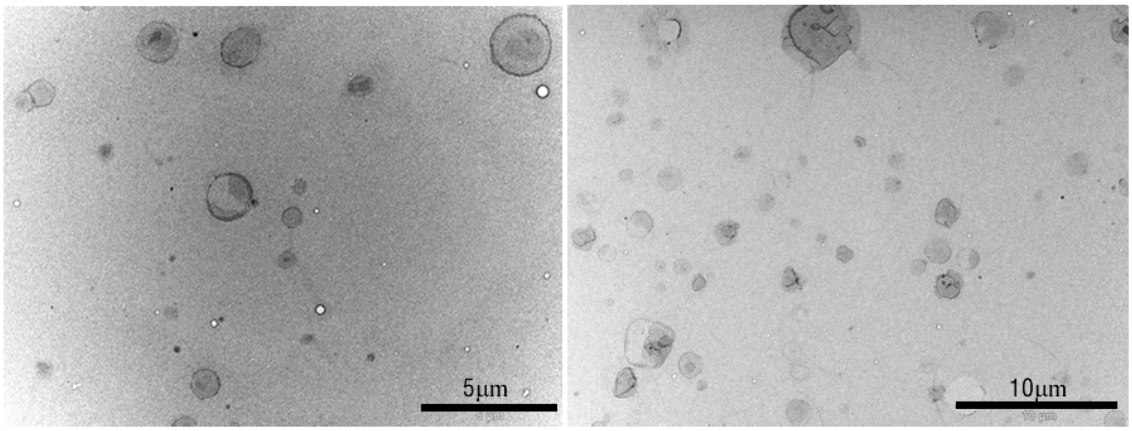

Figure 55: TEM images of PE/PG lipid vesicles. Images courtesy of Integrative Biology Microscopy Core Facility, University of South Florida

8.6.3 MDA production during photocatalytic experiments

MDA was detected in photocatalytic experiments containing 10^{11} CFU L^{-1} in order to increase the levels of MDA detection. Even though the MDA test has some limitations, the evolution of MDA in all the samples was very similar and consistent between experiments. The monotonic accumulation of MDA was observed during the first 20-30 minutes of the photocatalytic experiments for both unmodified *E. coli* cells and lipid vesicles. Thereafter, a steady decrease in concentration was recorded (Figure 56). There was a prolonged increase in MDA for the cells modified with linolenic acid. The overall trend for MDA release during photocatalysis was first observed by Maness *et al* [20] for the disinfection of *E. coli* cells under similar conditions. The trend appears to be consistent with the peroxidation of membrane lipids followed by the degradation of MDA (either naturally or photocatalytically). More MDA was produced in the vesicles because they were composed only of fatty acids, whereas cells have their fatty acids distributed in the membrane with other biological structures such as proteins.

A common criticism of the TBA assay is that MDA is produced by artifactual means during the harsh processing conditions of the test [187, 210, 213, 242, 243]. However, the use of BHT antioxidant in the test serves to eliminate or reduce the production of MDA during the processing of the sample [242]. In addition, the conditions of these tests were much milder compared to the more traditional TBA tests which utilize boiling temperatures to facilitate the reaction with MDA. The most convincing evidence of all is the fact that no measureable MDA concentrations were detected in any of the

control experiments (data not shown), leading to the conclusion that the observed trend resulted from treating the cells and vesicles photocatalytically.

The TBA test is the most frequently used method to detect lipid peroxidation, but it has also been criticized for its non-specificity, particularly in complex biological systems. However, it has proven useful in well defined systems such as the oxidation of lipid vesicles [209, 244]. Hence, when the time characteristic for MDA evolution during oxidation of the model membranes is compared to real cells, there is strong evidence that the trend observed in cells resulted from membrane peroxidation. In addition, the byproduct evolution simulated by the model is a close match to the observed data (Figure 57). However, this simulation could possibly include other byproducts apart from MDA.

8.6.4 Effect of supplemental fatty acid on MDA production in cells

For the cells modified with α-linolenic acid, it was found that MDA accumulation rate was relatively slow compared to the other cells and vesicles (Figure 56). There was a gradual increase which peaked around 45 minutes. Control cells and cells supplemented with oleic acid (C18:1 n-9) did not produce this extended MDA evolution curve, which leads to the belief that the kinetics is affected by the fatty acid composition. However, it is difficult to make a definitive conclusion about the impact of the fatty acid supplementation on MDA production because of the complexity of the system and the undefined sink processes for MDA.

Nonetheless, it is generally expected that increases in polyunsaturated fatty acid content would render the cell more sensitive to oxidation and an increase in the MDA production could be possible. Other studies have shown that the oxidizability of cells can be altered by supplementation with external fatty acids [208, 231, 245]. The results in this case seem to suggest that the enriching of the membrane with monounsaturated fatty acids retards the rate of MDA production, particularly when supplemented with α-linolenic acid. The actual mechanism by which these monosaturated fatty acids are able to reduce the peroxidation rate is still not clear. However, a possible explanation for this observation is the oxidation of monosaturated fatty acids does not produce bioactive byproducts responsible for enhancing membrane peroxidation [231, 246]. This effect, described by Lee et al [231], is similar to an antioxidant in which the monosaturated fatty acids serve as a temporary sink for the capture of free radicals, and retard propagation due to their reduced reactivity.

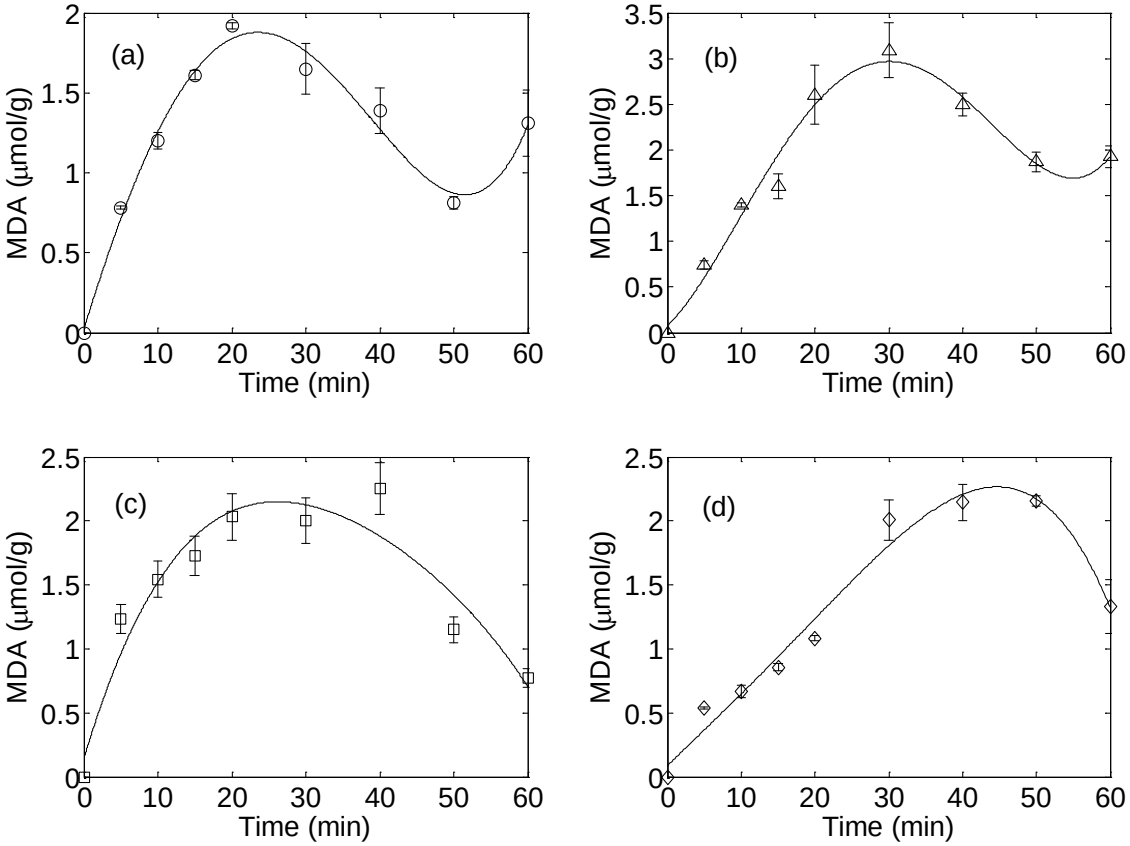

Figure 56: MDA production during photocatalytic experiments with P25 TiO2: I_0 = 4.85×10^{-5} E $L^{-1}s^{-1}$, $N_0 \approx 2.8\times10^{11}$ CFU L^{-1}: (a) unmodified cells; (b) *E. coli* PE/PG vesicles; (c) cells supplemented with oleic acid; (d) cells supplemented with linolenic acid. The data are fitted with a fourth order polynomial

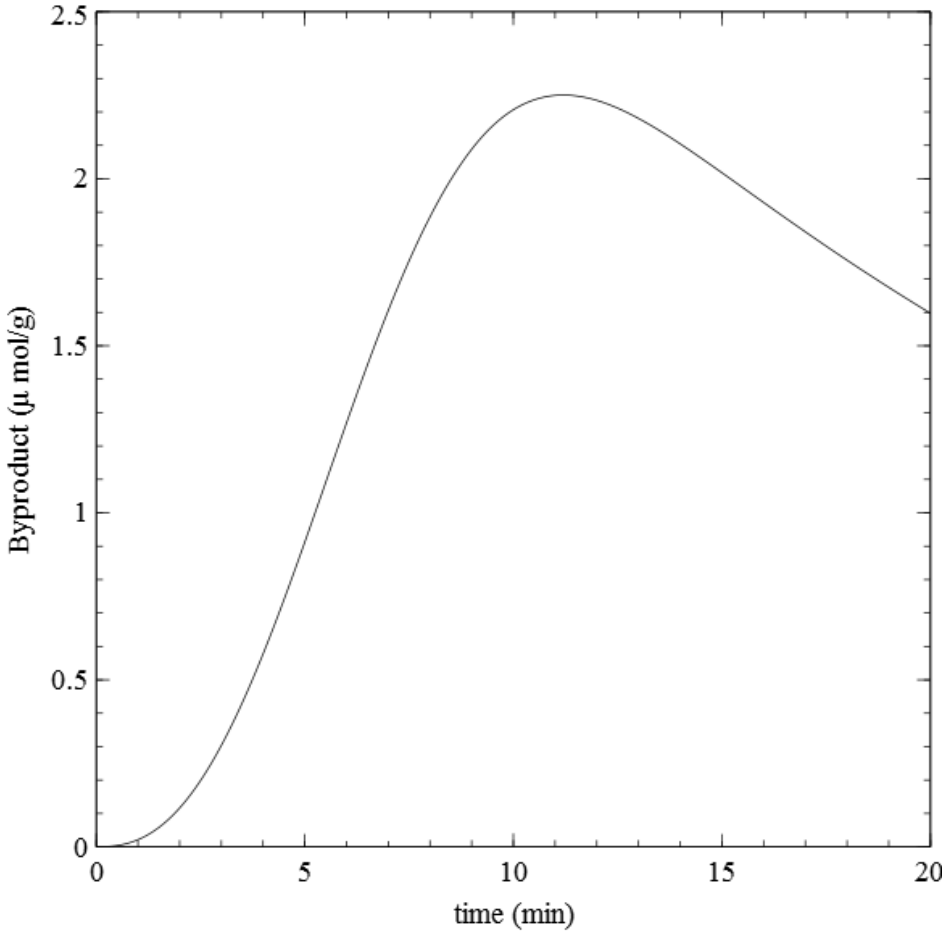

Figure 57: Typical curve for the simulation of byproducts from the model

8.6.5 Correlation between peroxidation and disinfection

From the analysis of main effects of fatty acid modification, it was found that there were no significant differences between the organisms. This suggests that while peroxidation is an important process for disinfection, it is not the sole process. It is very likely that oxidation of proteins and other biomolecules are just as important in the process [247]. Polyunsaturated fatty acids are usually very sensitive to oxidation. However, they were not present in significant proportions in *E. coli*. The MDA produced in these studies could result from both fatty acids and other cellular constituents.

8.6.6 LOOH production during disinfection

The illumination of TiO_2 in the presence of *E. coli* cells and lipid vesicles yielded measurable concentrations of hydroperoxides (Figure 58). The nature of the LOOH test ensures that only peroxide generated from the cells is measured. The kit uses a number of internal controls, which correct for endogenous iron content and possible hydrogen peroxide. A significant increase in LOOH concentration was observed during the early stages of the experiments. There was an apparent decrease in the hydroperoxide content at longer illumination times. As in the case of MDA, this trend indicates that the resulting kinetics is a consequence of both photocatalytically-induced formation and decomposition of hydroperoxides. This is consistent with the concomitant generation of MDA during the experiments.

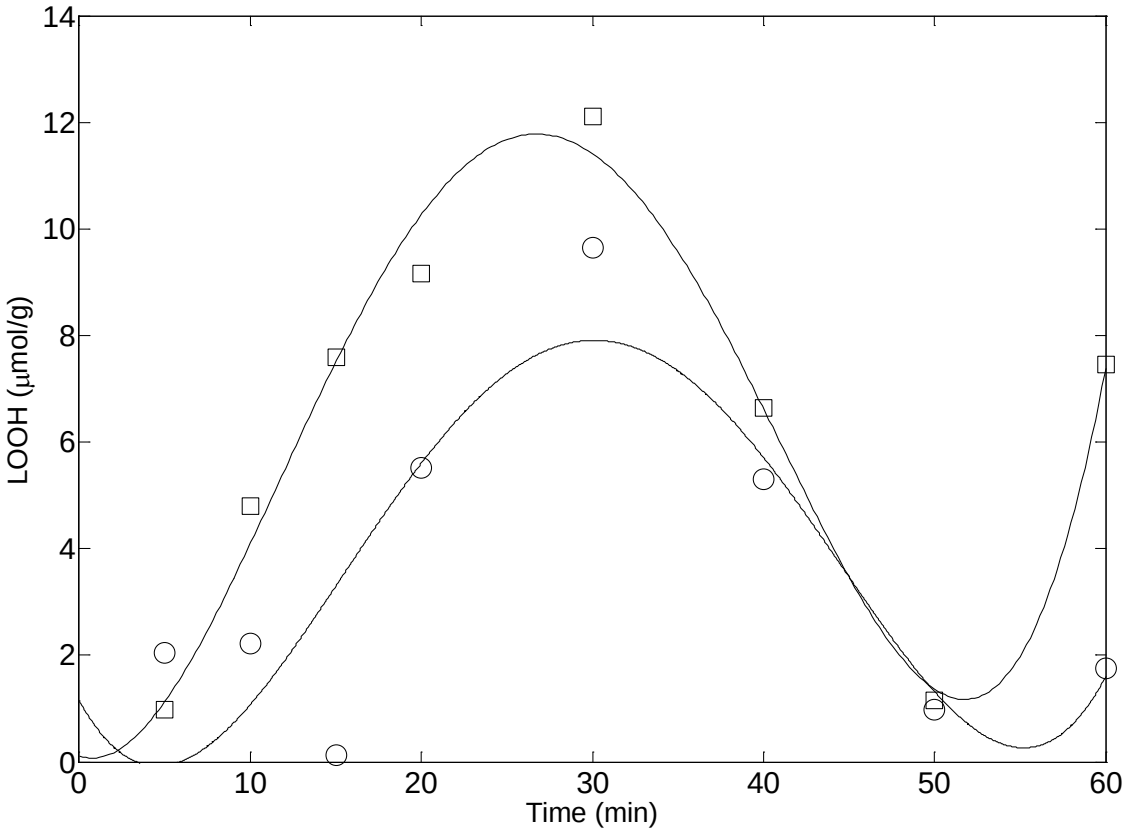

Figure 58: Time characteristics of lipid hydroperoxide detection during photocatalytic treatment: (○) *E. coli* cells; (□) vesicles prepared with *E. coli* phospholipids

CHAPTER 9: CONCLUSIONS

The photocatalytic disinfection of *E. coli* with suspended catalyst particles is a complex process that involves the interplay of many phenomena. These include light absorption and scattering, semiconductor photo-excitation and charge carrier generation, electrochemical surface reactions (including electron transfer reactions, adsorption, and acid-base reactions), and heterogeneous colloidal interactions. All these processes play a significant role in the overall inactivation efficiency. For a given solution composition, light intensity and catalyst concentration are the most significant operational factors in the entire process. The combination of light intensity and catalyst concentration determine the light absorption and scattering effects and the OH radical generation rate. Low catalyst concentration and high light intensity favor higher log inactivation. At low TiO_2 concentrations, the colloidal suspension is more stable, the distribution of light is fairly uniform, and there is a higher radical generation rate per mass of catalyst.

The mechanistic model developed in the study is very comprehensive. Apart from light intensity and catalyst concentration, it has the potential to predict the effect of pH and ionic strength on the disinfection process. However, these predictions are confined to stable suspensions. The disinfection efficiency is significantly reduced in destabilized suspensions which occur at high ionic strength, excessive particle concentration concentrations, and extreme pH.

It was found that the evolution of byproducts is consistent with the oxidation of cell membranes. MDA and LOOH were detected when *E. coli* cells and model cell membranes were exposed to photocatalytic action. Not only were the byproducts similar, but the time evolution showed very similar trends. However, no statistically significant effect could be observed by modifying the fatty acid profile of the cells. This is attributed to the fact that other biomolecules such as proteins are more abundant than polyunsaturated fatty acids and also react at high rates with the OH radical. Therefore, it can be concluded that even though peroxidation of the membrane is an important process in disinfection of *E. coli*, the fatty acid distribution was not sufficiently altered to observe any changes to the overall disinfection kinetics.

Finally, the model is flexible and has good validity for predicting the disinfection behavior of *E. coli*. The reaction rate parameters are within reasonable range and exhibit only small variability, especially at low catalyst concentrations. The reaction rate order with respect to the OH radical was found to be greater than unity. However, there is an inherent challenge to replicate residual survival, especially at low cell concentration because of the deterministic nature of the model. The model predicts uniform inactivation close to and beyond the limit of detection, which is not always the case. The high fluctuations of bacteria at low concentrations make this challenge very difficult to solve. One technique would be to utilize stochastic models which can define the probability of disinfecting an individual organism based on the reaction composition.

CHAPTER 10: RECOMMENDATIONS

The proposed model can be exploited for modeling bacterial survival notwithstanding the challenges. However, this is the first formulation of such a comprehensive model for photocatalytic disinfection. Naturally, many experimental research problems still exist and require attention. The most important would appear to be:

- experimental determination of the adsorption phenomena of TiO_2 catalyst particles to bacteria under varying conditions of pH and catalyst concentration

- developing a stochastic model with a mechanistic basis for disinfection, particularly for treatment of solutions containing a low concentration of cells

- testing the model for disinfection under flow conditions, particularly under solar conditions

- including the effects of salt concentration on double layer effects

REFERENCES

1. WHO, *Combating waterborne disease at the household level*. 2007, World Health Organization: Geneva.

2. United Nations, *Water for People, Water for Life: United Nations World Water Development Report*. UNESCO and Bergham Books, Barcelona, 2003.

3. J. Lonnen, S. Kilvington, S.C. Kehoe, F. Al-Touati, and K.G. McGuigan, Solar and photocatalytic disinfection of protozoan, fungal and bacterial microbes in drinking water, *Water Res.* 39 (2005) 877-883.

4. E.F. Duffy, F. Al Touati, S.C. Kehoe, O.A. McLoughlin, L.W. Gill, W. Gernjak, et al., A novel TiO_2-assisted solar photocatalytic batch-process disinfection reactor for the treatment of biological and chemical contaminants in domestic drinking water in developing countries, *Solar Energy*. 77 (2004) 649-655.

5. F. Méndez-Hermida, E. Ares-Mazás, K.G. McGuigan, M. Boyle, C. Sichel, and P. Fernández-Ibáñez, Disinfection of drinking water contaminated with *Cryptosporidium parvum* oocysts under natural sunlight and using the photocatalyst TiO_2, *J. Photochem. Photobiol. B.* 88 (2007) 105-111.

6. G.C. White, *The Handbook of Chlorination*. 2nd ed., Von Nostrand Reinhold, New York, 1986.

7. M.J. Nieuwenhuijsen, M.B. Toledano, N.E. Eaton, J. Fawell, and P. Elliott, Chlorination disinfection byproducts in water and their association with adverse reproductive outcomes: a review, *Occup. Environ. Med.* 57 (2000) 73-85.

8. E.A. Bryant, G.P. Fulton, and G.C. Budd, *Disinfection Alternatives for Safe Drinking Water*. Environmental Engineering Series. van Nostrand Reinhold, New York, 1992.

9. *Safe Drinking Water Act Amendments of 1996*, in *P.L. 104-182*. 1996. p. 1620-1621.

10. E.W. Rice, J.C. Hoff, and F.W. Schaefer, III, Inactivation of Giardia cysts by chlorine, *Appl. Environ. Microbiol.* 43 (1982) 250-251.

11. W.Q. Betancourt and J.B. Rose, Drinking water treatment processes for removal of Cryptosporidium and Giardia, *Veterinary Parasitology*. 126 (2004) 219-234.

12. S.D. Richardson, A.D. Thruston, T.V. Caughran, P.H. Chen, T.W. Collette, T.L. Floyd, et al., Identification of new ozone disinfection byproducts in drinking water, *Environ. Sci. Technol.* 33 (1999) 3368-3377.

13. S.D. Richardson, A.D. Thruston, T.V. Caughran, P.H. Chen, T.W. Collette, T.L. Floyd, et al., Identification of new drinking water disinfection byproducts formed in the presence of bromide, *Environ. Sci. Technol.* 33 (1999) 3378-3383.

14. C. Srinivasan and N. Somasundaram, Bactericidal and detoxification effects of irradiated semiconductor catalyst, TiO_2, *Curr. Sci.* 85 (2003) 1431-1438.

15. C. McCullagh, J.M.C. Robertson, D.W. Bahnemann, and P.K.J. Robertson, The application of TiO_2 photocatalysis for disinfection of water contaminated with pathogenic micro-organisms: a review, *Research on Chemical Intermediates*. 33 (2007) 359-375.

16. D. Bahnemann, Photocatalytic water treatment: solar energy applications, *Solar Energy*. 77 (2004) 445-459.

17. D.Y. Goswami, A review of engineering developments of aqueous phase solar photocatalytic detoxification and disinfection processes, *J. Sol. Energy Eng.* 119 (1997) 101-107.

18. S. Malato, P. Fernández-Ibáñez, M.I. Maldonado, J. Blanco, and W. Gernjak, Decontamination and disinfection of water by solar photocatalysis: Recent overview and trends, *Catal. Today*. 147 (2009) 1-59.

19. T. Matsunaga, R. Tomoda, T. Nakajima, and H. Wake, Photoelectrochemical sterilization of microbial cells by semiconductor powders, *FEMS Microbiol. Lett.* 29 (1985) 211-214.

20. P. Maness, S. Smolinski, D.M. Blake, Z. Huang, E.J. Wolfrum, and W.A. Jacoby, Bactericidal activity of photocatalytic TiO_2 reaction: toward an understanding of its killing mechanism, *Appl. Environ. Microbiol.* 65 (1999) 4094-4098.

21. J. Marugán, R. van Grieken, C. Sordo, and C. Cruz, Kinetics of the photocatalytic disinfection of *Escherichia coli* suspensions, *Appl. Catal. B.* 82 (2008) 27-36.

22. O.A. McLoughlin, P.F. Ibanez, W. Gernjak, S.M. Rodri'guez, and L.W. Gill, Photocatalytic disinfection of water using low cost compound parabolic collectors, *Solar Energy*. 77 (2004) 625-633.

23. A.G. Rincon and C. Pulgarin, Photocatalytical inactivation of *E. coli*: effect of (continuous-intermittent) light intensity and of (suspended-fixed) TiO_2 concentration, *Appl. Catal. B.* 44 (2003) 263-284.

24. A.-G. Rincon and C. Pulgarin, Bactericidal action of illuminated TiO_2 on pure *Escherichia coli* and natural bacterial consortia: post-irradiation events in the dark and assessment of the effective disinfection time, *Appl. Catal. B.* 49 (2004) 99-112.

25. C.P. Rodrigues, R.L. Ziolli, and J.R. Guimarães, Inactivation of *Escherichia coli* in water by TiO_2-assisted disinfection using solar light, *J. Braz. Chem. Soc.* 18 (2007) 126-134.

26. K. Sunada, Y. Kikuchi, K. Hashimoto, and A. Fujishima, Bactericidal and detoxification effects of TiO_2 thin film photocatalysts, *Environ. Sci. Technol.* 32 (1998) 726-728.

27. R.J. Watts, S. Kong, M.P. Orr, G.C. Miller, and B.E. Henry, Photocatalytic inactivation of coliform bacteria and viruses in secondary wastewater effluent, *Water Res.* 29 (1995) 95-100.

28. C. Wei, W.Y. Lin, Z. Zainal, N.E. Williams, K. Zhu, A.P. Kruzic, et al., Bactericidal activity of TiO_2 photocatalyst in aqueous media: toward a solar-assisted water disinfection system, *Environ. Sci. Technol.* 28 (1994) 934-938.

29. Y.-S. Choi and B.-W. Kim, Photocatalytic disinfection of *E. coli* in a UV/TiO_2-immobilised optical-fibre reactor, *J. Chem. Technol. Biotechnol.* 75 (2000) 1145-1150.

30. M. Cho and J. Yoon, Measurement of OH radical CT for inactivating *Cryptosporidium parvum* using photo/ferrioxalate and photo/TiO_2 systems, *Appl. Microbiol.* 104 (2008) 759-766.

31. H. Ryu, D. Gerrity, J.C. Crittenden, and M. Abbaszadegan, Photocatalytic inactivation of *Cryptosporidium parvum* with TiO_2 and low-pressure ultraviolet irradiation, *Water Res.* 42 (2008) 1523-1530.

32. S. Navalon, M. Alvaro, H. Garcia, D. Escrig, and V. Costa, Photocatalytic water disinfection of *Cryptosporidium parvum* and *Giardia lamblia* using a fibrous ceramic TiO_2 photocatalyst, *Water Sci. Technol.* 59 (2009) 639-645.

33. A. Cooper, D.Y. Goswami, and S.S. Block, Solar photochemical detoxification and disinfection for water treatment in tropical developing countries, *J. Adv. Oxidation Technol.* 3 (1998) 151-154.

34. S.S. Block, V.P. Seng, and D.W. Goswami, Chemically enhanced sunlight for killing bacteria, *J. Sol. Energy Eng.* 119 (1997) 85-91.

35. D.Y. Goswami, *Engineering of Solar Photocatalytic Detoxification and Disinfection*, in: K.W. Böer (Ed.), Advances in Solar Energy, ASES, 1995, pp. 165-210.

36. D.Y. Goswami, S.K. Sharma, G.D. Mathur, and C.K. Jotshi, Techno-economic analysis of solar detoxification systems, *J. Sol. Energy Eng.* 119 (1997) 108-113.

37. S. Malato, J. Blanco, A. Vidal, and C. Richter, Photocatalysis with solar energy at a pilot-plant scale: an overview, *Appl. Catal. B.* 37 (2002) 1-15.

38. S. Malato, J. Blanco, A. Vidal, P. Fernandez, J. Caceres, P. Trincado, et al., New large solar photocatalytic plant: set-up and preliminary results, *Chemosphere*. 47 (2002) 235-240.

39. Q. Li, R. Xie, Y.W. Li, E.A. Mintz, and J.K. Shang, Enhanced visible-light-induced photocatalytic disinfection of *E. coli* by carbon-sensitized nitrogen-doped titanium oxide, *Environ. Sci. Technol.* 41 (2007) 5050-5056.

40. M.S. Wong, W.C. Chu, D.S. Sun, H.S. Huang, J.H. Chen, P.J. Tsai, et al., Visible-light-induced bactericidal activity of a nitrogen-doped titanium photocatalyst against human pathogens, *Appl. Environ. Microbiol.* 72 (2006) 6111-6116.

41. J.A. Rengifo-Herrera, E. Mielczarski, J. Mielczarski, N.C. Castillo, J. Kiwi, and C. Pulgarin, *Escherichia coli* inactivation by N, S co-doped commercial TiO_2 powders under UV and visible light, *Appl. Catal. B.* 84 (2008) 448-456.

42. L. Caballero, K.A. Whitehead, N.S. Allen, and J. Verran, Inactivation of *Escherichia coli* on immobilized TiO_2 using fluorescent light, *J. Photochem. Photobiol. A.* 202 (2009) 92-98.

43. P. Wu, R. Xie, J.A. Imlay, and J.K. Shang, Visible-light-induced photocatalytic inactivation of bacteria by composite photocatalysts of palladium oxide and nitrogen-doped titanium oxide, *Appl. Catal. B.* 88 (2009) 576-581.

44. J.C. Yu, W. Ho, J. Yu, H. Yip, P.K. Wong, and J. Zhao, Efficient visible-light-induced photocatalytic disinfection on sulfur-doped nanocrystalline titania, *Environmental Science & Technology*. 39 (2005) 1175-1179.

45. C. Karunakaran, G. Abiramasundari, P. Gomathisankar, G. Manikandan, and V. Anandi, Cu-doped TiO_2 nanoparticles for photocatalytic disinfection of bacteria under visible light, *J. Colloid Interface Sci.* 352 (2010) 68-74.

46. O.K. Dalrymple, E. Stefanakos, M.A. Trotz, and D.Y. Goswami, A review of the mechanisms and modeling of photocatalytic disinfection, *Appl. Catal. B.* 98 (2010) 27-38.

47. N. Serpone and A.V. Emeline, Suggested terms and definitions in photocatalysis and radiocatalysis, *International Journal of Photoenergy*. 4 (2002) 91-131.

48. A. Mills and S. Le Hunte, An overview of semiconductor photocatalysis, *J. Photochem. Photobiol. A.* 108 (1997) 1-35.

49. R. Memming, *Semiconductor Electrochemistry*. Weinheim: Wiley-VCH, 2001.

50. M.R. Hoffmann, S.T. Martin, W. Choi, and D.W. Bahnemann, Environmental applications of semiconductor photocatalysis, *Chem. Rev.* 95 (1995) 69-96.

51. A. Wold, Photocatalytic properties of titanium dioxide (TiO2), *Chem. Mater.* 5 (1993) 280-283.

52. M. Ni, M.K.H. Leung, D.Y.C. Leung, and K. Sumathy, A review and recent developments in photocatalytic water-splitting using TiO_2 for hydrogen production, *Renewable and Sustainable Energy Reviews*. 11 (2007) 401-425.

53. S.-D. Mo and W.Y. Ching, Electronic and optical properties of three phases of titanium dioxide: Rutile, anatase, and brookite, *Physical Review B.* 51 (1995) 13023.

54. D. Reyes-Coronado, G. Rodriguez-Gattorno, M.E. Espinosa-Pesqueira, C. Cab, R.d. Coss, and G. Oskam, Phase-pure TiO_2 nanoparticles: anatase, brookite and rutile, *Nanotechnology*, (2008) 145605.

55. D. Gumy, C. Morais, P. Bowen, C. Pulgarin, S. Giraldo, R. Hajdu, et al., Catalytic activity of commercial of TiO_2 powders for the abatement of the bacteria (*E. coli*) under solar simulated light: Influence of the isoelectric point, *Appl. Catal. B.* 63 (2006) 76-84.

56. C. Di Valentin, G. Pacchioni, and A. Selloni, Electronic structure of defect states in hydroxylated and reduced rutile TiO_2(110) surfaces, *Phys. Rev. Lett.* 97 (2006) 166803-4.

57. N. Daude, C. Gout, and C. Jouanin, Electronic band structure of titanium dioxide, *Physical Review B.* 15 (1977) 3229.

58. D.S. Bhatkhande, V.G. Pangarkar, and A.A.C.M. Beenackers, Photocatalytic degradation for environmental applications - a review, *J. Chem. Technol. Biotechnol.* 77 (2002) 102-116.

59. S.Y. Chae, M.K. Park, S.K. Lee, T.Y. Kim, S.K. Kim, and W.I. Lee, Preparation of Size-Controlled TiO_2 Nanoparticles and Derivation of Optically Transparent Photocatalytic Films, *Chem. Mater.* 15 (2003) 3326-3331.

60. M. Gratzel, Photoelectrochemical cells, *Nature*. 414 (2001) 338-344.

61. J.-M. Herrmann, Heterogeneous photocatalysis: fundamentals and applications to the removal of various types of aqueous pollutants, *Catal. Today*. 53 (1999) 115-129.

62. N. Serpone and E. Pelizzetti, *Photocatalysis: Fundamentals and Applications*. John Wiley & Sons, Inc., New York, 1989.

63. C.C. Wong and W. Chu, The hydrogen peroxide-assisted photocatalytic degradation of alachlor in TiO2 suspensions, *Environ. Sci. Technol.* 37 (2003) 2310-2316.

64. C.S. Turchi and D.F. Ollis, Photocatalytic degradation of organic water contaminants: mechanisms involving hydroxyl radical attack, *J. Catal.* 122 (1990) 178.

65. M. Klare, J. Scheen, K. Vogelsang, H. Jacobs, and J.A. Broekaert, Degradation of short-chain alkyl- and alkanolamines by TiO2- and Pt/TiO2-assisted photocatalysis, *Chemosphere*. 41 (2000) 353-362.

66. P.K. Dutta, S.O. Pehkonen, V.K. Sharma, and A.K. Ray, Photocatalytic oxidation of arsenic(III): evidence of hydroxyl radicals, *Environ. Sci. Technol.* 39 (2005) 1827-1834.

67. C. Chen, P. Lei, H. Ji, W. Ma, J. Zhao, H. Hidaka, et al., Photocatalysis by titanium dioxide and polyoxometalate/TiO2 cocatalysts. Intermediates and mechanistic study, *Environ. Sci. Technol.* 38 (2004) 329-37.

68. M. Cho, H. Chung, W. Choi, and J. Yoon, Linear correlation between inactivation of *E. coli* and OH radical concentration in TiO_2 photocatalytic disinfection, *Water Res.* 38 (2004) 1069-1077.

69. WHO, *Emerging issues in water and infectious disease*. 2003, World Health Organization: Geneva.

70. M.T. Magdigan and J.M. Martinko, *Brock Biology of Microorganisms*. 11 ed., Pearson Education, Inc, Upper Saddle River, NJ, 2006.

71. WHO, *Guidelines for drinking-water quality*. 3rd ed., World Health Organization, Genva, 2008.

72. R. Matuszewska, Protozoan pathogens of genus *Cryptosporidium* and *Giardia*. Part I. Occurrence in water environment and health risk, *Rocz. Panstw. Zakl. Hig.* 58 (2007) 569-577.

73. K. Pond, *Water Recreation and Disease. Plausibility of Associated Infections: Acute Effects, Sequelae and Mortality*. IWA Publishing/World Health Organization, London, 2005.

74. J.L. Rennecker, B.J. Mariñas, J.H. Owens, and E.W. Rice, Inactivation of Cryptosporidium parvum oocysts with ozone, *Water Res.* 33 (1999) 2481-2488.

75. M.W. LeChevallier, W.D. Norton, and R.G. Lee, *Giardia* and *Cryptosporidium* spp. in filtered drinking water supplies, *Appl. Environ. Microbiol.* 57 (1991) 2617-2621.

76. EPA, *Drinking Water; National Primary Drinking Water Regulations; Total Coliforms (Including Fecal Coliforms and E. coli); Final Rule*. 1989, United States Environmental Protection Agency.

77. EPA, *National Primary Drinking Water Regulations: Revisions to the Total Coliform Rule*. 2010, US Environmental Protection Agency.

78. H.A. Al-Abadleh and V.H. Grassian, Oxide surfaces as environmental interfaces, *Surface Science Reports*. 52 (2003) 63-161.

79. G.E. Brown Jr, Surface science: How minerals react with water, *Science*. 294 (2001) 67-69.

80. H.P. Boehm, Acidic and basic properties of hydroxylated metal oxide surfaces, *Discuss. Faraday Soc.* 52 (1971) 264-275.

81. E.V. Stefanovich and T.N. Truong, Ab initio study of water adsorption on TiO_2(110): molecular adsorption versus dissociative chemisorption, *Chem. Phys. Lett.* 299 (1999) 623-629.

82. H.C. William and A.C. Marcus, Brønsted reactions on oxide mineral surfaces and the temperature-dependence of their dissolution rates, *Aquatic Sciences*. 55 (1993) 304-313.

83. A. Davis James and O. Leckie James, *Speciation of adsorbed ions at the oxide/water interface*, Chemical Modeling in Aqueous Systems, American Chemical Society, 1979, pp. 299-317.

84. S. Yurdakal, V. Loddo, B. Bayarri Ferrer, G. Palmisano, V. Augugliaro, J. Gimenez Farreras, et al., Optical properties of TiO_2 suspensions: Influence of pH and powder concentration on mean particle size, *Ind. Eng. Chem. Res.* 46 (2007) 7620-7626.

85. M. Predota, Z. Zhang, P. Fenter, D.J. Wesolowski, and P.T. Cummings, Electric double layer at the rutile (110) surface. 2. adsorption of ions from molecular dynamics and X-ray experiments, *J. Phys. Chem. B.* 108 (2004) 12061-12072.

86. C. Kormann, D.W. Bahnemann, and M.R. Hoffmann, Photolysis of chloroform and other organic molecules in aqueous titanium dioxide suspensions, *Environ. Sci. Technol.* 25 (1991) 494-500.

87. F. Gonzalez-Caballero and V.N. Shilov, Electrical double-layer at a colloid particle, *Encyclopedia of Surface and Colloid Science: Second Edition*, (2006) 1932 - 1936.

88. T. Imae, K. Muto, and S. Ikeda, The pH dependence of dispersion of TiO_2 particles in aqueous surfactant solutions, *Colloid Polym. Sci.* 269 (1991) 43-48.

89. Z.E. Allouni, M.R. Cimpan, P.J. Høl, T. Skodvin, and N.R. Gjerdet, Agglomeration and sedimentation of TiO_2 nanoparticles in cell culture medium, *Colloids Surf. B.* 68 (2009) 83-87.

90. V. Cabuil, P. Leviz, C. Treiner, R. Tsekov, E. Evstatieva, K.W. Stöckelhuber, et al., *Stability of TiO_2 suspensions in reactors for degradation of toxic pollutants*, in: V. Cabuil, P. Leviz, and C. Treiner (Eds.), Trends in Colloid and Interface Science XVII, Springer Berlin / Heidelberg, 2004, pp. 117-120.

91. R.A. French, A.R. Jacobson, B. Kim, S.L. Isley, R.L. Penn, and P.C. Baveye, Influence of ionic strength, pH, and cation valence on aggregation kinetics of titanium dioxide nanoparticles, *Environ. Sci. Technol.* 43 (2009) 1354-1359.

92. C. Sentein, B. Guizard, S. Giraud, C. Yé, and F. Ténégal, Dispersion and stability of TiO_2 nanoparticles synthesized by laser pyrolysis in aqueous suspensions, *J. Phys.: Conf. Ser.* 170 (2009) 012013.

93. R.J. Watts, S. Kong, and W. Lee, Sedimentation and reuse of titanium dioxide: application to suspended-photocatalyst reactors, *J. Environ. Eng.* 121 (1995) 730-735.

94. D.C. Grahame, The electrical double layer and the theory of electrocapillarity, *Chem. Rev.* 41 (1947) 441-501.

95. O. Stern, The theory of the electric double layer, *Z. Elektrochem*. 30 (1924) 508.

96. R. Rodriguez, M.A. Blesa, and A.E. Regazzoni, Surface complexation at the TiO_2(anatase)/aqueous solution interface: chemisorption of catechol. 177 (1996) 122-131.

97. J. Lausmaa, P. Löfgren, and B. Kasemo, Adsorption and coadsorption of water and glycine on TiO_2, *J. Biomed. Mater. Res.* 44 (1999) 227-242.

98. Y.-X. Weng, L. Li, Y. Liu, L. Wang, and G.-Z. Yang, Surface-binding forms of carboxylic groups on nanoparticulate TiO_2 surface studied by the interface-sensitive transient triplet-state molecular probe, *J. Phys. Chem. B.* 107 (2003) 4356-4363.

99. P. Olivera, M. Patrito, and H. Sellers, *Electronic Structure Calculations of Polyatomic Oxyanions Adsorbed on Metal Surfaces*, in: A. Więckowski (Ed.), Interfacial electrochemistry: theory, experiment, and applications, Marcel Dekker, Inc. New York, 1999.

100. V.E. Kazarinov, V.N. Andreev, and A.P. Mayorov, Investigation of the adsorption properties of the TiO_2 electrode by the radioactive tracer method, *Journal of Electroanalytical Chemistry and Interfacial Electrochemistry*. 130 (1981) 277-285.

101. G. Horányi, Investigation of the specific adsorption of sulfate ions on powdered TiO_2, *J. Colloid Interface Sci.* 261 (2003) 580-583.

102. M. Boström, V. Deniz, G.V. Franks, and B.W. Ninham, Extended DLVO theory: electrostatic and non-electrostatic forces in oxide suspensions, *Adv. Colloid Interface Sci.* 123-126 (2006) 5-15.

103. P. Demchick and A.L. Koch, The permeability of the wall fabric of *Escherichia coli* and Bacillus subtilis, *J. Bacteriol.* 178 (1996) 768-773.

104. M.C.M. van Loosdrecht, J. Lyklema, W. Norde, and A.J.B. Zehnder, Bacterial adhesion: A physicochemical approach, *Microb. Ecol.* 17 (1989) 1-15.

105. W.M. Oleary, Fatty acids of bacteria, *Bacteriol. Rev.* 26 (1962) 421-&.

106. J.E. Cronan, Jr. and E.P. Gelmann, An estimate of the minimum amount of unsaturated fatty acid required for growth of *Escherichia coli*, *J. Biol. Chem.* 248 (1973) 1188-1195.

107. K. Magnuson, S. Jackowski, C.O. Rock, and J.E. Cronan, Jr., Regulation of fatty acid biosynthesis in *Escherichia coli*, *Microbiol. Mol. Biol. Rev.* 57 (1993) 522-542.

108. J.S. Cox, D.S. Smith, L.A. Warren, and F.G. Ferris, Characterizing heterogeneous bacterial surface functional groups using discrete affinity spectra for proton binding, *Environ. Sci. Technol.* 33 (1999) 4514-4521.

109. R.E. Martinez, D.S. Smith, E. Kulczycki, and F.G. Ferris, Determination of intrinsic bacterial surface acidity constants using a Donnan shell model and a continuous pK_a distribution method, *J. Colloid Interface Sci.* 253 (2002) 130-139.

110. A. van der Wal, W. Norde, A.J.B. Zehnder, and J. Lyklema, Determination of the total charge in the cell walls of Gram-positive bacteria, *Colloids Surf. B.* 9 (1997) 81-100.

111. W. Jiang, A. Saxena, B. Song, B.B. Ward, T.J. Beveridge, and S.C.B. Myneni, Elucidation of functional groups on Gram-positive and Gram-negative bacterial surfaces using infrared spectroscopy, *Langmuir*. 20 (2004) 11433-11442.

112. T.R. Neu, Significance of bacterial surface-active compounds in interaction of bacteria with interfaces, *Microbiol. Rev.* 60 (1996) 151-166.

113. A.T. Poortinga, R. Bos, W. Norde, and H.J. Busscher, Electric double layer interactions in bacterial adhesion to surfaces, *Surface Science Reports*. 47 (2002) 1-32.

114. A.T. Poortinga, *Electric double layer interactions in bacterial adhesion and detachment*, Institute of Biomedical Materials Science and Applications, University of Groningen, PhD, 2001.

115. R. Sonohara, N. Muramatsu, H. Ohshima, and T. Kondo, Difference in surface properties between *Escherichia coli* and *Staphylococcus aureus* as revealed by electrophoretic mobility measurements, *Biophys. Chem.* 55 (1995) 273-277.

116. H. Ohshima and T. Kondo, Relationship among the surface potential, Donnan potential and charge density of ion-penetrable membranes, *Biophys. Chem.* 38 (1990) 117-122.

117. H. Ohshima, Electrophoresis of soft particles, *Adv. Colloid Interface Sci.* 62 (1995) 189-235.

118. H.J. Busscher and A.H. Weerkamp, Specific and non-specific interactions in bacterial adhesion to solid substrata, *FEMS Microbiol. Lett.* 46 (1987) 165-173.

119. E. Wasserman and A.R. Felmy, Computation of the electrical double layer properties of semipermeable membranes in multicomponent electrolytes, *Appl. Environ. Microbiol.* 64 (1998) 2295-2300.

120. K. Makino, H. Ohshima, and T. Kondo, Surface potential of an ion-penetrable charged membrane, *J. Theor. Biol.* 125 (1987) 367-368.

121. C.J. Van Oss, *Interfacial forces in aqueous media*. M. Dekker, New York, 1994.

122. A. Luttge, L. Zhang, and K.H. Nealson, Mineral surfaces and their implications for microbial attachment: Results from Monte Carlo simulations and direct surface observations, *Am. J. Sci.* 305 (2005) 766-790.

123. B.A. Jucker, H. Harms, S.J. Hug, and A.J.B. Zehnder, Adsorption of bacterial surface polysaccharides on mineral oxides is mediated by hydrogen bonds, *Colloids Surf. B.* 9 (1997) 331-343.

124. P. Landini and A.J.B. Zehnder, The global regulatory hns gene negatively affects adhesion to solid surfaces by anaerobically grown *Escherichia coli* by modulating expression of flagellar genes and lipopolysaccharide production, *J. Bacteriol.* 184 (2002) 1522-1529.

125. T. Taguchi, H. Terui, H. Ohshima, and T. Kondo, Interaction between an ion-penetrable particle and a solid particle. II. Criteria for heterocoagulation, *Colloid & Polymer Science*. 268 (1990) 83-87.

126. H. Terui, T. Taguchi, H. Ohshima, and T. Kondo, Interaction between an ion-penetrable particle and a solid particle. 1. Electrical double-layer interaction, *Colloid & Polymer Science*. 268 (1990) 76-82.

127. H. Ohshima and T. Kondo, Electrostatic interaction of an ion-penetrable sphere with a hard plate: Contribution of image interaction, *J. Colloid Interface Sci.* 157 (1993) 504-508.

128. J.-P. Hsu and B.-T. Liu, Electrical interaction between two spherical particles covered by an ion-penetrable charged membrane, *Chem. Phys.* 236 (1998) 63-76.

129. Y.-C. Kuo, M.-Y. Hsieh, and J.-P. Hsu, Interactions between a particle covered by an ion-penetrable charged membrane and a charged surface: A modified Gouy-Chapman theory, *Langmuir*. 18 (2002) 2789-2794.

130. H. Chick, An investigation of the laws of disinfection, *J. Hyg. (Lond).* 8 (1908) 92-158.

131. J.N. McClellan, *Modeling chlorine decay and chlorination by-product formation in water treatment and distribution*, University of Massachusetts Amherst, 2000.

132. C.N. Haas, J. Joffe, U. Anmangandla, and J.C. Hornberger, *Development and Validation of Rational Design Methods of Disinfection.* AWWA Research Foundation and American Water Works Association, Denver, CO, 1995.

133. L.K. Weavers and G.B. Wickramanayake, *Kinetics of inactivation of microorganisms*, in: S.S. Block (Ed.), Disinfection, sterilization, and preservation, Lippincott Williams & Wilkins, 2001, pp. 65-78.

134. H.E. Watson, A note on the variation of the rate of disinfection with change in the concentration of the disinfectant, *J. Hyg. (Lond).* 8 (1908) 536-542.

135. EPA, *Alternative disinfections and oxidants guidance manual*. 1999, Office of Water.

136. A.G. Rincon, C. Pulgarin, N. Adler, and P. Peringer, Interaction between *E. coli* inactivation and DBP-precursors -- dihydroxybenzene isomers -- in the photocatalytic process of drinking-water disinfection with TiO_2, *J. Photochem. Photobiol. A.* 139 (2001) 233-241.

137. L.W. Hom, Kinetics of chlorine disinfection in an ecosystem, *J. Sanitary Eng. Div.* 98 (1972) 183-194.

138. C. Wei, W.Y. Lin, Z. Zainal, N.E. Williams, K. Zhu, A.P. Kruzic, et al., Bactericidal activity of TiO_2 photocatalyst in aqueous media: Toward a solar-assisted water disinfection system, *Environ. Sci. Technol.* 28 (2002) 934-938.

139. M.G. Corradini, M.D. Normand, and M. Peleg, Stochastic and deterministic model of microbial heat inactivation, *J. Food Sci.* 75 (2010) R59-R70.

140. M. Peleg and K. Shetty, Modeling microbial populations with the original and modified versions of the continuous and discrete logistic equations, *Crit. Rev. Food Sci. Nutr.* 37 (1997) 471 - 490.

141. M. Peleg, Modeling and simulation of microbial survival during treatments with a dissipating lethal chemical agent, *Food Research International*. 35 (2002) 327-336.

142. M. Peleg and M.B. Cole, Reinterpretation of microbial survival curves, *Crit. Rev. Food Sci. Nutr.* 38 (1998) 353 - 380.

143. M. Peleg, M.D. Normand, and E. Damrau, Mathematical interpretation of dose-response curves, *Bull. Math. Biol.* 59 (1997) 747-761.

144. M.A.J.S. van Boekel, On the use of the Weibull model to describe thermal inactivation of microbial vegetative cells, *Int. J. Food Microbiol.* 74 (2002) 139-159.

145. B.F. Severin, M.T. Suidan, and R.S. Engelbrecht, Kinetic modeling of U.V. disinfection of water, *Water Res.* 17 (1983) 1669-1678.

146. B.F. Severin, M.T. Suidan, and R.S. Engelbrecht, Series-event kinetic model for chemical disinfection, *J. Environ. Eng.* 110 (1984) 430-439.

147. C.N. Haas, A mechanistic kinetic model for chlorine disinfection, *Environmental Science & Technology*. 14 (1980) 339-340.

148. Z. Adamczyk, B. Siwek, M. Zembala, and P. Belouschek, Kinetics of localized adsorption of colloid particles, *Adv. Colloid Interface Sci.* 48 (1994) 151-280.

149. P. Fernandez-Ibanez, J. Blanco, S. Malato, and F.J. de las Nieves, Application of the colloidal stability of TiO2 particles for recovery and reuse in solar photocatalysis, *Water Res.* 37 (2003) 3180-3188.

150. M.R. Oberholzer, J.M. Stankovich, S.L. Carnie, D.Y.C. Chan, and A.M. Lenhoff, 2-D and 3-D interactions in random sequential adsorption of charged particles, *J. Colloid Interface Sci.* 194 (1997) 138-153.

151. B. Widom, Random sequential addition of hard spheres to a volume, *J. Chem. Phys.* 44 (1966) 3888-3894.

152. Z. Adamczyk, M. Zembala, B. Siwek, and P. Warszynski, Structure and ordering in localized adsorption of particles, *J. Colloid Interface Sci.* 140 (1990) 123-137.

153. Z. Adamczyk, Kinetics of diffusion-controlled adsorption of colloid particles and proteins, *J. Colloid Interface Sci.* 229 (2000) 477-489.

154. Q. Yang, P. Ling Ang, M.B. Ray, and S.O. Pehkonen, Light distribution field in catalyst suspensions within an annular photoreactor, *Chem. Eng. Sci.* 60 (2005) 5255-5268.

155. C.G. Hatchard and C.A. Parker, A new sensitive chemical actinometer. II. Potassium ferrioxalate as a standard chemical actinometer, *Proceedings of the Royal Society of London. Series A, Mathematical and Physical Sciences*. 235 (1956) 518-536.

156. H.J. Kuhn, S.E. Braslavsky, and R. Schmidt, Chemical actinometry, *Pure Appl. Chem.* 76 (2004) 2105-2146.

157. N.J. Bunce, J. LaMarre, and S.P. Vaish, Photorearrangement of azoxybenzene to 2-hydroxyazobenzene: a convenient chemical actinometer, *Photochem. Photobiol.* 39 (1984) 531-533.

158. L. Sun and J.R. Bolton, Determination of the quantum yield for the photochemical generation of hydroxyl radicals in TiO_2 suspensions, *J. Phys. Chem.* 100 (1996) 4127-4134.

159. H. Zhang, G. Chen, and D.W. Bahnemann, *Environmental Photo(electro)catalysis: Fundamental Principles and Applied Catalysts*, in: C. Comninellis and G. Chen (Eds.), Electrochemistry for the Environment, Springer. New York, 2010.

160. A.-G. Rincon and C. Pulgarin, Effect of pH, inorganic ions, organic matter and H_2O_2 on *E. coli* K12 photocatalytic inactivation by TiO_2: Implications in solar water disinfection, *Appl. Catal. B.* 51 (2004) 283-302.

161. W. Chu and C.C. Wong, The photocatalytic degradation of dicamba in TiO2 suspensions with the help of hydrogen peroxide by different near UV irradiations, *Water Res.* 38 (2004) 1037-43.

162. Y. Wang and C.-s. Hong, Effect of hydrogen peroxide, periodate and persulfate on photocatalysis of 2-chlorobiphenyl in aqueous TiO2 suspensions, *Water Res.* 33 (1999) 2031-2036.

163. J. Thiebaud, F. Thevent, and C. Fittschen, OH radicals and H_2O_2 molecules in the gas phase near to TiO_2 surfaces, *J. Phys. Chem. C.* 114 (2010) 3082-3088.

164. M.C. Lee and W. Choi, Solid phase photocatalytic reaction on the soot/TiO_2 interface: The role of migrating OH radicals, *J. Phys. Chem. B.* 106 (2002) 11818-11822.

165. Y. Murakami, E. Kenji, A.Y. Nosaka, and Y. Nosaka, Direct detection of OH radicals diffused to the gas phase from the UV-irradiated photocatalytic TiO_2 surfaces by means of laser-induced fluorescence spectroscopy, *J. Phys. Chem. B.* 110 (2006) 16808-16811.

166. R. Roots and S. Okada, Estimation of life times and diffusion distances of radicals involved in x-ray-induced DNA strand breaks or killing of mammalian cells, *Radiat. Res.* 64 (1975) 306-320.

167. Y. Murakami, K. Endo, I. Ohta, A.Y. Nosaka, and Y. Nosaka, Can OH radicals diffuse from the UV-irradiated photocatalytic TiO_2 surfaces? Laser-induced-fluorescence study, *J. Phys. Chem. C.* 111 (2007) 11339-11346.

168. I.M. Svishchev and A.Y. Plugatyr, Hydroxyl radical in aqueous solution: Computer simulation, *J. Phys. Chem. B.* 109 (2005) 4123-4128.

169. M.G. Campo and J.R. Grigera, Classical molecular-dynamics simulation of the hydroxyl radical in water, *J. Chem. Phys.* 123 (2005.

170. A. Kupperman, *Diffusion model of the radiation chemistry of aqueous solutions*, in: G. Silini (Ed.), Radiation Research: Proceedings of the Third International Congress of Radiation Research, Wiley. New York, 1967, pp. 212-234.

171. P. Vassilev, M.J. Louwerse, and E.J. Baerends, Ab initio molecular dynamics simulation of the OH radical in liquid water, *Chem. Phys. Lett.* 398 (2004) 212-216.

172. M.G. Campo and J.R. Grigera, Classical molecular-dynamics simulation of the hydroxyl radical in water, *J. Chem. Phys.* 123 (2005) 084507-6.

173. B. Halliwell and J. Gutteridge, *Free radicals in biology and medicine*. 2nd ed., Clarendon Press, Oxford, 1989.

174. W.A. Pryor (Ed.), *Free radicals in biology*. Academic Press, Inc, New York, 1976.

175. R.T. Dean, S. Fu, R. Stocker, and M.J. Davies, Biochemistry and pathology of radical-mediated protein oxidation, *Biochem. J.* 324 (1997) 1-18.

176. C.L. Hawkins and M.J. Davies, Generation and propagation of radical reactions on proteins, *Biochimica et Biophysica Acta (BBA) - Bioenergetics*. 1504 (2001) 196-219.

177. J.M.C. Gutteridge, Lipid peroxidation initiated by superoxide-dependent hydroxyl radicals using complexed iron and hydrogen peroxide, *FEBS Lett.* 172 (1984) 245-249.

178. Y.W. Cheng, R.C.Y. Chan, and P.K. Wong, Disinfection of *Legionella pneumophila* by photocatalytic oxidation, *Water Res.* 41 (2007) 842-852.

179. Z.-X. Lu, L. Zhou, Z.-L. Zhang, W.-L. Shi, Z.-X. Xie, H.-Y. Xie, et al., Cell damage induced by photocatalysis of TiO_2 thin films, *Langmuir*. 19 (2003) 8765-8768.

180. N.-p. Huang, X. Min-hua, C.-w. Yuan, and Y. Rui-rong, The study of the photokilling effect and mechanism of ultrafine TiO*2* particles on U937 cells, *J. Photochem. Photobiol. A.* 108 (1997) 229-233.

181. I.L. Stefan and F. Irwin, Superoxide and iron: partners in crime, *IUBMB Life*. 48 (1999) 157-161.

182. A. Carlioz and D. Touati, Isolation of superoxide-dismutase mutants in *Escherichia coli* - Is superoxide-dismutase necessary for aerobic life, *EMBO J.* 5 (1986) 623-630.

183. J. Kiwi and V. Nadtochenko, Evidence for the mechanism of photocatalytic degradation of the bacterial wall membrane at the TiO_2 interface by ATR-FTIR and laser kinetic spectroscopy, *Langmuir*. 21 (2005) 4631-4641.

184. J. Kiwi and V. Nadtochenko, New evidence for TiO_2 photocatalysis during bilayer lipid peroxidation, *J. Phys. Chem. B.* 108 (2004) 17675-17684.

185. V.A. Nadtochenko, A.G. Rincon, S.E. Stanca, and J. Kiwi, Dynamics of *E. coli* membrane cell peroxidation during TiO_2 photocatalysis studied by ATR-FTIR spectroscopy and AFM microscopy, *J. Photochem. Photobiol. A.* 169 (2005) 131-137.

186. N. Porter, S. Caldwell, and K. Mills, Mechanisms of free radical oxidation of unsaturated lipids, *Lipids*. 30 (1995) 277-290.

187. D.R. Janero, Malondialdehyde and thiobarbituric acid-reactivity as diagnostic indices of lipid peroxidation and peroxidative tissue injury, *Free Radic. Biol. Med.* 9 (1990) 515-540.

188. Z.-Y. Jiang, A. Woollard, and S. Wolff, Lipid hydroperoxide measurement by oxidation of Fe_2^+ in the presence of xylenol orange. Comparison with the TBA assay and an iodometric method, *Lipids*. 26 (1991) 853-856.

189. D.J.W. Barber and J.K. Thomas, Reactions of radicals with lecithin bilayers, *Radiat. Res.* 74 (1978) 51-65.

190. J.M. Joseph and C.T. Aravindakumar, Determination of rate constants for the reaction of hydroxyl radicals with some purines and pyrimidines using sunlight, *J. Biochem. Biophys. Methods*. 42 (2000) 115-124.

191. G.V. Buxton, C.L. Greenstock, W.P. Helman, and A.B. Ross, Critical review of rate constants for reactions of hydrated electron, hydrogen atom and hydroxyl radicals (OH/O−) in aqueous solution, *J. Phys. Chem. Ref. Data*. 17 (1988) 513–817.

192. C. Minero, G. Mariella, V. Maurino, D. Vione, and E. Pelizzetti, Photocatalytic transformation of organic compounds in the presence of inorganic ions. 2. Competitive reactions of phenol and alcohols on a titanium dioxide-fluoride system, *Langmuir*. 16 (2000) 8964-8972.

193. P. Calza and E. Pelizzetti, Photocatalytic transformation of organic compounds in the presence of inorganic ions, *Pure Appl. Chem.* 73 (2001) 1839-1848.

194. H.Y. Chen, O. Zahraa, and M. Bouchy, Inhibition of the adsorption and photocatalytic degradation of an organic contaminant in an aqueous suspension of TiO_2 by inorganic ions, *J. Photochem. Photobiol. A.* 108 (1997) 37-44.

195. C. Guillard, E. Puzenat, H. Lachheb, A. Houas, and J.-M. Herrmann, Why inorganic salts decrease the TiO_2 photocatalytic efficiency, *International Journal of Photoenergy*. 7 (2005) 1-9.

196. M. Abdullah, G.K.C. Low, and R.W. Matthews, Effects of common inorganic anions on rates of photocatalytic oxidation of organic carbon over illuminated titanium dioxide, *J. Phys. Chem.* 94 (1990) 6820-6825.

197. C. Kormann, D.W. Bahnemann, and M.R. Hoffmann, Photolysis of chloroform and other organic molecules in aqueous TiO2 suspensions, *Environ. Sci. Technol.* 25 (1991) 494-500.

198. M.B. McBride, *Environmental chemistry of soils*. Oxford University Press, 1994.

199. D.A. Dzombak and F. Morel, *Surface complexation modeling: hydrous ferric oxide*. Wiley, 1990.

200. Y. Ku, W.-H. Lee, and W.-Y. Wang, Photocatalytic reduction of carbonate in aqueous solution by UV/TiO_2 process, *J. Mol. Catal. A: Chem*. 212 (2004) 191-196.

201. S.J. Hug and B. Sulzberger, In situ Fourier transform infrared spectroscopic evidence for the formation of several different surface complexes of oxalate on TiO_2 in the aqueous phase, *Langmuir*. 10 (1994) 3587-3597.

202. P.A. Connor and A.J. McQuillan, Phosphate adsorption onto TiO_2 from aqueous solutions: an in situ internal reflection infrared spectroscopic study, *Langmuir*. 15 (1999) 2916-2921.

203. J. Kochany and E. Lipczynska-Kochany, Application of the EPR spin-trapping technique for the investigation of the reactions of carbonate, bicarbonate, and phosphate anions with hydroxyl radicals generated by the photolysis of H_2O_2, *Chemosphere*. 25 (1992) 1769-1782.

204. R.W. Matthews, H.A. Mahlman, and T.J. Sworski, Elementary processes in the radiolysis of aqueous sulfuric acid solutions. Determinations of both GOH and GSO4, *The Journal of Physical Chemistry*. 76 (1972) 1265-1272.

205. C.Y. Chang, K.S. Yao, J.H. Lee, and C.H. Chen, Formation and calculation of hydroxyl radical in the optimal photocatalytic process using the Taguchi method, *Environmental Informatics*. 5 (2007) 655-663.

206. I. Tejero, A. Gonzalez-Lafont, J.M. Lluch, and L.A. Eriksson, Theoretical modeling of hydroxyl-radical-induced lipid peroxidation reactions, *J. Phys. Chem. B.* 111 (2007) 5684-5693.

207. M.A. Cubillos, E.A. Lissi, and E.B. Abuin, Kinetics of lipid peroxidation in compartmentalized systems initiated by a water-soluble free radical source, *Chem. Phys. Lipids*. 104 (2000) 49-56.

208. B.A. Wagner, G.R. Buettner, and C.P. Burns, Free radical-mediated lipid peroxidation in cells: oxidizability is a function of cell lipid bis-allylic hydrogen content, *Biochemistry*. 33 (2002) 4449-4453.

209. Q.-T. Li, M.H. Yeo, and B.K. Tan, Lipid peroxidation in small and large phospholipid unilamellar vesicles induced by water-soluble free radical sources, *Biochem. Biophys. Res. Commun.* 273 (2000) 72-76.

210. J.M.C. Gutteridge, The use of standards for malonyldialdehyde, *Anal. Biochem.* 69 (1975) 518-526.

211. J.M.C. Gutteridge and B. Halliwell, The measurement and mechanism of lipid peroxidation in biological systems, *Trends Biochem. Sci.* 15 (1990) 129-135.

212. S.K. Jain, The accumulation of malonyldialdehyde, a product of fatty acid peroxidation, can disturb aminophospholipid organization in the membrane bilayer of human erythrocytes, *J. Biol. Chem.* 259 (1984) 3391-3394.

213. K. Moore and L.J. Roberts, Measurement of lipid peroxidation, *Free Radic. Res.* 28 (1998) 659-671.

214. T. Iwaoka, F. Tabata, and T. Takahashi, Lipid peroxidation and lipid peroxide detected by chemiluminescence, *Free Radic. Biol. Med.* 3 (1987) 329-333.

215. A.G. Marr and J.L. Ingraham, Effect of temperature on the composition of fatty acids in *Escherichia coli, J. Bacteriol.* 84 (1962) 1260-1267.

216. C.O. Gill, Effect of growth temperature on the lipids of *Pseudomonas fluorescens, J Gen Microbiol*. 89 (1975) 293-298.

217. J.E. Cronan, Jr., Phospholipid alterations during growth of *Escherichia coli*, *J. Bacteriol.* 95 (1968) 2054-2061.

218. R.C. Weast, *Handbook of Chemistry and Physics.* 53 ed., Chemical Rubber Cleveland, 1972.

219. M.C. Hidalgo, G. Colón, and J.A. Navío, Modification of the physicochemical properties of commercial TiO_2 samples by soft mechanical activation, *J. Photochem. Photobiol. A.* 148 (2002) 341-348.

220. E. Danačíková, J. John, A. Motl, F. Šebesta, and E. Hooper, Study of sorption properties of various titanium dioxide materials, *Czech J. Phys.* 49 (1999) 789-795.

221. D.V. Bavykin and F.C. Walsh, *Titanate and titania nanotubes: synthesis, properties and applications*. Royal Society of Chemistry, Cambridge, 2010.

222. A. Savitzky and M.J.E. Golay, Smoothing and differentiation of data by simplified least squares procedures, *Anal. Chem.* 36 (1964) 1627-1639.

223. Z.-Y. Jiang, J.V. Hunt, and S.P. Wolff, Ferrous ion oxidation in the presence of xylenol orange for detection of lipid hydroperoxide in low density lipoprotein, *Anal. Biochem.* 202 (1992) 384-389.

224. J.E. Cronan, Jr. and C.O. Rock, The presence of linoleic acid in *Escherichia coli* cannot be confirmed, *J. Bacteriol.* 176 (1994) 3069-3071.

225. A. Pal, S.O. Pehkonen, L.E. Yu, and M.B. Ray, Photocatalytic inactivation of Gram-positive and Gram-negative bacteria using fluorescent light, *J. Photochem. Photobiol. A.* 186 (2007) 335-341.

226. Y. Horie, D.A. David, M. Taya, and S. Tone, Effects of light intensity and titanium dioxide concentration on photocatalytic sterilization rates of microbial cells, *Ind. Eng. Chem. Res.* 35 (1996) 3920-3926.

227. M. Kaneko, M. Kaneko, and I. Okura (Eds.), *Photocatalysis: science and technology*. Biological and Medical Physics Series, Springer, New York, 2002.

228. C.S. Turchi. *Effect of light intensity on photocatalytic reaction*. in *Potential applications of concentrated solar energy: proceedings of a workshop*. 1991. Washington, D.C.: Commission on Engineering and Technical Systems (CETS).

229. T.A. Egerton and C.J. King, Influence of light intensity on photoactivity in titanium dioxide pigmented systems, *J. Oil Col. Chem. Assoc.* 62 (1979) 386-391.

230. H.M. Coleman, M.I. Abdullah, B.R. Eggins, and F.L. Palmer, Photocatalytic degradation of 17[beta]-oestradiol, oestriol and 17[alpha]-ethynyloestradiol in water monitored using fluorescence spectroscopy, *Appl. Catal. B.* 55 (2005) 23-30.

231. C. Lee, J. Barnett, and P.D. Reaven, Liposomes enriched in oleic acid are less susceptible to oxidation and have less proinflammatory activity when exposed to oxidizing conditions, *J. Lipid Res.* 39 (1998) 1239-1247.

232. S. Parra, J. Olivero, and C. Pulgarin, Relationships between physicochemical properties and photoreactivity of four biorecalcitrant phenylurea herbicides in aqueous TiO2 suspension, *Appl. Catal. B.* 36 (2002) 75-84.

233. C.-Y. Chang, Y.-H. Hsieh, L.-L. Hsieh, K.-S. Yao, and T.-C. Cheng, Establishment of activity indicator of TiO_2 photocatalytic reaction--Hydroxyl radical trapping method, *J. Hazard. Mater.* 166 (2009) 897-903.

234. C. Watson, I. Janik, T. Zhuang, O. CharvaÌtovaÌ, R.J. Woods, and J.S. Sharp, Pulsed electron beam water radiolysis for submicrosecond hydroxyl radical protein footprinting, *Anal. Chem.* 81 (2009) 2496-2505.

235. J. Lyklema, H.P. van Leeuwen, and M. Minor, DLVO-theory, a dynamic re-interpretation, *Adv. Colloid Interface Sci.* 83 (1999) 33-69.

236. G.J. Liu, X.R. Zhang, L. McWilliams, J.W. Talley, and C.R. Neal, Influence of ionic strength, electrolyte type, and NOM on As(V) adsorption onto TiO_2, *Journal of Environmental Science and Health, Part A: Toxic/Hazardous Substances and Environmental Engineering*. 43 (2008) 430 - 436.

237. K. Suttiponparnit, J. Jiang, M. Sahu, S. Suvachittanont, T. Charinpanitkul, and P. Biswas, Role of surface area, primary particle size, and crystal phase on titanium dioxide nanoparticle dispersion properties, *Nanoscale Research Letters*. 6 (2010) 1-8.

238. A. Zita and M. Hermansson, Effects of ionic strength on bacterial adhesion and stability of flocs in a wastewater activated sludge system, *Appl. Environ. Microbiol.* 60 (1994) 3041-3048.

239. T. Saito, T. Iwase, J. Horie, and T. Morioka, Mode of photocatalytic bactericidal action of powdered semiconductor TiO_2 on mutans streptococci, *J. Photochem. Photobiol. B.* 14 (1992) 369-379.

240. P.R. Cullis and B. De Kruijff, The polymorphic phase behaviour of phosphatidylethanolamines of natural and synthetic origin. A 31P NMR study, *Biochimica et Biophysica Acta (BBA) - Biomembranes*. 513 (1978) 31-42.

241. P.L. Yeagle and A. Sen, Hydration and the lamellar to hexagonal(II) phase transition of phosphatidylethanolamine, *Biochemistry*. 25 (1986) 7518-7522.

242. A.M. Jentzsch, H. Bachmann, P. Fürst, and H.K. Biesalski, Improved analysis of malondialdehyde in human body fluids, *Free Radic. Biol. Med.* 20 (1996) 251-256.

243. K.J. Dennis and T. Shibamoto, Gas chromatographic determination of malonaldehyde formed by lipid peroxidation, *Free Radic. Biol. Med.* 7 (1989) 187-192.

244. A.F. Vikbjerg, T.L. Andresen, K. Jørgensen, H. Mu, and X. Xu, Oxidative stability of liposomes composed of docosahexaenoic acid-containing phospholipids, *J. Am. Oil Chem. Soc.* 84 (2007) 631-637.

245. C.M. Hart, J.K. Tolson, and E.R. Block, Supplemental fatty acids alter lipid peroxidation and oxidant injury in endothelial cells, *Am J Physiol Lung Cell Mol Physiol*. 260 (1991) L481-488.

246. J. Cosgrove, D. Church, and W. Pryor, The kinetics of the autoxidation of polyunsaturated fatty acids, *Lipids*. 22 (1987) 299-304.

247. M.J. Davies, The oxidative environment and protein damage, *Biochimica et Biophysica Acta (BBA) - Proteins & Proteomics*. 1703 (2005) 93-109.

APPENDICES

Appendix A: Computer Codes

```
function [yprime]=rateeq(t,y,k,r,Ia,mcat)

%A function that contains the rate equations for photocatalytic disinfection

% m[*OH]+[cell]l = [cell]d + x[BP] ---------- (1)

% [*OH]+[BP] = [BP] ---------- (2)


% Since the states are passed in as a single vector, let

% y(1) = [*OH], i.e., concentration of OH radicals

% y(2) = [cell]l, i.e., concentration of live cells

% y(3) = [BP], i.e., byproduct concentration

% G = generation rate of *OH (uM/s)

% k(1) = rxn rate constant for radicals with cell,% (L/uM/s)

% k2 = rxn rate constant with byproducts (L/uM/s)

% k(2)= order of rxn wrt [*OH]

% k(3) = rxn constant wrt [*OH]

% KQ1 = constant of quenching [HCO3]

% KQ2 = constant of quenching [CL]

% KQ3 = constant of quenching [HPO4]


G = Ia*exp(-7*mcat*r);
```

Appendix A: (Continued)

```
KBP = 1e4; %L/mol

KQ1=6e4; %L/mol

KQ2=1e5; %L/mol

KQ3=8e6; %L/mol

HCO3=0.085;%mol/L

CL=20*6.9*10^-3;%mol/L

HPO4=20*0.59*10^-3;%mol/L

% k(1)=1e5;

% k(2)=1.5;

% k(3)=1;

R=1.535/2;

pH = 7;

H_conc = 10^-(pH);

An_sum = H_conc*(KQ1*HCO3+KQ2*CL+KQ3*HPO4);


theta_BP = KBP*y(3)*1e-3/(1+KBP*y(3)*1e-3+An_sum);


theta_An = H_conc*(KQ1*HCO3+KQ2*CL+KQ3*HPO4)/(1+KBP*y(3)*1e-
3+An_sum);

yprime(1)= (G*(1-(theta_An)-(theta_BP)) - k(3)*((y(1)^k(2))*y(2)))*pi*R;

yprime(2)= (-k(1)*((y(1)^k(2)))*y(2))*pi*R;

yprime(3) = (k(3)*((y(1)^k(2)))*y(2) - G*theta_BP*5e2)*pi*R;
```

Appendix A: (Continued)

```
yprime = yprime(:);

% This ensures that the vector returned is a column vector
```

Appendix A: (Continued)

```
function [yprime] = myfun2 (t,y,k,Ia,mcat)
%A function that numerically integrates the rate equations with respect to reactor
radius

yprime=quadv(@(r)rateeq(t,y,k,r,Ia,mcat),0,0.7675,1e-6);
yprime=yprime(:);
end
```

Appendix A: (Continued)

```
function [C2]=myodefun(k,inv,Ia,mcat)
%A numerical analysis function that solves the set of ODE using a 5th order Runge-
Kutta method

tdata=inv(:,2);
inverse=inv(:,1);
up=max(tdata);
tt=0:0.1:up; % Start time
x0 = [0 1 0] ;% Initial conditions
options = [];

[t,s] = ode45(@myfun2,tt,x0,options,k,Ia,mcat);

OH = s(:,1);
CELL = s(:,2);
BP = s(:,3);

ss=max(size(tdata));

Cmod = interp1(tt,CELL,tdata)/max(CELL);


dlmwrite(Results\simulation\optional\BYPRODUCTS.txt',BP)
dlmwrite(Results\simulation\optional\CELL.txt',CELL)
dlmwrite(Results\simulation\optional\OH.txt',OH)


for i=1:ss
   Cexp(i)=1/inverse(i);
   C2(i)=Cmod(i)*inverse(i);
end
C2=C2(:);
end
```

Appendix A: (Continued)

function myfitmodel()

```
%Fits data to the mechanistic model developed by Dalrymple et al (2011)
%t2 is the time
%Cexp is the experimental data
%E is the error associated with the data
close(gcf)
ext = '.xlsx';
files = {'CTRL'};% 'C161' 'C181' 'C183'};
filestr = strcat(files,ext);
sheetstr ={'MID'};% 'MID' 'LOW'};
%Reads data directly from MS Excel files
cellrange1 = {'M112:R118' 'M6:R12' 'M42:R48' 'M77:R83'};
cellrange2 = {'M177:R183' 'M83:R91'};% 'M6:R14' 'M45:R53' 'M83:R91'};
cellrange3 = {'M130:R141' 'M6:R14' 'M48:R56' 'M89:R97'};

colorset1 = {'ko' 'bs' 'rd' 'g^' 'mv'};
colorset2 = {'k-' 'b-' 'r-' 'g-' 'm-'};

TiO2 = {'0.01' 0.10' '0.25' '0.50'};
Intensity =[1 2 3];
TiO2Num=[0.01 0.10 0.25 0.50];
QY=0.03; %quantum yield for OH generation
```

Appendix A: (Continued)

```
Fs = [0.0019 0.0172 0.0193 0.02]; %fraction of adsorbed light
filenum = max(size(filestr));
sheetnum = max(size(sheetstr));
op=optimset('MaxFunEvals',20000,'MaxIter',10000);
dlmwrite('Results\simulation\optional\ALL_DATA_coef.csv','') %creates blank file
for f = 1:filenum
        filename=char(filestr(f));
          for iii=1:sheetnum
        sheet=char(sheetstr(iii));
    work={'Currently working on ' filename  ' ' sheet '...'};
    update = char(strcat(work));
    disp(update);

    if strcmp(sheet,'HIGH')==1
                        cellrange = cellrange1;
      Io = 4.61e-5;
    else
      if strcmp(sheet,'MID')==1
        cellrange = cellrange2;
        Io = 2.495e-5;
      else
```

Appendix A: (Continued)

```
 cellrange = cellrange3;
    Io = 1.43e-5;
  end
end

file = char(files(f));

  rangesize = max(size(cellrange));
        for r=1:rangesize
 inverse=[];
 yexp=[];
                range = char(cellrange(r));
                data=xlsread(filename,sheet,range);
                t2=data(:,1);
                Cexp = data(:,5);
                E = data(:,6);
                K=[0.01 1.5 4]; %initial guesses
                up = max(t2);
                ss = max(size(Cexp));
 for zz=1:ss
   inverse(zz)=1/Cexp(zz);
   yexp(zz) = 1;
```

Appendix A: (Continued)

```
end
 inverse=inverse(:);
 inverse(:,1)=inverse;
 yexp=yexp(:);
 inverse(:,2)=t2;
 Ia=QY*Io*Fs(r)*1e3
 mcat=TiO2Num(r)
 [x, resnorm] = lsqcurvefit(@myodefun,K,inverse,yexp,[1e-6 1 1],[1e6 5
1e3],op,Ia,mcat);
 x
 resnorm
 [C]=myodefun2(x,inverse,Ia,mcat);
 t3=0:0.1:up;
 t4=t3(:);
 [D]=interp1(t4,C(:,1),t2);

 for i=1:ss
   Y1(i) = log10(Cexp(i));
   Y2(i)= log10(D(i));
   SSY1= Y1(i)^2;
   resY1(i)=(Y1(i)-Y2(i))^2;
   SS(i)=(Cexp(i))^2;
```

Appendix A: (Continued)

```
    res(i)=(Cexp(i)-D(i))^2;
        end

        %Sum of squares in Cexp
        SSy = sum(SS)-((sum(Cexp))^2/ss);
        SSres = sum(res);
        SSyY1=sum(SSY1)-((sum(Y1))^2/ss);
        SSresY1=sum(resY1);

        %Goodness of fit parameters
        Rsq1 = 1-SSres/SSy;
        Rsq2 = 1-SSresY1/SSyY1;
        rms1 = sqrt(SSres/ss);
         rms2 = sqrt(SSresY1/ss);

        Rsq(1)=Rsq1;
        Rsq(2)=Rsq2;
        model_data = [t4 C(:,1)];
        conc = char(TiO2(r));
        csvfilename1 = char(strcat(file,'_',sheet,'_',conc,'model.txt'));
  dlmwrite(' \ALL_DATA_coef.csv',[Intensity(iii) TiO2Num(r) x Rsq1],'-append')
```

Appendix A: (Continued)

```
savelocation1= char(strcat(\Results\simulation\optional\',file,'\',csvfilename1));

    dlmwrite(savelocation1,model_data,'delimiter','\t') %adds time variable to
file

    %plots
                datacolor = char(colorset1(r));
                fitcolor = char(colorset2(r));
                hold on
                subplot (2,2,1), plot(t2,Cexp,datacolor,t4,C(:,1),fitcolor)
                axis([0 max(t2) min(Cexp) max(Cexp)])
                xlabel('Time (min)')
                ylabel('C/C_{o}')
                hold on
                errorbar(t2,Cexp,E,datacolor)
    legend boxoff

                subplot(2,2,2)
    semilogy(t2,Cexp,datacolor,t4,C(:,1),fitcolor)
                hold on
    errorbar(t2,Cexp,E,datacolor)
                errorbarlogy;
```

Appendix A: (Continued)

```
  xlabel('Time (min)')
                        ylabel('log C/C_{o}')
                        axis([0 max(t2) min(Cexp) max(Cexp)])
      legend boxoff


      subplot(2,2,3)
      hold on
      plot(t4,C(:,2),fitcolor)
                        xlabel('Time (min)')
                        ylabel('Byproduct conc')
                        legend boxoff


      subplot(2,2,4)
      hold on
      plot(t4,C(:,3),fitcolor)
      xlabel('Time (min)')
                        ylabel('[OH] mol/L')
                        legend boxoff
    end
   imagename = char(strcat('Results\simulation\optional\',file,'\',sheet,'2'));
                saveas(gcf,imagename,'fig')
    saveas(gcf,imagename,'png')
```

Appendix A: (Continued)

```
        close(gcf); %close figure window
    end
end
```

Appendix B: Fatty Acid Spectra

Microbial ID, Inc.
Volume: DATA File: E103226.46B Samp Ctr: 3 ID Number: 6051
Type: Samp Bottle: 71 Method: RCLIN6
Created: 3/22/2010 3:57:26 PM Created By: sstrauss (Sue Strauss)
Sample ID: C-USF10-03 (01-Luria Broth-Direct DL

RT	Response	Ar/Ht	RFact	ECL	Peak Name	Perc	Comment1	Comment2
0.6998	1.165E+9	0.014	----	6.6894	SOLVENT	----	< min rt	
0.7726	1710	0.012	----	7.1994		----	< min rt	
1.5783	17592	0.008	1.070	12.0018	12:0	3.30	ECL deviates 0.002	Reference 0.001
1.8364	3599	0.009	1.028	12.9998	13:0	0.65	ECL deviates 0.000	Reference 0.003
1.9757	660	0.013	1.011	13.4882	12:0 3OH	0.12	ECL deviates 0.005	
2.0733	1554	0.009	----	13.8307		----		
2.1079	2758	0.007	----	13.9519	unknown 13.951	----	ECL deviates 0.001	
2.1206	49471	0.009	0.995	13.9964	14:0	8.63	ECL deviates -0.004	Reference 0.001
2.2753	6966	0.012	----	14.5094		----		
2.3662	825	0.008	0.972	14.8109	15:1 w8c	0.14	ECL deviates -0.003	
2.4224	24657	0.009	----	14.9973	15:0	----	ECL deviates -0.003	
2.4768	1465	0.009	----	15.1722		----		
2.5818	50518	0.009	0.955	15.5101	Sum In Feature 2	8.46	ECL deviates -0.005	14:0 3OH/16:1 iso I
2.6825	74705	0.009	0.948	15.8344	Sum In Feature 3	12.4	ECL deviates -0.006	16:1 w7c/16:1 w6c
2.7097	1071	0.010	0.946	15.9221	16:1 w5c	0.18	ECL deviates -0.006	
2.7339	217554	0.009	0.945	15.9999	16:0	36.0	ECL deviates 0.000	Reference 0.003
2.7633	2731	0.013	----	16.0942		----		
2.8992	953	0.010	0.935	16.5297	15:0 3OH	0.16	ECL deviates -0.003	
2.9881	1929	0.011	0.930	16.8147	17:1 w8c	0.31	ECL deviates 0.000	
3.0186	81103	0.009	0.928	16.9126	17:0 cyclo	13.2	ECL deviates -0.002	
3.0462	12116	0.009	0.927	17.0011	17:0	1.97	ECL deviates 0.001	Reference 0.002
3.2168	357	0.010	0.919	17.5524	16:0 3OH	0.06	ECL deviates 0.004	
3.2796	2075	0.010	0.916	17.7552	Sum In Feature 5	0.33	ECL deviates -0.001	18:2 w6,9c/18:0
3.3079	73697	0.009	0.914	17.8467	Sum In Feature 8	11.8	ECL deviates -0.001	18:1 w7c
3.3256	740	0.010	0.914	17.9041	Sum In Feature 8	0.12	ECL deviates 0.002	18:1 w6c
3.3567	2772	0.010	0.912	18.0045	18:0	0.44	ECL deviates 0.005	Reference 0.000
3.4593	315	0.009	----	18.3434		----		
3.4668	353	0.009	----	18.3683		----		
3.4991	3233	0.012	----	18.4748		----		
3.5665	1769	0.011	----	18.6977		----		
3.6392	8911	0.010	0.901	18.9379	19:0 cyclo w8c	1.41	ECL deviates 0.006	
3.6568	1223	0.010	0.900	18.9964	19:0	0.19	ECL deviates -0.004	Reference -0.014
3.7066	896	0.014	----	19.1642		----		
----	50518	---	----	----	Summed Feature	8.46	12:0 aldehyde ?	unknown 10.9525
----	-----	---	----	----		----	16:1 iso I/14:0 3OH	14:0 3OH/16:1 iso I
----	74705	---	----	----	Summed Feature	12.4	16:1 w7c/16:1 w6c	16:1 w6c/16:1 w7c
----	2075	---	----	----	Summed Feature	0.33	18:0 ante/18:2 w6,9c	18:2 w6,9c/18:0
----	74437	---	----	----	Summed Feature	11.9	18:1 w7c	18:1 w6c

ECL Deviation: 0.003 Reference ECL Shift: 0.006 Number Reference Peaks: 7
Total Response: 621153 Total Named: 601869

Appendix B: (Continued)

Percent Named: 96.90% Total Amount: 570076

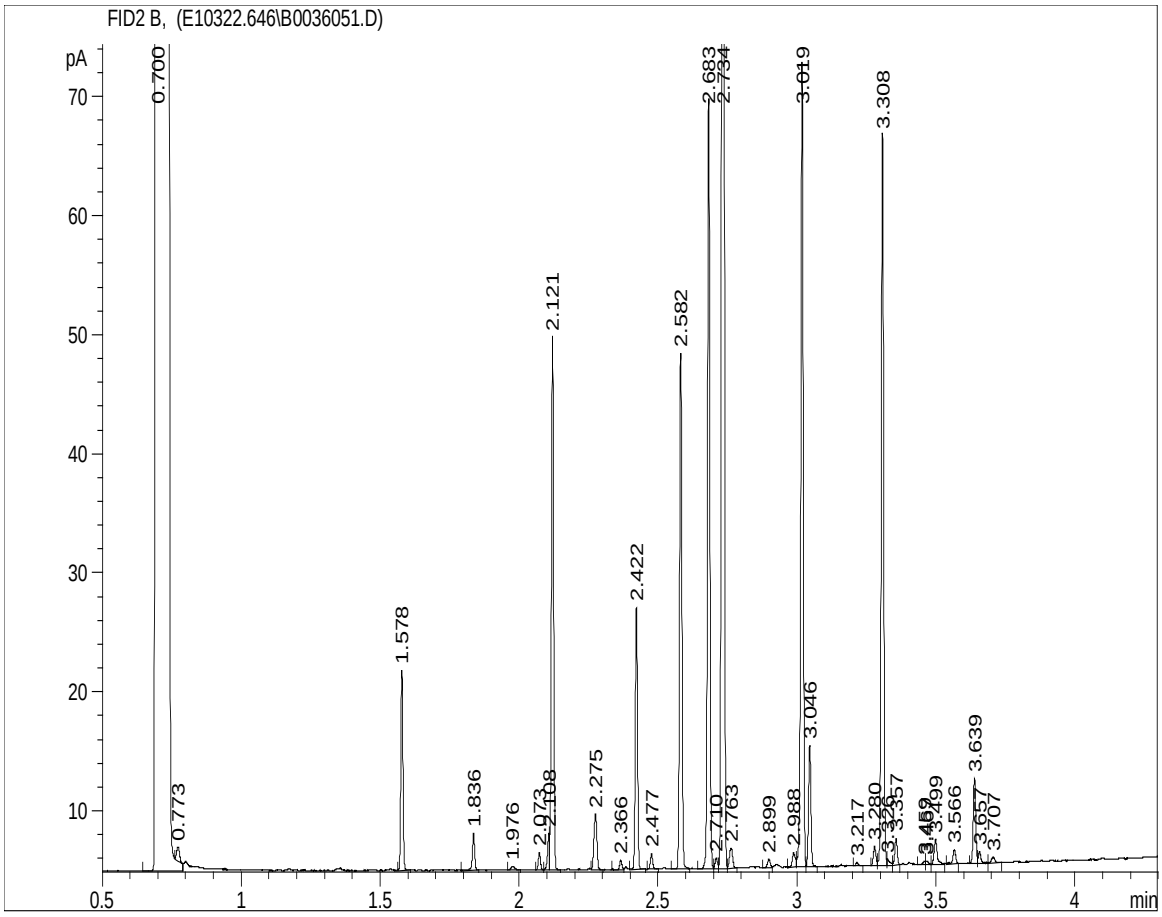

Appendix B: (Continued)

Microbial ID, Inc.
Volume: DATA File: E103226.46A Samp Ctr: 5 ID Number: 6052
Type: Samp Bottle: 72 Method: RCLIN6
Created: 3/22/2010 4:06:23 PM Created By: sstrauss (Sue Strauss)
Sample ID: C-USF10-03 (02-Oleic-Direct DL

RT	Respons	Ar/H	RFact	ECL	Peak Name	Perce	Comment1	Comment2
0.7415	1.123E+	0.02	----	6.6887	SOLVENT PEAK	----	< min rt	
1.6673	15276	0.01	1.069	12.001	12:0	3.53	ECL deviates 0.001	Reference 0.013
1.9354	2399	0.01	1.032	13.000	13:0	0.53	ECL deviates 0.000	Reference 0.012
2.0777	448	0.01	1.016	13.483	12:0 3OH	0.10	ECL deviates 0.000	
2.1680	362	0.00	----	13.789		----		
2.1802	630	0.00	----	13.831		----		
2.2290	39485	0.01	1.001	13.996	14:0	8.53	ECL deviates -0.004	Reference 0.008
2.3884	5210	0.01	----	14.511	unknown	----	ECL deviates -0.005	
2.4820	364	0.00	0.978	14.813	15:1 w8c	0.08	ECL deviates 0.000	
2.5394	17261	0.00	----	14.998	15:0	----	ECL deviates -0.001	
2.5951	1097	0.00	----	15.173		----		
2.7040	39696	0.00	0.962	15.514	Sum In Feature	8.25	ECL deviates 0.000	14:0 3OH/16:1
2.7934	6772	0.00	0.955	15.795	16:1 w9c	1.40	ECL deviates -0.005	
2.8062	34168	0.00	0.955	15.835	Sum In Feature	7.05	ECL deviates -0.005	16:1 w7c/16:1
2.8347	399	0.01	0.953	15.924	16:1 w5c	0.08	ECL deviates -0.003	
2.8586	165258	0.00	0.951	15.999	16:0	33.96	ECL deviates 0.000	Reference 0.009
2.8883	1192	0.01	----	16.093		----		
2.9563	1102	0.01	----	16.306		----		
3.0279	854	0.01	0.941	16.531	15:0 3OH	0.17	ECL deviates -0.002	
3.1189	835	0.01	0.936	16.817	17:1 w8c	0.17	ECL deviates 0.002	
3.1503	36377	0.01	0.934	16.916	17:0 cyclo	7.34	ECL deviates 0.001	
3.1773	7301	0.00	0.932	17.001	17:0	1.47	ECL deviates 0.001	Reference 0.007
3.4285	90120	0.01	0.919	17.797	18:1 w9c	17.90	ECL deviates 0.003	
3.4447	31781	0.00	0.919	17.848	Sum In Feature	6.31	ECL deviates 0.001	18:1 w7c
3.4938	1425	0.01	0.916	18.004	18:0	0.28	ECL deviates 0.004	Reference 0.007
3.6391	1518	0.01	----	18.475		----		
3.7086	718	0.01	----	18.701		----		
3.7718	8920	0.01	0.904	18.906	Sum In Feature	1.74	ECL deviates 0.019	19:0 cyclo
3.7804	5168	0.00	0.904	18.934	19:0 cyclo w8c	1.01	ECL deviates 0.002	
3.7996	519	0.00	0.903	18.996	19:0	0.10	ECL deviates -0.003	Reference -0.005
----	39696	---	----	----	Summed	8.25	12:0 aldehyde ?	unknown
----	-----	---	----	----		----	16:1 iso I/14:0 3OH	14:0 3OH/16:1
----	34168	---	----	----	Summed	7.05	16:1 w7c/16:1 w6c	16:1 w6c/16:1
----	8920	---	----	----	Summed	1.74	19:1w7c/19:1 w6c	19:1
----	-----	---	----	----		----	19:0 cyclo	
----	31781	---	----	----	Summed	6.31	18:1 w7c	18:1 w6c

ECL Deviation: 0.005 Reference ECL Shift: 0.009 Number Reference Peaks: 7
Total Response: 494184 Total Named: 487566
Percent Named: 98.66% Total Amount: 462899

Appendix B: (Continued)

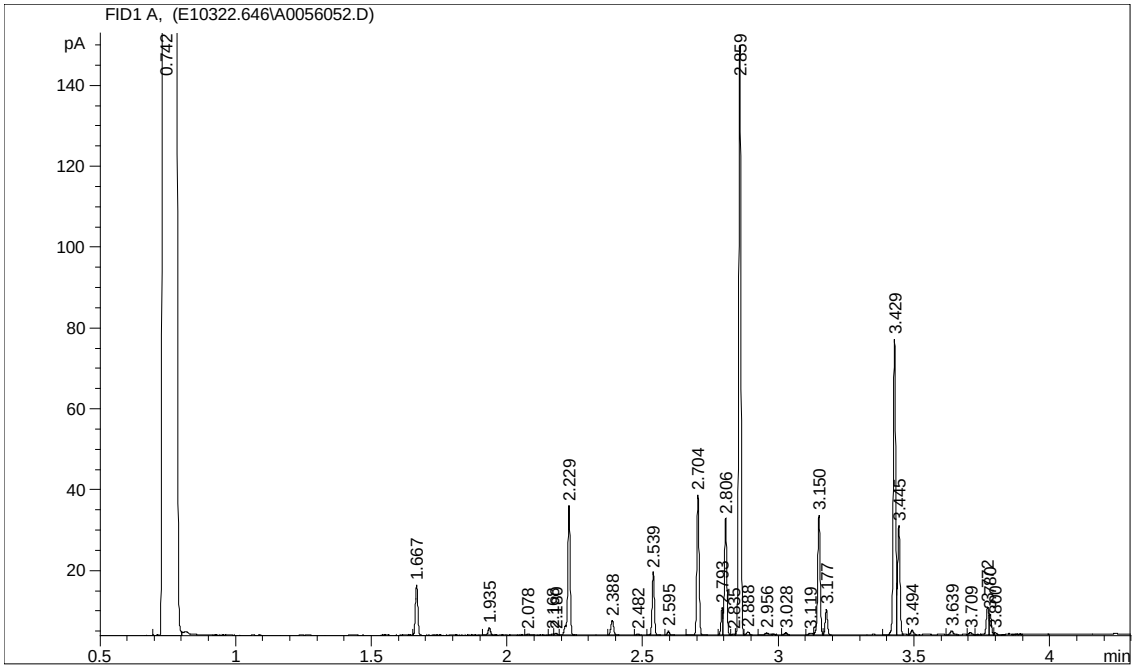

Appendix B: (Continued)

Microbial ID, Inc.
Volume: DATA File: E103226.46B Samp Ctr: 4 ID Number: 6053
Type: Samp Bottle: 73 Method: RCLIN6
Created: 3/22/2010 4:06:23 PM Created By: sstrauss (Sue Strauss)
Sample ID: C-USF10-03 (03-Palmitoleic-Direct DL

RT	Respons	Ar/H	RFact	ECL	Peak Name	Percen	Comment1	Comment2
0.6998	1.163E+	0.01	----	6.6888	SOLVENT PEAK	----	< min rt	
0.7730	2173	0.01	----	7.2011		----	< min rt	
1.5381	657	0.00	----	11.820	unknown 11.825	----	ECL deviates -0.004	
1.5786	17130	0.00	1.070	12.001	12:0	3.60	ECL deviates 0.001	Reference
1.8369	2366	0.00	1.028	13.000	13:0	0.48	ECL deviates 0.000	Reference
1.9758	536	0.01	1.011	13.487	12:0 3OH	0.11	ECL deviates 0.005	
2.0733	2490	0.00	----	13.829		----		
2.1077	2552	0.00	----	13.950	unknown 13.951	----	ECL deviates -0.001	
2.1209	36016	0.00	0.995	13.996	14:0	7.04	ECL deviates -0.003	Reference
2.2760	6150	0.01	----	14.510	unknown 14.502	----	ECL deviates -0.005	
2.3672	331	0.00	0.972	14.813	15:1 w8c	0.06	ECL deviates -0.001	
2.4225	18266	0.00	----	14.996	15:0	----	ECL deviates -0.003	
2.4772	1317	0.00	----	15.172		----		
2.5820	45545	0.00	0.955	15.510	Sum In Feature 2	8.55	ECL deviates -0.005	14:0 3OH/16:1
2.6828	94182	0.00	0.948	15.834	Sum In Feature 3	17.56	ECL deviates -0.006	16:1 w7c/16:1
2.7105	575	0.00	0.946	15.923	16:1 w5c	0.11	ECL deviates -0.004	
2.7342	198761	0.00	0.945	16.000	16:0	36.93	ECL deviates 0.000	Reference
2.7628	2821	0.01	----	16.091		----		
2.8992	876	0.01	0.935	16.528	15:0 3OH	0.16	ECL deviates -0.004	
2.9256	668	0.01	----	16.613		----		
2.9959	1450	0.01	0.930	16.838	17:1 w7c	0.27	ECL deviates 0.003	
3.0187	75624	0.00	0.928	16.912	17:0 cyclo	13.80	ECL deviates -0.003	
3.0462	10821	0.00	0.927	17.000	17:0	1.97	ECL deviates 0.000	Reference
3.2797	2126	0.01	0.916	17.754	Sum In Feature 5	0.38	ECL deviates -0.002	18:2
3.3080	43366	0.00	0.914	17.845	Sum In Feature 8	7.80	ECL deviates -0.002	18:1 w7c
3.3570	2020	0.01	0.912	18.004	18:0	0.36	ECL deviates 0.004	Reference
3.4659	360	0.00	----	18.364		----		
3.4986	3375	0.01	----	18.472		----		
3.5667	1727	0.01	----	18.697		----		
3.6390	3304	0.01	0.901	18.935	19:0 cyclo w8c	0.59	ECL deviates 0.004	
3.6574	1300	0.01	0.900	18.996	19:0	0.23	ECL deviates -0.003	Reference -
3.7065	958	0.01	----	19.162		----		
----	45545	---	----	----	Summed Feature	8.55	12:0 aldehyde ?	unknown
----	-----	---	----	----		----	16:1 iso I/14:0 3OH	14:0 3OH/16:1
----	94182	---	----	----	Summed Feature	17.56	16:1 w7c/16:1 w6c	16:1 w6c/16:1
----	2126	---	----	----	Summed Feature	0.38	18:0 ante/18:2	18:2
----	43366	---	----	----	Summed Feature	7.80	18:1 w7c	18:1 w6c

ECL Deviation: 0.003 Reference ECL Shift: 0.005 Number Reference Peaks: 7
Total Response: 550047 Total Named: 536329
Percent Named: 97.51% Total Amount: 508649

Appendix B: (Continued)

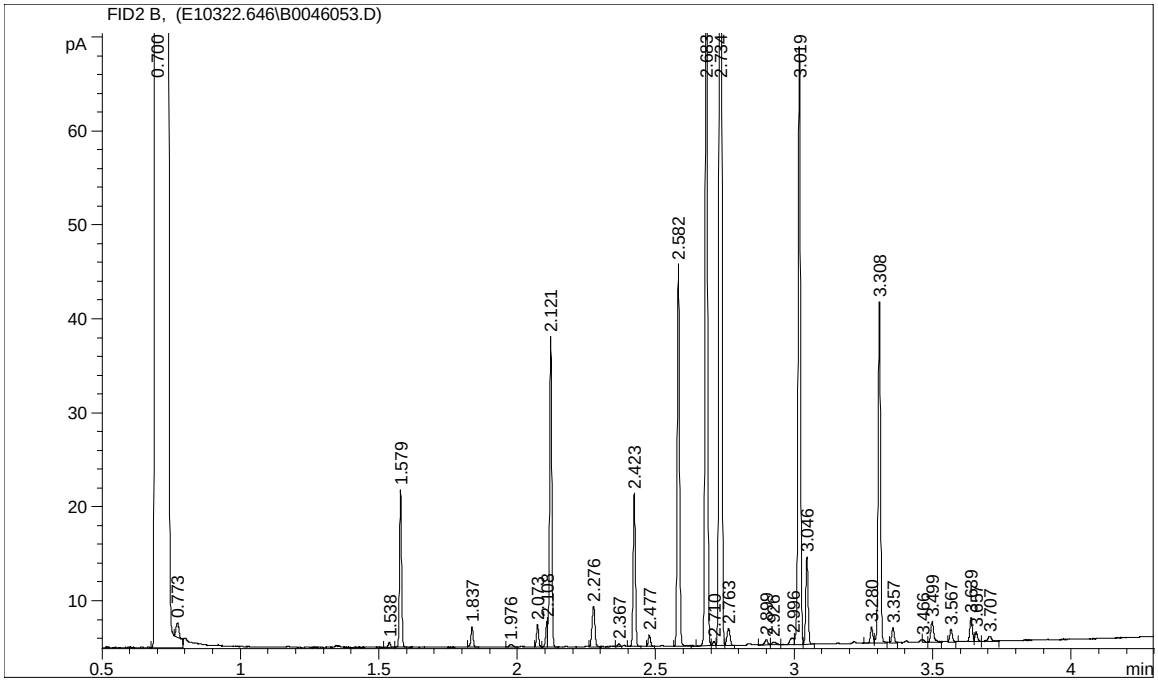

Appendix B: (Continued)

Microbial ID, Inc.
Volume: DATA File: E103226.46A Samp Ctr: 6 ID Number: 6054
Type: Samp Bottle: 74 Method: RCLIN6
Created: 3/22/2010 4:15:23 PM Created By: sstrauss (Sue Strauss)
Sample ID: C-USF10-03 (04-Linolenic-Direct DL

RT	Respons	Ar/H	RFact	ECL	Peak Name	Perce	Comment1	Comment2
0.7323	167022	0.00	----	6.6278		----	< min rt	
0.7411	1.13E+9	0.01	----	6.6861	SOLVENT PEAK	----	< min rt	
1.6677	13210	0.01	1.069	12.001	12:0	2.99	ECL deviates 0.002	Reference 0.014
1.9357	2489	0.00	1.032	12.999	13:0	0.54	ECL deviates 0.000	Reference 0.013
2.0783	486	0.01	1.016	13.484	12:0 3OH	0.10	ECL deviates 0.001	
2.1807	1205	0.00	----	13.831		----		
2.2158	2077	0.00	----	13.950	unknown 13.951	----	ECL deviates -0.001	
2.2294	37707	0.00	1.001	13.996	14:0	7.98	ECL deviates -0.004	Reference 0.010
2.3890	5513	0.01	----	14.511	unknown 14.502	----	ECL deviates -0.004	
2.4828	653	0.00	0.978	14.814	15:1 w8c	0.14	ECL deviates 0.001	
2.5401	18075	0.00	----	14.999	15:0	----	ECL deviates 0.000	
2.5956	1118	0.00	----	15.173		----		
2.7046	37923	0.00	0.962	15.515	Sum In Feature 2	7.72	ECL deviates 0.000	14:0 3OH/16:1 iso
2.8069	54115	0.00	0.955	15.836	Sum In Feature 3	10.93	ECL deviates -0.004	16:1 w7c/16:1
2.8351	774	0.01	0.953	15.924	16:1 w5c	0.16	ECL deviates -0.004	
2.8590	169755	0.00	0.951	15.999	16:0	34.18	ECL deviates 0.000	Reference 0.010
2.8894	2400	0.01	----	16.095		----		
2.9600	1236	0.02	----	16.316		----		
3.0280	826	0.01	0.941	16.530	15:0 3OH	0.16	ECL deviates -0.003	
3.1196	1549	0.01	0.936	16.817	17:1 w8c	0.31	ECL deviates 0.003	
3.1506	60288	0.01	0.934	16.915	17:0 cyclo	11.92	ECL deviates 0.000	
3.1783	8822	0.00	0.932	17.002	17:0	1.74	ECL deviates 0.002	Reference 0.011
3.4169	8936	0.00	0.920	17.758	Sum In Feature 5	1.74	ECL deviates 0.002	18:2 w6,9c/18:0
3.4296	8316	0.00	0.919	17.798	18:1 w9c	1.62	ECL deviates 0.004	
3.4447	77610	0.01	0.919	17.846	Sum In Feature 8	15.09	ECL deviates -0.001	18:1 w7c
3.4644	669	0.01	0.918	17.908	Sum In Feature 8	0.13	ECL deviates 0.007	18:1 w6c
3.4941	4036	0.01	0.916	18.003	18:0	0.78	ECL deviates 0.003	Reference 0.008
3.5508	733	0.01	0.914	18.187	17:0 iso 3OH	0.14	ECL deviates -0.006	
3.5703	1892	0.01	----	18.250		----		
3.6080	1071	0.01	----	18.372		----		
3.6395	3246	0.01	----	18.474		----		
3.7091	1682	0.01	----	18.700		----		
3.7823	7355	0.01	0.904	18.938	19:0 cyclo w8c	1.41	ECL deviates 0.006	
3.8005	1157	0.01	0.903	18.997	19:0	0.22	ECL deviates -0.003	Reference -0.002
3.8495	1008	0.01	----	19.159		----		
----	37923	---	----	----	Summed Feature	7.72	12:0 aldehyde ?	unknown 10.9525
----	-----	---	----	----		----	16:1 iso I/14:0 3OH	14:0 3OH/16:1 iso
----	54115	---	----	----	Summed Feature	10.93	16:1 w7c/16:1 w6c	16:1 w6c/16:1
----	8936	---	----	----	Summed Feature	1.74	18:0 ante/18:2	18:2 w6,9c/18:0
----	78278	---	----	----	Summed Feature	15.22	18:1 w7c	18:1 w6c

ECL Deviation: 0.003 Reference ECL Shift: 0.010 Number Reference Peaks: 7
Total Response: 512267 Total Named: 497409
Percent Named: 97.10% Total Amount: 472484

ABOUT THE AUTHOR

Omatoyo Kofi Dalrymple attended the Stewartville Primary School and then went on to high school education at St. Stanislaus College from 1991-1996. He began studies at the University of Guyana in Civil Engineering the same year he graduated high school, and completed an engineering degree with distinction in 2001. In 2002, he was awarded a CIDA scholarship to read for an MSc in Natural Resources Management with a specialization in Climate Change at the University of the West Indies, Cave Hill, Barbados. He then lived and worked in Barbados for a short while. Kofi moved to Tampa, Florida in 2005 to pursue a Doctorate in Civil & Environmental Engineering at the University of South Florida. He is very interested in forming alliances to work in areas of physical planning and infrastructural development, environment and natural resources management, water and sanitation, and youth development in the Caribbean.